Electronic Supplementary Information for:

Thermodynamic and Kinetic Studies of H_2 and N_2 Binding to Bimetallic Nickel-Group 13 Complexes and Neutron Structure of a Ni(η^2-H_2) Adduct

Ryan C. Cammarota[†‡], Jing Xie[†€β‡], Samantha A. Burgess[ƻ], Matthew V. Vollmer[†], Konstantinos D. Vogiatzis[†€£], Jingyun Ye[†€], John C. Linehan[ƻ], Aaron M. Appel[ƻ], Christina Hoffman[Ψ], Xiao-Ping Wang[Ψ], Victor G. Young, Jr.[†], Connie C. Lu*[†]

[†]Department of Chemistry and [€]Supercomputing Institute, and Chemical Theory Center, University of Minnesota-Twin Cities, 207 Pleasant Street SE, Minneapolis, Minnesota 55455, United States.

[ƻ]Catalysis Science Group, Pacific Northwest National Laboratory, P.O. Box 999, MS K2-57, Richland, Washington 99352, United States

[Ψ]Neutron Scattering Division, Oak Ridge National Laboratory, Oak Ridge, Tennessee 37831, United States

[β]Key Laboratory of Cluster Science of Ministry of Education, School of Chemistry and Chemical Engineering, Beijing Institute of Technology, Beijing 100081, China

[£]Department of Chemistry, University of Tennessee, Knoxville, Tennessee 37996, United States

[‡]These authors contributed equally.

*Corresponding author: C.C.L. (e-mail: clu@umn.edu)

SI Table of Contents

I. Data Analysis Methods

A. Determination of Thermodynamic Parameters for H_2 and N_2 Binding to NiML Complexes using VT ^{31}P NMR Spectroscopy

Fast Chemical Exchange Equilibria: Equilibrium Constant (K) Measurements

The binding equilibria of H_2 to NiML (M=Al, Ga, In; **1**−**3**), as well as that of N_2 to NiInL (**3**), were observed to be undergoing fast chemical exchange relative to the ^{31}P NMR timescale (161.9 or 202.4 MHz). These binding equilibria display a single ^{31}P NMR resonance across a wide T range, where the observed chemical shift is the population-weighted average of the chemical shifts of the two rapidly exchanging species, (L')NiML and NiML (where L' is H_2 or N_2). If the chemical shifts of (L')NiML and NiML are known, then the position of the observed chemical shift of the system at equilibrium can be used to determine the concentration ratio of (L')NiML and NiML (equation S1).[1,2]

$$\frac{[(\mathrm{L'})\mathrm{NiML}]}{[\mathrm{NiML}]} = \frac{\delta_{obs} - \delta_{\mathrm{NiML}}}{\delta_{(\mathrm{L'})\mathrm{NiML}} - \delta_{obs}} \qquad \text{(S1)}$$

In equation S1, δ_{obs} is the observed ^{31}P NMR chemical shift at equilibrium for each T, δ_{NiML} is the high T convergence of ^{31}P δ of NiML under Ar (at T ~ 373 K in toluene), and $\delta_{(L')NiML}$ is the low T convergence of ^{31}P δ of (L')NiML under high pressures of L' gas (at T ~ 193 K). After evaluating the concentration ratio of (L')NiML and NiML at each T using equation S1, the binding equilibria constants, K_{H_2} or K_{N_2}, could then be calculated using the known pressure of L' gas ($P_{\mathrm{L'}}$; equation S2), or alternatively using the dissolved gas concentration ([L']), which was based on empirically-determined gas solubility in toluene.[3-7]

$$K_{\mathrm{L'}} = \frac{[(\mathrm{L'})\mathrm{NiML}]}{[\mathrm{NiML}] \cdot P_{\mathrm{L'}}} = \frac{\delta_{obs} - \delta_{\mathrm{NiML}}}{\delta_{(\mathrm{L'})\mathrm{NiML}} - \delta_{obs}} \times \frac{1}{P_{\mathrm{L'}}} \qquad \text{(S2)}$$

Fast Chemical Exchange Equilibria: Determination of ΔH°, ΔS°, and ΔG° Binding Parameters

Two complementary methods of extracting thermodynamic binding parameters were utilized: (a) non-linear fitting of a sigmoidal ^{31}P δ vs. T plot; and (b) van't Hoff plot linear regression analysis.

(a) Fitting of Sigmoidal ^{31}P δ vs. T plot. Combining equations S2 and S5 (derived from rearranging equations S3 and S4), equation S6 is obtained upon solving for the observed ^{31}P NMR chemical shift, δ_{obs}.

$$\Delta G^\circ = -\mathrm{RT}\cdot\ln(K_{\mathrm{L'}}) \qquad \text{(S3)}$$

$$\Delta G^\circ = \Delta H^\circ - (\mathrm{T}\cdot\Delta S^\circ) \qquad \text{(S4)}$$

$$K_{\mathrm{L'}} = \mathrm{e}^{\frac{-\Delta H^\circ}{\mathrm{RT}} + \frac{\Delta S^\circ}{\mathrm{R}}} \qquad \text{(S5)}$$

$$\delta_{obs} = \frac{\left\{\left[\left(\mathrm{e}^{\frac{-\Delta H^\circ}{\mathrm{RT}} + \frac{\Delta S^\circ}{\mathrm{R}}}\right) \cdot P_{\mathrm{L'}} \cdot \left(\delta_{(L')NiML}\right)\right] + \delta_{NiML}\right\}}{\left\{\left[\left(\mathrm{e}^{\frac{-\Delta H^\circ}{\mathrm{RT}} + \frac{\Delta S^\circ}{\mathrm{R}}}\right) \cdot P_{\mathrm{L'}}\right] + 1\right\}} \qquad \text{(S6)}$$

Using equation S6, ΔH°, ΔS°, and $\delta_{(L')NiML}$ were fit to the experimental data (using the SOLVER function in Microsoft Excel) such that the sum of the squared residuals was minimized between the calculated and experimental values for δ_{obs}. The thermodynamic binding parameters obtained from non-linear fitting matched within error of those obtained from van't Hoff analysis (described below) in all cases, with the van't Hoff values preferred because of the more straightforward tabulation of the uncertainty via linear regression. Δ*G*° at 298 K was calculated using equation S4 based on the tabulated Δ*H*° and Δ*S*° values.

(b) van't Hoff Analysis. A van't Hoff plot of ln($K_{L'}$) vs. 1/T was constructed and used to extract Δ*H*° and Δ*S*° for L' binding (based on manipulation of equations S3 and S4 to give equation S7). Δ*G*° at 298 K was calculated using equation S4 and the Δ*H*° and Δ*S*° values determined from the van't Hoff plot.

$$\ln(K_{L'}) = \frac{-\Delta H°}{R}\left(\frac{1}{T}\right) + \frac{\Delta S°}{R} \qquad \text{(S7)}$$

The non-linear fitting approach outlined in method "A" complements the van't Hoff analysis by providing the best-fit value for $\delta_{(L')NiML}$ that is utilized in calculating ln$K_{L'}$ at each T in the van't Hoff analysis (equation S2). It should also be noted that van't Hoff plots were found to deviate from linearity in some cases at very low T and/or low pressures of L' gas due to a breakdown in the assumption of fast chemical exchange. Thus, van't Hoff analysis was only used for data collected at temperature-pressure combinations where fast chemical exchange was ensured to be a valid assumption (please refer to section B for additional considerations regarding the validation of fast chemical exchange). Lastly, the standard deviations reported for Δ*H*° and Δ*S*° were obtained by propagating the error associated with the slope and the y-intercept, respectively, from linear regression analysis of the van't Hoff plot.

Slow Chemical Exchange Equilibria: Determination of K, ΔH°, ΔS°, and ΔG°

The binding equilibrium of N_2 to NiGaL (**2**) was observed to be undergoing slow chemical exchange at low T relative to the ^{31}P NMR timescale (161.9 MHz). Distinct ^{31}P NMR resonances were observable for (N_2)NiGaL (**2**−N_2) and NiGaL (**2**) over a range of T (193 K to 237 K), and their relative integrations were used in conjunction with the known pressures of N_2 (or alternatively the known [N_2] in toluene[3-5]) in order to calculate K_{N_2} at each T (equation S2). Thermodynamic binding parameters were subsequently extracted from the van't Hoff analysis (equation S7), with Δ*G*° at 298 K determined using equation S4. Similar evaluation of K_{N_2} based on relative peak integrations was carried out for N_2 binding to NiAlL (**1**), which also was found to exhibit slow exchange at low T (despite a high pressure of 51 atm).

Definition of Standard State for Gases: ΔG°$_{1atm}$ versus ΔG°$_{1M}$

In equations S2 and S6, $P_{L'}$ (in atm) is known based on initial pressurization of the sample, and so 1 atm is conveniently used as the standard state definition for L' gas. For (L')NiML and NiML, the standard state is defined to be 1 M at 298 K in toluene. Pressure is assumed to vary with temperature in accordance with Guy Lussac's Law for a closed system ($P_1/T_1 = P_2/T_2$). This treatment for determining $P_{L'}$ at various T was applied for both the case of VT NMR with a pressurized J. Young tube, which is unambiguously a closed system, as well as for the more ambiguous case of VT NMR with a pressurized PEEK tube in which the sample was locally heated while attached to an ISCO pump that maintains a constant pressure.[8] Please refer to Table S2 (and the accompanying discussion) to see how the assumption of the interdependence of P and T for high-pressure PEEK cells (as opposed to constant P_{H_2}) impacts the thermodynamic results for H_2 binding to **2**.

Alternatively, the standard state for L' gas can be defined as 1 M, in which case the solubility of L' gas in toluene and its dependence on T was taken to be that determined empirically in the literature (see below). Although adopting $P_{L'}$ = 1 atm as the standard state for gases is our preference (see discussion below), we have calculated both standard states to allow facile comparisons with other literature reports. For the alternative standard state definition of 1 M gas, the dissolved gas concentrations (in mol/L) of H_2 and N_2 at 1 atm pressure in toluene were determined using empirical equations S8-S9, where $\chi_{L'}$ is the gas-solute mole ratio ($\chi_{L'} = \frac{\text{mol } L' \text{ dissolved}}{\text{mol toluene + mol } L' \text{ dissolved}}$), R is the ideal gas constant (in J/mol·K), T is temperature (in K), and τ = T/100.

$$\ln(\chi_{H_2}) = -5773/RT + -47.68/R \qquad (S8)$$

$$\chi_{N_2} = \exp[(-6.27576) - (3.71675/\tau)] \qquad (S9)$$

For equation S8, empirical constants of 5773 J/mol and −47.68 J/(mol·K) were previously reported based on solubility measurements for 1 atm H_2 in toluene over the range of T = 298 to 373 K.[6] For equation S9, empirical constants were experimentally determined for 1 atm N_2 in toluene over the range of T = 283 to 313 K.[3-5] Another recent set of data collected at 303 K and 363 K is in accord with the empirical solubility relationship for N_2 utilized in this work.[7]

For **1-3**, converting the binding free energy values ($\Delta G°$) in toluene from a standard state of 1 atm gas pressure (denoted by $\Delta G°_{1atm}$) to that of 1 M gas concentration (denoted by $\Delta G°_{1M}$) results in $\Delta G°_{1M}$ being more favorable than $\Delta G°_{1atm}$ by ~3.5 kcal/mol for H_2 binding and ~3.1 kcal/mol for N_2 binding (assuming no change in solution volume). Hence, we can compare either $\Delta G°_{1atm}$ or $\Delta G°_{1M}$ values for H_2 and N_2 binding to **1-3** with literature values, which are typically reported for one of these two standard states. Tables S6-S9 show the H_2 and N_2 binding parameters for complexes **1-3** compared with those determined for other transition metal complexes in the literature.

To crudely compare *all* literature complexes, we converted the reported $\Delta G°$ values for a given standard state to the other standard state by applying the conversion factors derived from our results for **1-3**, with estimated binding parameters obtained via such manipulations clearly denoted by footnotes in Tables S6-S9. This is a rough approximation because our experimental conditions are not identical to conditions used for previous binding studies, and the conversion between 1 M and 1 atm standard states will vary slightly in different solvents. Hence, $\Delta G°$ values for literature complexes reported with respect to different standard states cannot be compared rigorously, and caution should be exercised when attempting to compare binding parameters for two literature complexes with differing standard state definitions.

Defining the standard state as 1 atm gas pressure is sensible because:

- The gas pressure is known precisely at all T based on the initial pressurization at 298 K and Guy Lussac's Law ($P_1/T_1 = P_2/T_2$). On the contrary, determining H_2 and N_2 concentrations at all T requires knowing the precise solution volume and the T dependence of the gas solubility in a specific solvent (both of which are subject to error). Furthermore, empirically-determined gas solubility relationships are based on data collected over specific T ranges (*vide supra*). The thermodynamic binding data sets in this work, as well as those in a related study which also utilizes empirical gas solubility data,[9] often include data collected at T that lie outside the ranges for which the solubility data was collected, and so extrapolation of the empirical solubility relationships may not be explicitly valid.
- A standard state of 1 atm for gases is more realistic and closer to actual experimental conditions than [gas] = 1 M. For example, at 1 atm in toluene at 298 K, $[H_2] \approx 0.003$ M and $[N_2] \approx 0.005$ M, which is far lower than 1 M.[5,10] Thus, one consequence of defining the standard state to be [gas] = 1 M is that $\Delta G°_{1M}$ will invariably be negative, as even very weak binding equilibria will be favorable under the extreme conditions of 1 M dissolved gas concentration. For example, $\Delta G°_{1M}$ for H_2 binding to NiAlL (**1**) is −1.9(2) kcal/mol, even though the equilibrium lies heavily towards NiAlL (**1**) under the experimental conditions (1 atm H_2, 298 K, toluene) and only ~7% of (η^2-H_2)NiAlL (**1**−H_2) is present at equilibrium. Therefore, we feel that defining the standard state to be 1 atm H_2 gas pressure, which gives $\Delta G°_{1atm}$ = +1.6(2) kcal/mol, better conveys the favorability for this (and related) binding equilibria because it describes the typical experimental conditions much more closely.

B. Case Study of H_2 Binding to Complex 2: Examining the Impact of Exchange Rates and Other Factors on the Reliability of Thermodynamic Binding Parameters

The binding of H_2 to **2** was studied in the most depth, with VT ^{31}P NMR studies performed under various H_2 pressures (0.1, 1.0, 6.8, 13.6, and 34 atm) and a wide T range (193 to 368 K). As such, the determination of the thermodynamic binding parameters for H_2 binding to **2** are presented in detail to illustrate the importance of gas pressure, exchange rates, and temperature (T) on the reliability of the obtained thermodynamic values.

Gas Pressure

Varying the H_2 pressure (0.1, 1.0, 6.8, 13, and 34 atm) resulted in significant changes in the ^{31}P VT NMR profile, as well as in the rate of chemical exchange between **2** and **2**−H_2. The reported thermodynamic parameters for H_2 binding to **2** (Table 2) were based on van't Hoff analyses of data sets collected under 6.8 and 13.6 atm H_2 (reported as an average). These two data sets were selected for analysis because they exhibit fast-exchange kinetics (for T > 240 K) and permit sampling of a large portion of the equilibrium by varying T, as reflected by the significant variation of the observed ^{31}P NMR peak position with T (see Figures 2 and S15; ^{31}P δ = 56.9 to 42.7 at 6.8 atm, and 56.9 to 47 ppm at 13.6 atm). On the other hand, increasing H_2 pressure to 34 atm resulted in the presence of a large percentage of **2**−H_2 at equilibrium across all T, such that the ^{31}P δ changed more narrowly (^{31}P δ = 56.9 to 50.4 ppm; Figure S15). More precise thermodynamic binding parameters can be obtained for data collected at 6.8 atm and 13.6 atm H_2 than for that measured at 34 atm, as the former contain fewer data points where ^{31}P δ_{obs} is close to the $\delta_{(H_2)NiML}$ convergence endpoint, which is, itself, subject to error (fit based on ^{31}P δ vs. T plot, as previously described). For these reasons, data collected at 34 atm H_2 was not included in van't Hoff analyses; however, this high-pressure data was important for determining ^{31}P δ of **2**−H_2 based on convergence behavior at high $P_{\mathrm{H_2}}$ and low T. Data collected under 1 atm H_2 was also eschewed from van't Hoff analysis despite exhibiting the largest ^{31}P δ variation with T (^{31}P δ = 56.9 to 38 ppm; Figure 2b), as chemical exchange kinetics do not adhere to the fast exchange requirement at T < 300 K (see Figures S2-S3 and the accompanying exchange rate discussion in the next section for additional details).

Exchange Rate

A critical assumption for extracting thermodynamic parameters based on a population-weighted average chemical shift is that chemical exchange between the two species in question is truly fast relative to the NMR timescale. Rigorously fast chemical exchange occurs when $\mathrm{rate_{ex}} >> (\delta_A - \delta_B)$, where $\mathrm{rate_{ex}}$ is the exchange rate, and δ_X are the chemical shifts (in Hz) of the exchanging species (Equation S10).[1,11,12]

$$\mathrm{rate_{ex}}/(\delta_A - \delta_B) > 10 \qquad \text{(S10)}$$

If the inequality in equation S10 holds true, then the fast-exchange assumption is valid and $K_{\mathrm{H_2}}$ can be accurately determined from the observed chemical shift (δ_{obs}). Chemical exchange can also be qualitatively assessed based on the line widths of the observed ^{31}P peak. In the fast-exchange limit, the observed ^{31}P resonance will shift between δ_A and δ_B as T (and/or $P_{\mathrm{H_2}}$ in this case) is varied, but the peak should not broaden significantly. In contrast, the fast-intermediate and intermediate exchange regimes, where $\mathrm{rate_{ex}}$ is between 1 and 10 times the peak separation ($\delta_A - \delta_B$), are characterized by significant peak broadening as the observed resonance shifts between δ_A and δ_B.[1] In the fast-intermediate and intermediate exchange regimes, complex non-Lorentzian lineshapes and exchange broadening result in ^{31}P δ_{obs} no longer representing the population-weighted average of δ_A and δ_B for the exchanging species.[2,13] Thus, if chemical exchange is not rigorously fast, and instead is fast-intermediate, then thermodynamic parameters extracted from observed chemical shifts will be prone to error and will be unreliable.[2] Additionally, substantial peak broadening in fast-intermediate and intermediate exchange regimes also results in greater error in measuring δ_{obs}, and hence introduces further error into thermodynamic parameter determination.

It is not trivial to differentiate borderline cases of fast chemical exchange and fast-intermediate (ie. how much broadening concurrent with peak shifting is problematic?). In practice, borderline cases typically are assumed to be fast exchange to easily facilitate analysis, with little confirmation that this is indeed the correct assumption.[2] In order to ensure that the VT ^{31}P NMR spectroscopy studies reported in this work gave valid and reliable thermodynamic results, we excluded data sets where significant peak broadening was observed concurrent with peak shifting, as illustrated by the 1 atm data set in Figure S1 (right).

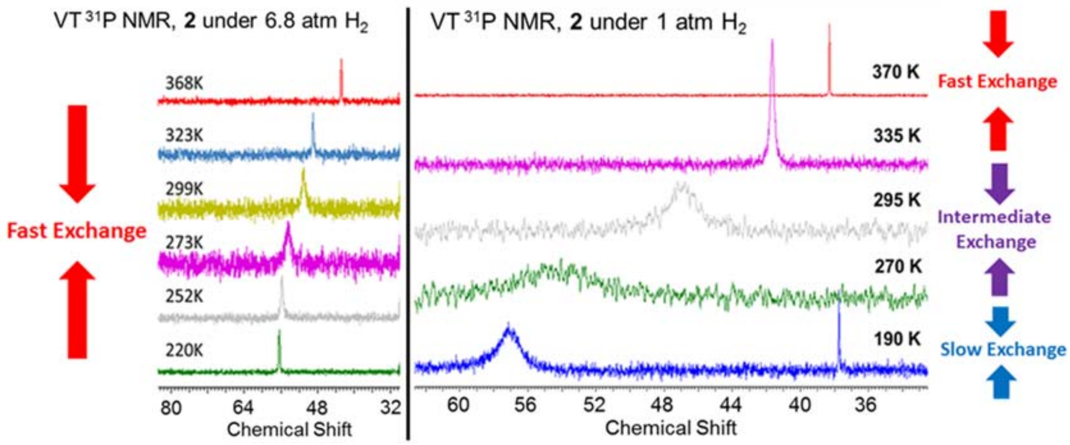

Figure S1. Stacked VT ^{31}P NMR spectra for **2** under 6.8 atm (left) and 1.0 atm H_2 (right).

Under 1 atm H_2, interconversion between **2** and **2**−H_2 is fast relative to the ^{31}P NMR timescale (161.9 MHz) at high T, but transitions to intermediate and slow exchange regimes as T is decreased (Figure S1, right). At a higher H_2 pressure of 6.8 atm, the broadening of the observed peak is minimal (Figure S1, left). Figure S15 shows a similar comparison for higher H_2 pressures, 13.6 and 34 atm, which also show relatively sharp ^{31}P peaks at all T. The lack of peak broadening at higher H_2 pressures qualitatively suggested faster chemical exchange, which makes intuitive sense because higher H_2 pressures result in greater dissolved H_2 concentrations and increased rates of H_2 binding to NiML complexes. This trend of increased chemical exchange rates at higher gas pressures was quantified explicitly for H_2 binding to **2** (see Figures S45-S46). Thus, to ensure rigorously fast exchange rates and reliable determination of binding parameters, the binding equilibria in this work were studied under elevated gas pressures (6.8 and 13.6 atm for H_2 binding to **2**; 34 and 51 atm, respectively, for H_2 and N_2 binding to **1**). One exception is the case of H_2 binding to **3**, where H_2 binding is so favorable that sub-ambient pressures (0.1 atm) are needed to establish a measurable equilibrium between **3** and **3**−H_2. This special case was discussed in the main text, and the resulting binding parameter estimates were supported by additional experiments (Figures S24-S26).

In addition to using elevated gas pressures where possible and visually inspecting the broadness of the ^{31}P NMR resonances, two different quantitative approaches were carried out to validate the assumption of rigorously fast chemical exchange. The first of these approaches involved extracting rate$_{ex}$ values via ^{31}P NMR lineshape simulations at various T (at 1 atm H_2; see methods section C for details).[11,13-16] With the known dependence of rate$_{ex}$ on T in hand, along with the peak separation ($\delta_A - \delta_B$), we were able to evaluate the conditions (T and P_{H_2}) for which equation S10 is true. Table S1 shows the results of this analysis for H_2 binding to complexes **1**−**3** under 1 atm H_2, where the minimum T required for fast chemical exchange was determined based on measured rate$_{ex}$ at various T.

Table S1. Comparison of ^{31}P δ_{NiML}, $\delta_{(H_2)NiML}$, and peak separation ($\delta_{NiML} - \delta_{(H_2)NiML}$) for the NiML complexes **1**−**3**, and the minimum T at 1 atm H_2 for fast interconversion of NiML and (η^2-H_2)NiML.

complex (M)	^{31}P δ (ppm)[a]		Peak Separation, Δν		Minimum T for Fast Exchange[b]	
	(η^2-H_2)NiML	NiML	161.9	202.4	161.9 MHz	202.4 MHz
1 (Al)	44.3	30.7	2200	2750	> 292	> 297
2 (Ga)	56.9	37.5	3130	3920	> 308	> 313
3 (In)	67.5	44.2	3770	4710	> 341	> 347

[a] Chemical shifts (in toluene-d_8) are the high T convergence for NiML (under 1 atm Ar) and the low T convergence for (η^2-H_2)NiML (under high H_2 pressure). [b] Minimum T is for 1 atm H_2; the minimum T required for fast exchange decreases significantly with increasing H_2 pressure (see Figures S45-S46 for exchange rate dependence on P_{H_2}).

Table S1 and Figure S1 illustrate the dramatic effect of T on the exchange rate. It is ideal to study binding equilibria over a wide T range, as this will in principle permit obtaining more data points that sample a larger portion of the equilibrium, which will in turn allow for a more reliable van't Hoff analysis from which to extract thermodynamic parameters. The tabulated data show that rigorously fast interconversion of **2** and **2**−H_2 under 1 atm H_2 only occurs when T is > ~310 K, and so data collected at T < ~310 K (at 1 atm H_2) will lead to the breakdown of the fast exchange assumption (Table S1). As the H_2 pressure is increased, the exchange rate increases for a given T and fast exchange becomes an increasingly valid assumption at lower T, which allows for more data points over a wider T range to be included in van't Hoff analysis. We note that performing NMR lineshape analyses can be quite challenging and time-intensive, and so we only performed this analysis extensively at 1 atm H_2 (see methods section C for details on NMR lineshape simulations).

The second approach for quantitative validation of fast exchange involves close examination of the van't Hoff plots (and the resulting thermodynamic values) obtained under different temperature ranges. This approach is also helpful in assessing the magnitude of potential errors in thermodynamic values associated with incorrect application of the fast exchange assumption. Ideally, if fast exchange holds true for all T included in the van't Hoff analysis, then the binding parameters extracted from the slope and y-intercept of the van't Hoff plot for any smaller T subrange should not differ significantly from those obtained from the trendline for the full T range. As an example, Figure S2 shows the van't Hoff plot for H_2 binding to **2** under 1 atm pressure subdivided into three T subranges. The linear trendline equations for each T subset illustrate the stark differences for measurements obtained across the different T regimes.

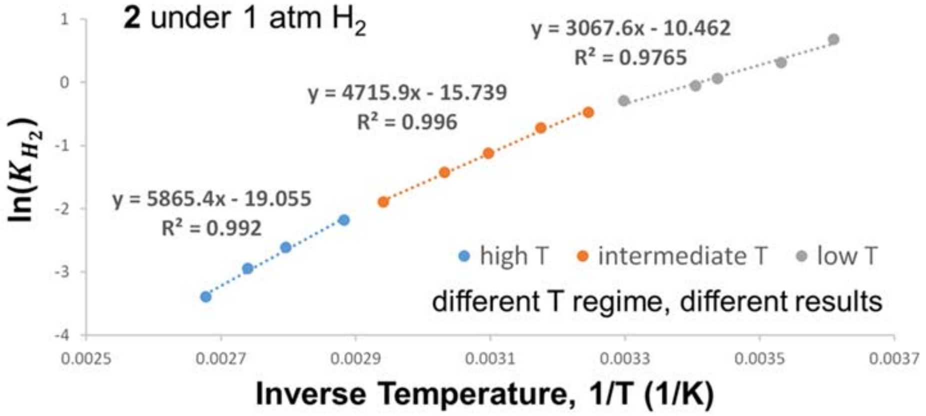

Figure S2. The van't Hoff plot for H_2 binding to **2** under 1 atm H_2 subdivided into three T regimes: "low" (277 to 303 K), "intermediate" (308 to 340 K), and "high" (346 K to 368 K).

Next, the thermodynamic parameters ($\Delta H°$, $\Delta S°$, and $\Delta G°$) were determined from the van't Hoff plots in each of the T subsets. Figure S3 shows plots of $\Delta H°$ (left) and $\Delta G°$ (right; calculated at 298 K) as a function of the T regimes. For the T axis, the average T of each T subset was used. Although it is not shown, it should be noted that the plot of $\Delta S°$ vs. T regime has a nearly identical profile to $\Delta H°$ plot. Analogously, subdividing the van't Hoff plot into 3 T regimes was also performed for the H_2 binding equilibrium with **2** under 6.8 atm H_2, and the resulting $\Delta H°$ and $\Delta G°$ (at 298 K) values as a function of T regime are also plotted in Figure S3 for comparison. Ideally, the $\Delta H°$ and $\Delta G°$ (at 298 K) values determined from van't Hoff analysis should not vary significantly based on the T regime in which data was collected. Thus, flat plots in Figure S3 are suggestive of ideal fast exchange behavior and are indicative that the thermodynamic results are the same regardless of which T subsets are considered for van't Hoff analysis (as should be the case). This seen to be essentially true for **2** under 6.8 atm H_2, and will only hold true to a greater extent for the higher pressure 13.6 atm H_2 data set, but clearly is not true for the 1 atm H_2 data set (Figure S3).

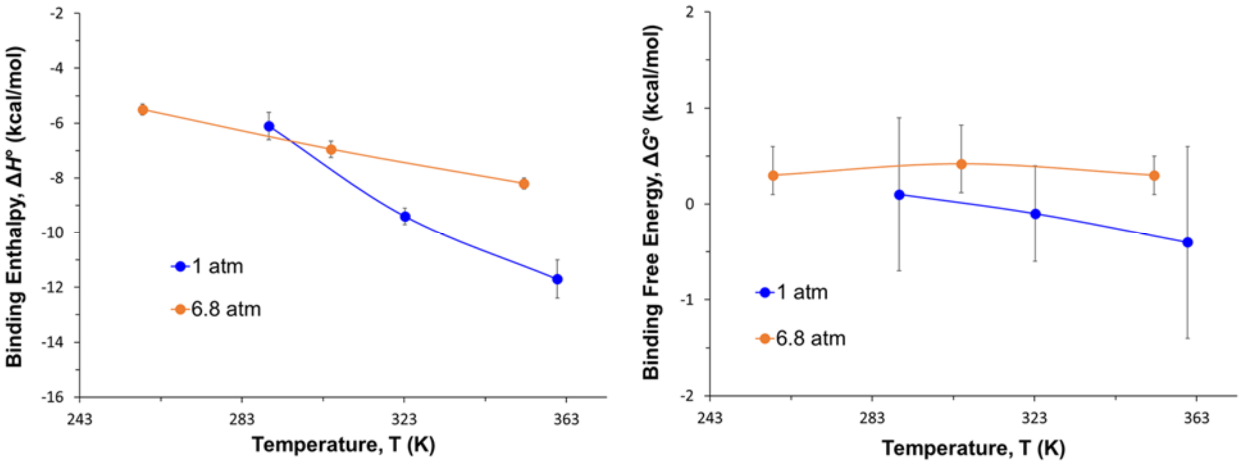

Figure S3. Plot of Δ*H*° (left) and Δ*G*° (right; calculated at 298 K based on Δ*H*° and Δ*S*°) vs. average T of data subset for H_2 binding to **2** at 1 and 6.8 atm H_2. Error bars represent the standard deviation in each value, which are larger compared to van't Hoff analysis of the full data set because there are less data points in the regression analysis for each T regime subset. At 1 atm H_2: Δ*H*° = −11.7(7), −9.4(3), and −6.1(5) kcal/mol; Δ*S*° = −38(2), −31(1), and −21(2) cal/mol·K; and Δ*G*° = −0.4(1.0), −0.1(5), and +0.1(8) kcal/mol for the high, intermediate, and low T regimes, respectively. At 6.8 atm H_2 (with two subsets): Δ*H*° = −7.7(2) and −6.4(4) kcal/mol; Δ*S*° = −27.1(5) and −24.0(1.4) cal/mol·K; and Δ*G*° = +0.4(2) and +0.5(6) kcal/mol for high (300 to 368 K) and low T (240 to 299 K) regimes, respectively.

Clearly the Δ*H*° and Δ*S*° values obtained for different T subsets at 1 atm H_2 are very different, and their significant temperature-dependence can be attributed to the breakdown of the assumption of fast exchange at 1 atm H_2 as T decreases (Figure S3). Intriguingly, despite the clear breakdown in the fast exchange assumption at 1 atm H_2, Δ*G*° values *were found to be largely invariant across the different T regime subsets*. The greater robustness of Δ*G*° has been well-documented in the literature, as the co-variance of Δ*H*° and Δ*S*° can lead to compensation effects which leave Δ*G*° unchanged.[11,17] Nevertheless, incorrect application of the fast exchange assumption for the 1 atm H_2 data set gives a Δ*G*° value for H_2 binding to **2** that deviates by ~0.5 kcal/mol from that obtained with proper considerations at higher H_2 pressures (ie. Δ*G*° = +0.6(2) kcal/mol; Table 2). Given the potential for introducing error in thermodynamic parameters,[2] we also validated the fast exchange assumption for other binding equilibria (Figures S4-S6).

Caution: The van't Hoff plot for the full dataset in Figure S2 has a reasonably high R^2 value of 0.983 over the full T range, and as such it easily could be mistaken for a linear plot suitable for extracting thermodynamic parameters. However, both qualitative and quantitative analyses clearly show the dramatic effects of T on the exchange rate and illustrate the danger of applying the assumption of fast exchange to extract thermodynamic parameters for an equilibrium without carefully considering the validity of this assumption under different T and P conditions.

PEEK Cells: Pressure Treatment

High-pressure studies at 6.8 atm and 13.6 atm H_2, from which thermodynamic parameters for H_2 binding to **2** were extracted, were carried out in PEEK cells pressurized with an ISCO syringe pump which maintains a constant P_{H_2}.[8] However, the volume of the PEEK cell in the NMR instrument over which T is varied is small relative to that of the entire high-pressure gas line, and so the local pressure and H_2 concentration in solution should still be perturbed by local variations in T similarly to the closed system case. Therefore, we believe that the best assumption is still to treat P_{H_2} as varying with T using Guy Lussac's Law, but in light of the ambiguity of this "locally heated and cooled" open system, Table S2 shows how assuming constant P_{H_2} would impact the thermodynamic results for H_2 binding to **2**.

Relatively minor differences are seen in the resulting values for Δ*H*° (−4.9 to −6.6 kcal/mol) and Δ*S*° (−18.5 to −23.8 cal/mol·K) depending on which assumptions are made regarding the dependence of $P_{\mathrm{H_2}}$ on T (Table S2). Importantly, regardless of which assumptions are made, Δ*G*° remains invariant in all cases (0.6 ± 0.2 kcal/mol). The final values reported in the main text are from the last row in Table S2, which is a combined linear regression of the van't Hoff plot that uses both the 6.8 and 13.6 atm datasets with the assumption that $P_{\mathrm{H_2}}$ varies with T in accordance with Guy Lussac's Law.

Collectively, the analyses presented in this section illustrate that Δ*G*° is a more reliable and robust value than Δ*H*° and *Δ**S*° to compare between complexes **1-3** and with the binding energetics for other complexes reported in the literature.

Table S2. Thermodynamic parameters for H_2 binding to **2** categorized by data sets (data collected under 6.8 atm or 13.6 atm H_2, or both), fitting method (van't Hoff or non-linear ^{31}P δ vs. T), and treatment of P (vary with T vs. constant).

H_2 Pressure (atm)	Fit Type	Assumption	Fit Quality	# pts	T Range (K)	ΔH° (kcal/mol)	ΔS° (cal/[mol·K])	ΔG° (kcal/mol)
6.8	van't Hoff	P α T	$R^2 = 0.992$	15	> 240 K	−6.6 (± 0.2)	−23.8 (± 0.6)	+0.5 (± 0.2)
6.8	non-linear	P α T	$Res^2/pt = 0.13$	17	200 to 370 K	−6.8	−24.5	+0.5
6.8	van't Hoff	const. P	$R^2 = 0.991$	15	> 240 K	−6.0 (± 0.2)	−21.7 (± 0.5)	+0.5 (± 0.2)
6.8	non-linear	const. P	$Res^2/pt = 0.12$	17	200 to 370 K	−6.2	−22.4	+0.5
13.6	van't Hoff	P α T	$R^2 = 0.993$	9	> 240 K	−5.5 (± 0.2)	−20.5 (± 0.6)	+0.7 (± 0.2)
13.6	non-linear	P α T	$Res^2/pt = 0.05$	12	200 to 360 K	−5.8	−21.7	+0.6
13.6	van't Hoff	const. P	$R^2 = 0.992$	9	> 240 K	−4.9 (± 0.2)	−18.5 (± 0.6)	+0.6 (± 0.2)
13.6	non-linear	const. P	$Res^2/pt = 0.05$	12	200 to 360 K	−5.2	−19.6	+0.6
6.8, 13.6 average	non-linear	P α T	–	29	200 to 370 K	−6.3	−23.1	+0.6
6.8, 13.6 average	non-linear	const. P	–	29	200 to 370 K	−5.7	−21.0	+0.6
6.8, 13.6 combined fitting	non-linear	P α T	–	29	200 to 370 K	−6.7	−24.2	+0.5
6.8, 13.6 average	van't Hoff	P α T	–	24	> 240 K	−6.0 (± 0.8)	−22 (± 2)	+0.6 (± 0.2)
6.8, 13.6 average	van't Hoff	const. P	–	24	> 240 K	−5.4 (± 0.8)	−20 (± 2)	+0.6 (± 0.2)
6.8, 13.6 combined regression	van't Hoff	P α T	–	24	> 240 K	−6.3 (± 0.2)	−23.0 (± 0.7)	+0.6 (± 0.3)

Validation of Fast Exchange Rate Assumption for other Binding Equilibria

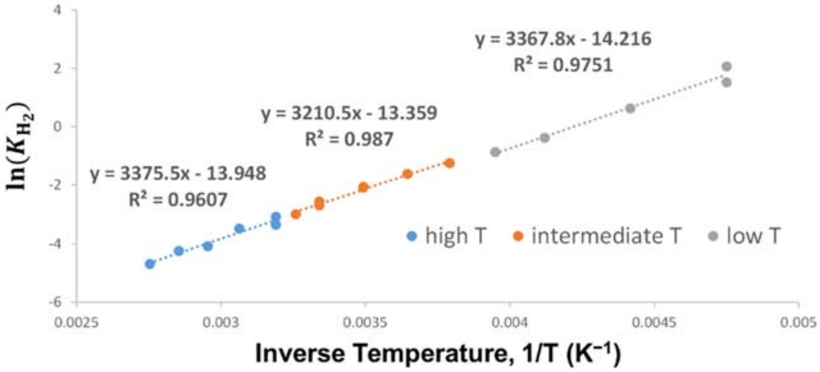

Figure S4. van't Hoff plot for H_2 binding to **1** under 34 atm H_2 subdivided into three T regimes: "low" (210 to 253 K), "intermediate" (263 to 307 K), and "high" (313 to 368 K).

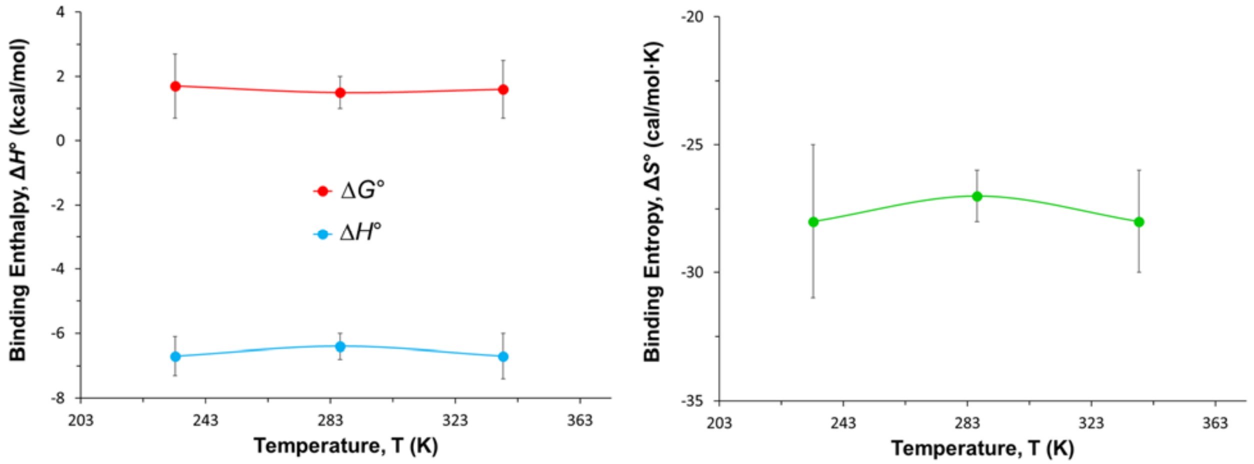

Figure S5. Plots of Δ*H*° (left) and Δ*G*° (right; at 298 K) vs. T for H_2 binding to **1** under 34 atm H_2. Error bars represent the standard deviation in each value. Essentially no T dependence was observed for all thermodynamic parameters. Δ*H*° = −6.7(7), −6.4(4), and −6.7(6) kcal/mol; Δ*S*° = −28(2), −27(1), and −28(3) cal/mol·K; Δ*G*° = +1.6(9), +1.5(5), and +1.7(1.0) kcal/mol for the high, intermediate, and low T regimes, respectively.

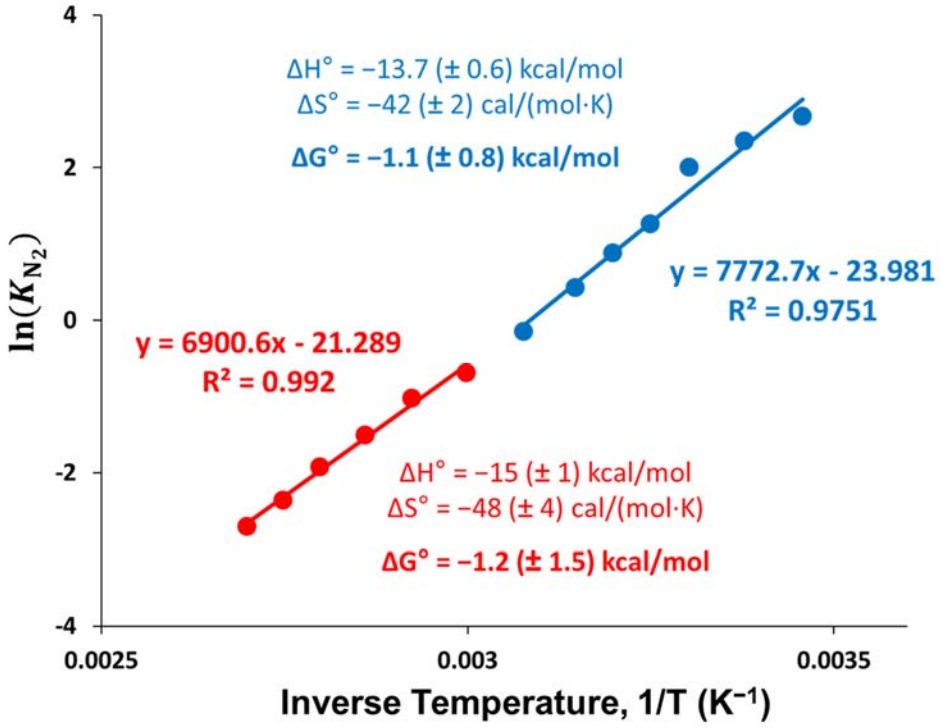

Figure S6. van't Hoff analysis for N_2 binding equilibrium with **3** under 1 atm N_2 (T = 288 to 370 K), plotted as two T subsets: high (333 to 370 K) and intermediate (289 to 325 K). Both T subsets yield identical Δ*H*°, Δ*S*°, and Δ*G*° values, within experimental error (see labels above). Low T data (< 288 K) was not considered for van't Hoff analysis based on the observation of significant peak broadening.

C. Kinetics Studies: Rates of H_2 Self-Exchange and H_2 Loss from ^{31}P NMR Lineshape Analysis

Data Analysis Procedure. The rates of self-exchange, which involves the interconversion of (η^2-H_2)NiML and NiML, were determined via a global lineshape analysis of VT ^{31}P NMR spectra collected in toluene-d_8 over a wide T range (213 to 343 K). The exchange rate (rate$_{ex}$ in s^{-1}), or the frequency of chemical exchange, was determined at each T using gNMR version 5.0 and the associated suite of programs (gCVT and gSPG) to find the best least-squares fit to the experimental spectrum.[18] VT ^{31}P NMR spectra were simulated using a two-site, non-mutual exchange model,[18,19] with the following input parameters for NiML and (η^2-H_2)NiML complexes: chemical shifts (δ), intrinsic linewidths (W) and relative equilibrium concentrations (C).

Explanation of Input Parameters for Simulation. Factors which could potentially contribute to the broadness of the observed ^{31}P NMR resonances include: (1) intrinsic linewidths (W) of NiML and (η^2-H_2)NiML; (2) broadening from quadrupolar nuclei; (3) broadening from coupling to other nuclei; (4) broadening from magnetic field inhomogeneity and sub-optimal shimming; and (5) broadening from chemical exchange.[11,18] In order to extract accurate exchange rates, it is critical to isolate the broadening arising from chemical exchange from that attributable to these other processes. In the case of our system, no quadrupolar nuclei are present, and the ^{31}P nuclei in NiML and (η^2-H_2)NiML are not coupled to any other nuclei (note: ^{31}P NMR spectra were collected with ^1H- and ^{13}C-decoupling). Both δ and W were found to vary slightly as a function of T. To be as precise as possible, both δ(T) and W(T) were measured for NiML (under 1 atm Ar) by VT ^{31}P NMR spectroscopy for each T. The same samples were then pressurized with 1 atm H_2, and VT ^{31}P NMR spectra were again collected at the same set of T. By collecting spectra for samples of NiML and (η^2-H_2)NiML at the exact same concentration and solution volume, in the same J. Young NMR tubes, and with the same NMR instrument (with automatic tuning and shimming with Bruker Topshim sequence), the irregular contributions of magnetic field inhomogeneity and sample shimming to the ^{31}P NMR lineshapes would be accounted for as much as possible in the measurements of intrinsic linewidths (W) at each T.

In contrast to NiML, a few assumptions were needed in order to estimate δ and W for the (η^2-H_2)NiML complexes because of the interconversion of (η^2-H_2)NiML and NiML species. We chose (OC)NiML as model complexes to estimate δ and W at a given T for (L')NiML (L' = H_2).[20] Because CO is bound irreversibly in (OC)NiML, no chemical exchange occurs under 1 atm of Ar. The average ratio of the linewidths of (OC)NiML to NiML was found to be close to unity (1.0 for Ga, 1.027 for In), and so those factors were used to estimate W for (η^2-H_2)NiML based on the measured W for NiML at a given T. By analogy, for NiAlL (**1**), for which no CO adduct had been isolated at the time of this study, the linewidth ratio of the bound (H_2) to unbound species was assumed to be ~ 1.0 (as was the case for M = Ga and In).

The relative concentrations (C) of NiML and (η^2-H_2)NiML at each T were based on either the relative peak integrations (for slow exchange) or the observed ^{31}P peak position (for fast exchange), as described in section B. Of note, iteration of the relative concentrations was performed to obtain the best fit for each experimental spectrum, and the final C values obtained were all nearly identical to the initial input values in all cases. With the known δ, W, and C input parameters for both NiML and (η^2-H_2)NiML for a given T, full lineshape iteration was then performed by variation of the exchange rate to obtain the best least-squares fit of the simulated spectra to the experimental spectra. The output of the simulation included the exchange rate that gave the best-fit simulation (and associated uncertainty) for each NiML sample (M=Al, Ga, In) at each T (all under 1 atm H_2).

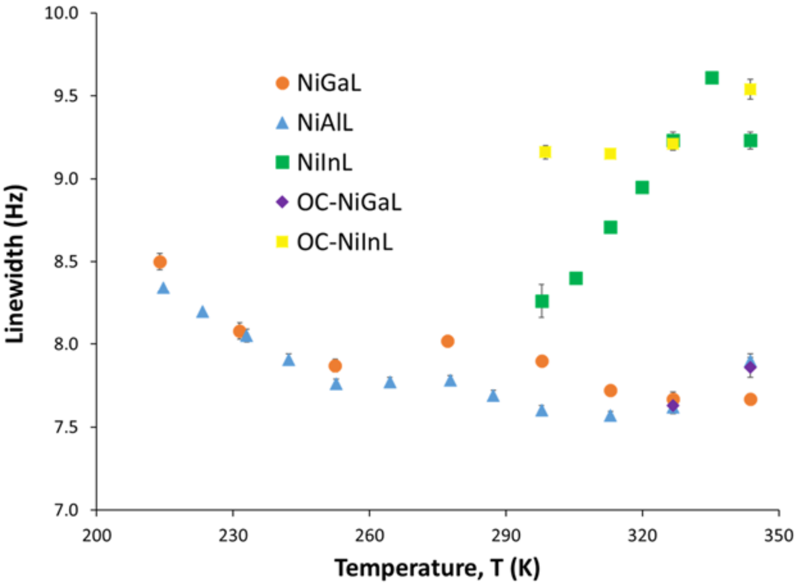

Figure S7. Linewidths (W in Hz) of VT ^{31}P NMR spectra (161.9 MHz) for NiML and (OC)NiML complexes in toluene-d_8 (~7.5 mM in 0.70 mL) under 1 atm Ar. The ratio of the linewidths of (OC)NiML at high T (> 300 K) relative to those of the corresponding NiML complexes was used to estimate the intrinsic linewidths of (η^2-H_2)NiML.

Determination of Rate Constants and Activation Parameters for H_2 Loss. The rate constants for H_2 loss from (η^2-H_2)NiML, k_{loss}, were also extracted at each T using equations S11-S12, in conjunction with the exchange rates determined via NMR lineshape simulations.[18] The derivation of an expression for k_{loss} as a function of these variables is shown in the series of equations below. Chemical exchange occurs via unimolecular H_2 loss from (η^2-H_2)NiML and subsequent binding of H_2 to NiML, where H_2 loss is the rate-limiting step for self-exchange.

$$\mathrm{rate_{ex}} \cong \mathrm{rate_{loss}} = k_{\mathrm{loss}} \cdot [(\mathrm{H_2})\mathrm{NiML}] \qquad \text{(S11)}$$

$$k_{\mathrm{loss}} = \frac{\mathrm{rate_{ex}}}{[(\mathrm{H_2})\mathrm{NiML}]} \qquad \text{(S12)}$$

Upon obtaining k_{loss} for complexes **1**−H_2, **2**−H_2, and **3**−H_2 at various T, Eyring plots of ln(k_{loss}/T) vs. 1/T allow for the activation parameters for H_2 loss ($\Delta H^{\ddagger}_{loss}$, $\Delta S^{\ddagger}_{loss}$, and $\Delta G^{\ddagger}_{loss}$) to be determined. Finally, comparison of $\Delta G^{\ddagger}_{loss}$ values for H_2 loss and ΔG°_{1M} values for H_2 binding permits the tabulation of the free energy of activation values for H_2 binding ($\Delta G^{\ddagger}_{bind}$).

D. Additional Computational Details

Density functional theory (DFT) calculations were performed using the Gaussian 09 program package.[21] Four functionals (M06-L,[22] M06-D3, PBE0,[23] and PBE0-D3) and five basis sets (denoted as bs0 to bs4, Table S3) were evaluated. The TZ2P[24] basis set was used for EDA analysis,[25] as described below.

Table S3. Basis sets descriptions

Basis Set	Element				
Denotation	In	H_2	Ni	N,P	C,H
bs0	def2-TZVPP&SDD	def2-TZVP	def2-TZVPP	def2-TZVP	def2-SVP
bs1	def2-TZVPP&SDD	def2-TZVPP	def2-TZVPP	def2-TZVP	def2-SVP
bs2	SDD & SDD	def2-TZVP	def2-TZVPP	def2-TZVP	def2-SVP
bs3	LANL2DZ	6-31G(d)	6-31G(d)	6-31G(d)	6-31G(d)
bs4	LANL2DZ	6-311G(d,p)	6-311G(d,p)	6-311G(d,p)	6-311G(d,p)
TZ2P	TZ2P	TZ2P	TZ2P	TZP	DZP

Energy Decomposition Analysis

Energy decomposition analysis (EDA),[25,26] as implemented in the Amsterdam Density Functional (ADF 2016)[27,28] program package, was applied for the elucidation of the contributions to H_2–Ni and N_2–Ni bonding interactions. The (η^2-H_2)NiML complex is fragmented into H_2 and NiML, and the (N_2)NiML complex is fragmented into N_2 and NiML. The EDA interaction energy is calculated by taking the electronic energy difference between the complex and its constituent fragments. EDA interaction energy is denoted as "ΔE_{int}", and includes neither the deformation energy of the fragments nor any thermal effects. The relationship between ΔE_{int} and the binding free energy in solution, ΔG_{sol}, is shown in equation S13.

$$\Delta G_{sol} = \Delta E_{int} + \Delta E_{\text{deformation}} + \Delta\Delta G_{solvation} + \Delta\Delta G_{thermal} \qquad \text{(S13)}$$

$\Delta E_{\text{deformation}}$ results from deforming the fragments from their optimal equilibrium structures to the geometries and electronic states they acquire in the adduct complex. $\Delta\Delta G_{solvation}$ is the solvation energy of the binding reaction, or the energy difference upon moving from the gas phase into solution. $\Delta\Delta G_{thermal}$ is the thermal correction to the free energy for the binding reaction.

EDA breaks the total interaction energy into four components:

$$\Delta E_{int}\ (\text{EDA}) = \Delta E_{elstat} + \Delta E_{Pauli} + \Delta E_{orb} + \Delta E_{disp} \qquad \text{(S14)}$$

ΔE_{elstat} corresponds to the attractive, quasi-classical electrostatic interaction between the charge densities of the fragments. ΔE_{Pauli} corresponds to repulsive energy between electrons of the same spin due to the anti-symmetrized nature of the wavefunction. ΔE_{orb} is obtained from the relaxation (i.e. mixing) of the fragment orbitals. Finally, ΔE_{disp} describes the dispersive effects between the two fragments.

The extended transition state – natural orbitals for chemical valence (ETS-NOCV) method,[29] in combination with the energy decomposition scheme, is used to decompose the orbital interaction ΔE_{orb} into contributions from specific NOCV pairs. The deformation density, $\Delta\rho$, is partitioned into the different components (σ, π, δ) of the chemical bond. Each NOCV pair shows the electron flow, as pictured by red → blue, and allows for assignment of the orbital interactions between the two fragments. ETS-NOCV calculations were performed with the ADF program using PBE0-D3 with the TZ2P basis sets. Relativistic effects for In were included by applying the zeroth-order regular approximation (ZORA).[30] It should be noted that because the ETS-NOCV analysis is not completely implemented for meta-GGA or meta-hybrid functionals, such as M06-L and M06, we instead used the PBE0-D3 functional for these calculations.

II. Neutron and X-ray structures of 3−H$_2$ and NMR characterization of 1−H$_2$

Table S4. Structural parameters for **3**−H$_2$ (X-ray and neutron data at 100 K)

Metric	X-ray	neutron	Overlay of X-ray and neutron structures [c]
Ni-In (Å)	2.4789(2)	2.485(18)	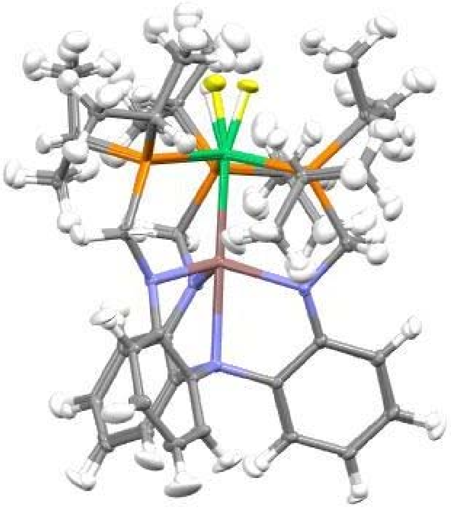
FSR [a]	0.93	0.93	
Ni-P	2.2502(4)	2.239(13)	
	2.2521(4)	2.257(14)	
	2.2831(4)	2.284(13)	
In-N$_{amide}$	2.1097(10)	2.104(16)	
	2.1127(11)	2.135(16)	
	2.1217(12)	2.139(17)	
M-N$_{apical}$	2.3658(11)	2.388(18)	
Ni to P$_3$-plane (Å)	0.29	0.31	
In to N$_3$-plane (Å)	0.50	0.52	
Ni-H	1.65(2), 1.58(2) [b]	1.61(2), 1.61(2)	
H-H	0.92(3) [b]	0.80(2)	
P-Ni-P angle	112.16(2)	111.2(5)	
	120.20(2)	120.7(5)	
	122.76(2)	122.6(5)	
N$_{amide}$-In-N$_{amide}$ angle	111.73(4)	111.4(7)	
	115.80(5)	115.9(8)	
	116.48(4)	115.1(7)	
Ni-In-N$_{apical}$ angle	178.63(3)	178.0(7)	
H-Ni-H angle	33.1(9)	28.9(9)	

[a] Formal shortness ratio using Alvarez covalent radii for Ni, Ga, and In.[31] [b] The high quality of the X-ray structure (data collected to ~0.6 Å) allowed for the placement of the H$_2$ ligand from the difference map. However, the Ni−H and H−H bond distances from X-ray diffraction studies are not exceedingly reliable, which prompted their more precise determination via neutron diffraction. [c] In the overlay, the H$_2$ unit is shown in yellow for the neutron structure and in white for the X-ray structure.

Table S5. Selected structural parameters for NiInL complexes (**3**, **3**−H_2, and **3**−N_2).

	3	**3**-N_2	**3**-H_2 [a]
Ni-In	2.4573(12)	2.5256(7)	2.4789(2)
FSR [b]	0.92	0.95	0.93
Ni-P (*avg*)	2.252	2.311	2.262
Ni-H/N	–	1.848(3)	1.61(2), 1.61(2)
In-N_{apical}	2.309(6)	2.384(5)	2.366(1)
In-N_{amide} (*avg*)	2.119	2.1187	2.115
Ni to P_3-plane	0.23	0.38	0.29
In to N_3-plane	0.48	0.54	0.50

[a] Data shown for **3**−H_2 is from X-ray structure reported in this work at 100 K, with Ni−H distances given from the neutron structure. [b] FSR defined in Table S4, footnote a.

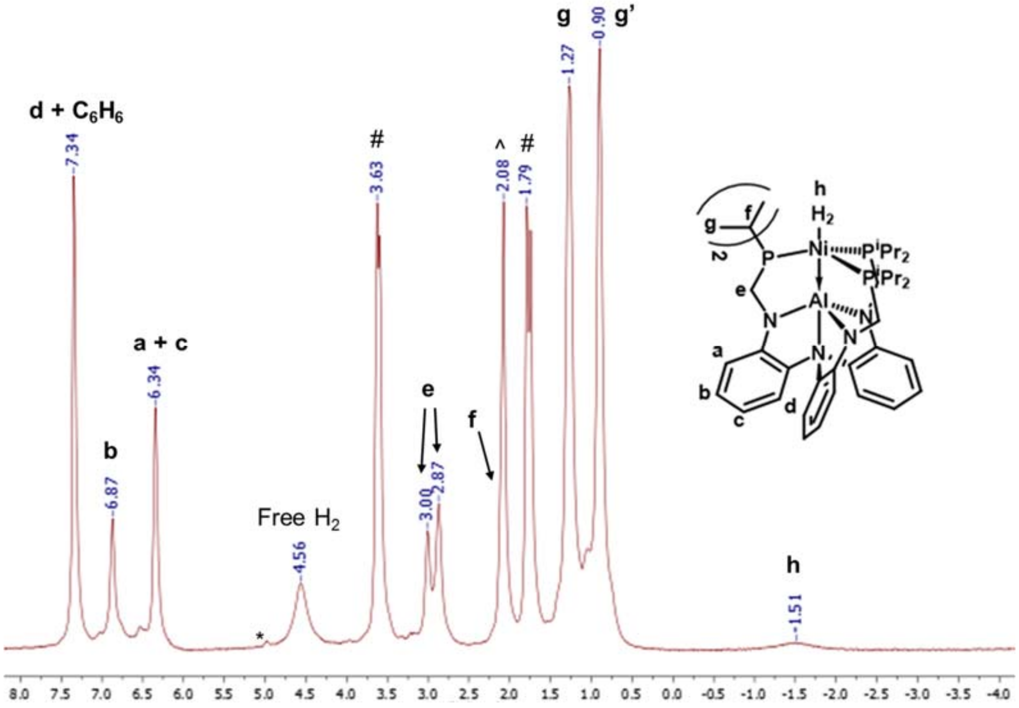

Figure S8. ^{1}H NMR spectrum (500 MHz, THF-d_8, 232 K) of (η^2-H_2)NiAlL (**1**-H_2) generated *in-situ* by exposing NiAlL (~50 mM) to 34 atm H_2. Low T and/or elevated H_2 pressure are needed to drive the binding equilibrium toward **1**−H_2; refer to Figure S9 for the full VT ^{1}H NMR profile. Residual solvent peaks of THF (#), toluene (^), and C_6H_6 are denoted, and a small N*H* peak of the $NiLH_3$ ^{31}P chemical shift standard (that forms from residual H_2O) is denoted at 4.99 ppm (*).

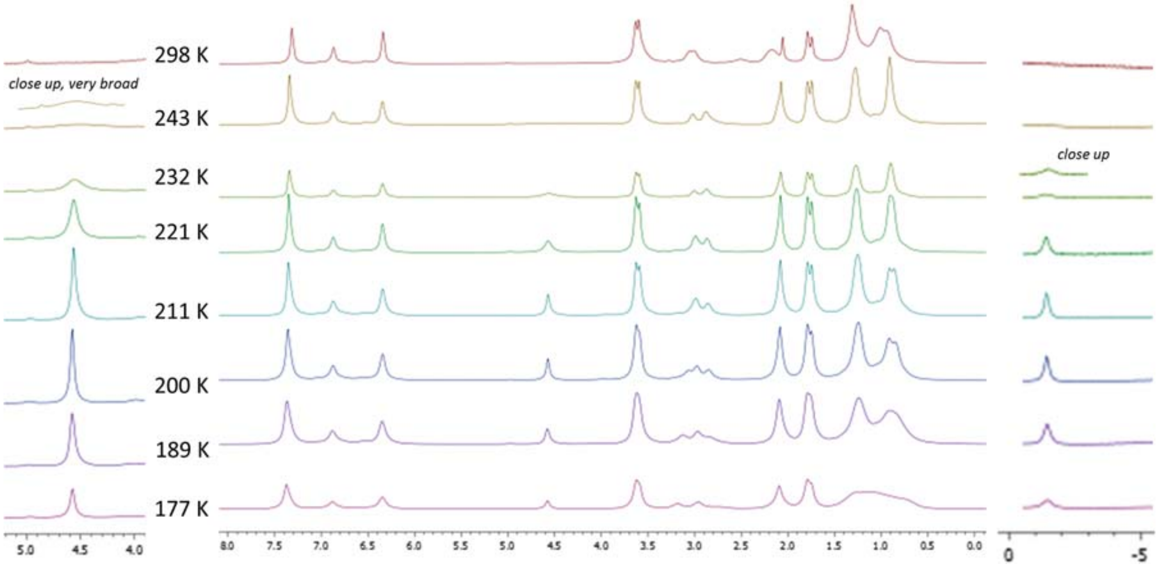

Figure S9. Stacked VT ^1H NMR (500 MHz) of (η^2-H_2)NiAlL (**1**−H_2) generated *in-situ* from exposure of NiAlL (**1**) to 34 atm H_2 in THF-d_8 (~50 mM). Close-ups of the free H_2 region (4 to 5 ppm; left) and the bound H_2 region (−5 to 0 ppm; right) are also shown. At 298 K, no resonances for bound or free H_2 can be identified, suggesting that H_2 exchange is rapid relative to the ^1H NMR timescale. At T ≤ 232 K, chemical exchange slows and distinct peaks for free and bound H_2 are observed at 4.57 and −1.5 ppm, respectively.

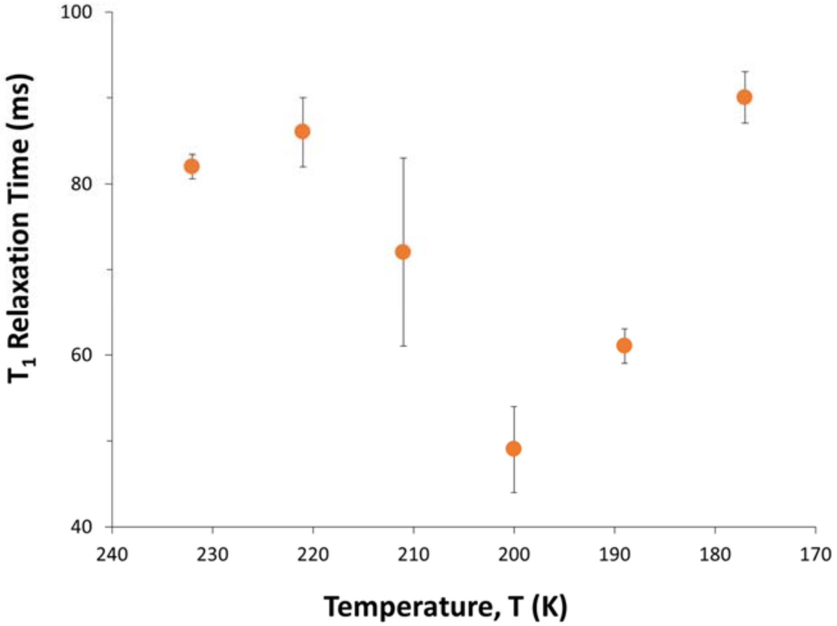

Figure S10. Plot of T_1 relaxation time (in ms, at 500 MHz) of the bound H_2 resonance of (η^2-H_2)NiAlL (**1**−H_2) vs. T (see experimental conditions and VT ^1H NMR profile in Figure S9 above). T_1 values were obtained every ~10 K from 177 K to 232 K, with significant broadening of the bound H_2 resonance precluding T_1 measurements at higher T. The short T_1(min) value of ≤ 49 (±5) ms at 200 K is indicative of an intact H_2 ligand. Direct comparison of the T_1(min) value for **1**−H_2 to those previously reported[32] for **2**−H_2 and **3**−H_2 is complicated by the fact that the latter were measured in toluene-d_8 (vs. THF-d_8) at lower concentrations (~15 mM vs. ~50 mM) and under lower H_2 pressure (1 atm vs. 34 atm).

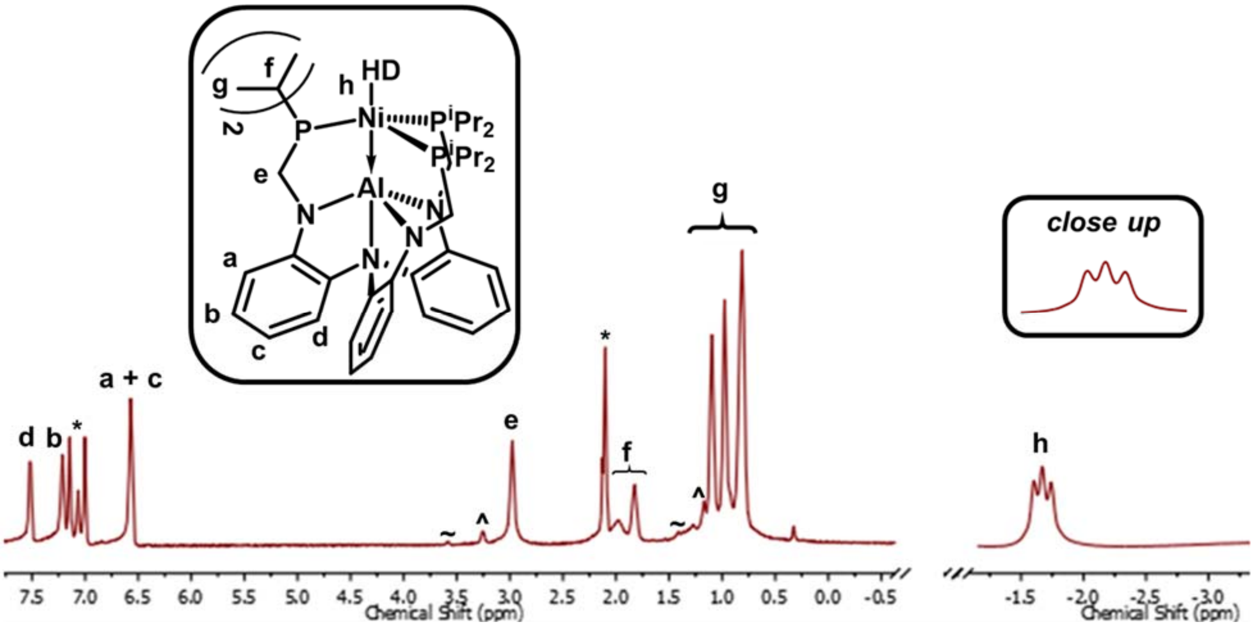

Figure S11. ^{1}H NMR spectrum (500 MHz, toluene-d$_8$, 213 K) of (η^2-HD)NiAlL (**1**-HD) generated *in situ* by exposing NiAlL (~7.5 mM) to 3.8 atm HD. Residual solvent peaks of toluene (*), THF (~), and diethyl ether (^) are denoted, and a close up of the hydride region is also shown (J_{HD} = 34.4 Hz; right).

III. Data for Thermodynamic Binding Studies

Control VT NMR Experiments under Ar

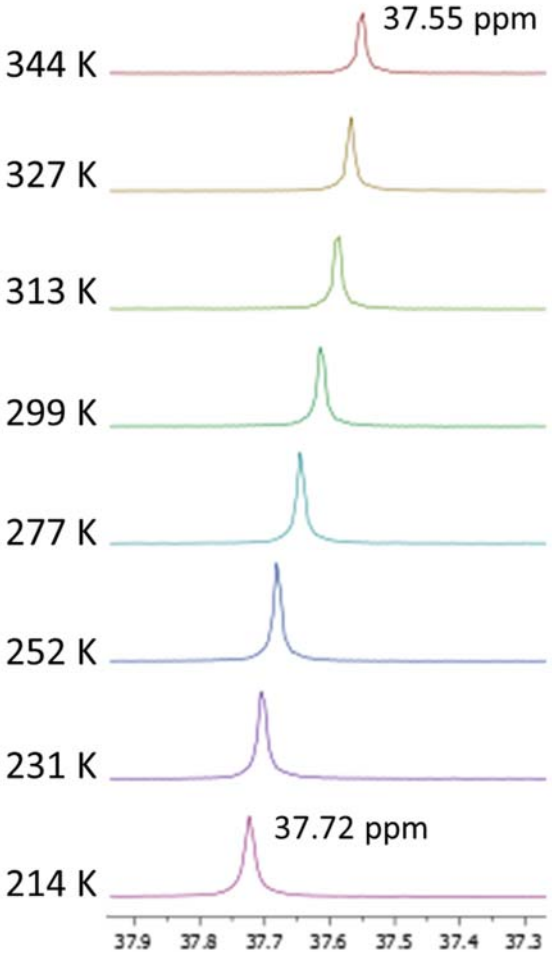

Figure S12. Stacked VT ^{31}P NMR spectra (161.9 MHz) for NiGaL (**2**) in toluene-d_8 under 1 atm Ar from 214 to 344 K. The observed chemical shift (δ) changes by < 0.2 ppm in the spectra shown, and only changes by < 0.5 ppm from 193 K to 370 K. This control experiment shows that the chemical shift of **2** is virtually invariant with T in the absence of H_2 or N_2 gas, and thus significant changes in ^{31}P δ upon varying T under H_2 or N_2 gas are due to interactions of H_2 or N_2 with NiGaL.

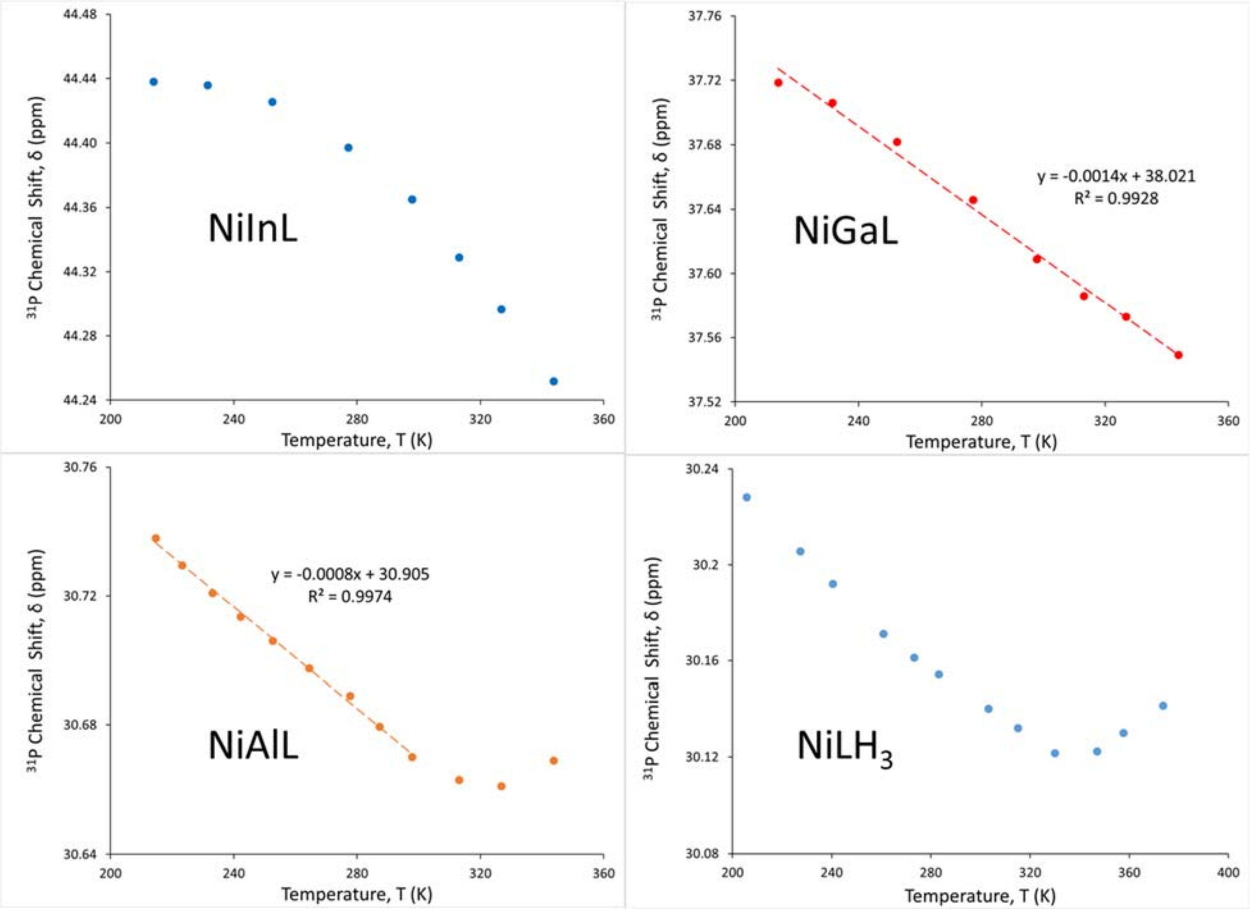

Figure S13. ^{31}P NMR chemical shift dependence on temperature, δ(T), for NiAlL (**1**), NiGaL (**2**), NiInL (**3**), and $NiLH_3$ (**4**) in toluene-d_8 under 1 atm Ar. Over the T range of 213 to 344 K, the observed chemical shift changes by < 0.08, < 0.18, < 0.20, and < 0.12 ppm for **1**, **2**, **3**, and **4**, respectively. δ(T) for NiML (plotted above) were used as input parameters for gNMR simulations of ^{31}P NMR lineshapes (Figures S42-S44). ^{31}P resonances observed in binding studies were referenced relative to the known chemical shifts of a $NiLH_3$ (**4**)[33] internal standard at all T.

VT NMR Experiments for H_2 Binding

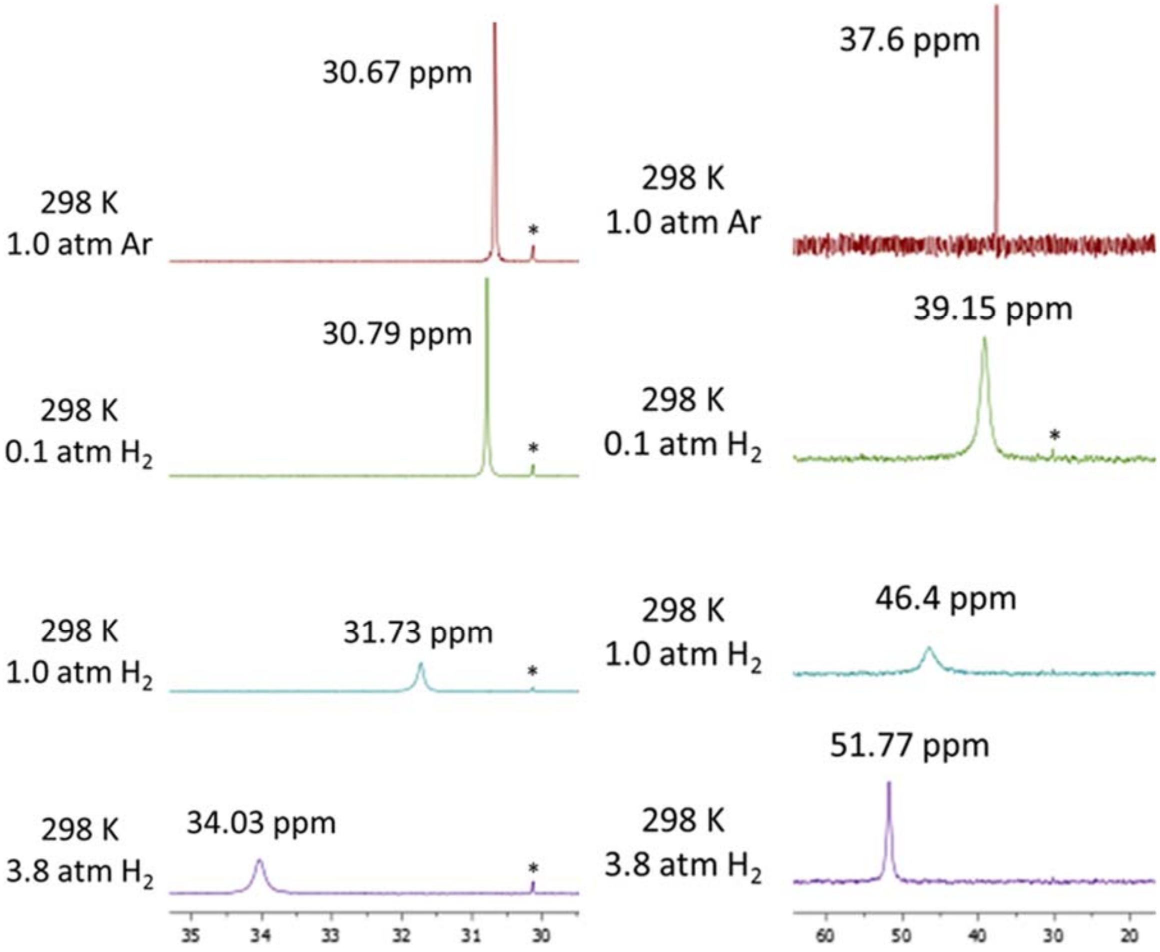

Figure S14. Comparison of ^{31}P NMR spectra (161.9 MHz) for NiAlL (**1**, left) and NiGaL (**2**, right) at 298 K in toluene-d_8 under various pressures of H_2 (0.1, 1.0, and 3.8 atm) and 1 atm Ar. The lone ^{31}P resonance shifts downfield with increasing H_2 pressure as the equilibrium shifts towards (η^2-H_2)NiML. The breakdown of the fast-exchange assumption is indicated by peak broadening.[1,2] Hence, thermodynamic binding studies were performed under elevated H_2 pressures: 34 atm H_2 for **1**, and 6.8 and 13.6 atm H_2 for **2**. A small amount of the chemical shift standard, $NiLH_3$ (~30.1 ppm), is denoted by an asterisk (*).

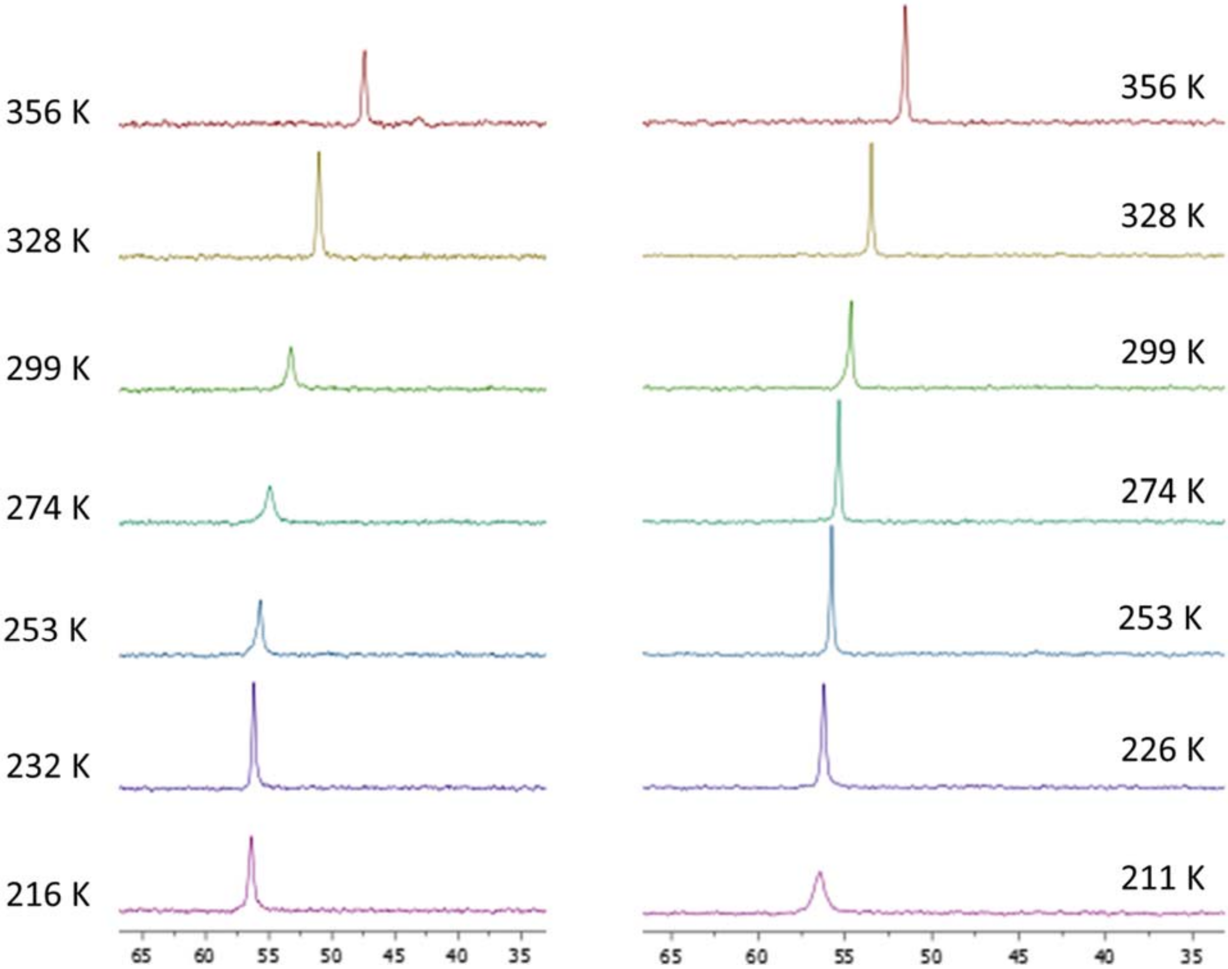

Figure S15. Stacked VT ^{31}P NMR spectra (202.4 MHz) of NiGaL (**2**) under 13.6 atm H_2 (left) and 34 atm H_2 (right) obtained in toluene-d_8 (~15 mM in 0.30 mL) from 210 to 360 K. Data obtained under 13.6 atm H_2 was used to obtain a van't Hoff plot (Figure S16), and averaging the results obtained at 6.8 atm and 13.6 atm H_2 gave the final results for the thermodynamic parameters for H_2 binding to **2** (Tables 2 and S2). Low T chemical shift convergence under 34 atm H_2 was used to determine the chemical shift of **2**−H_2.

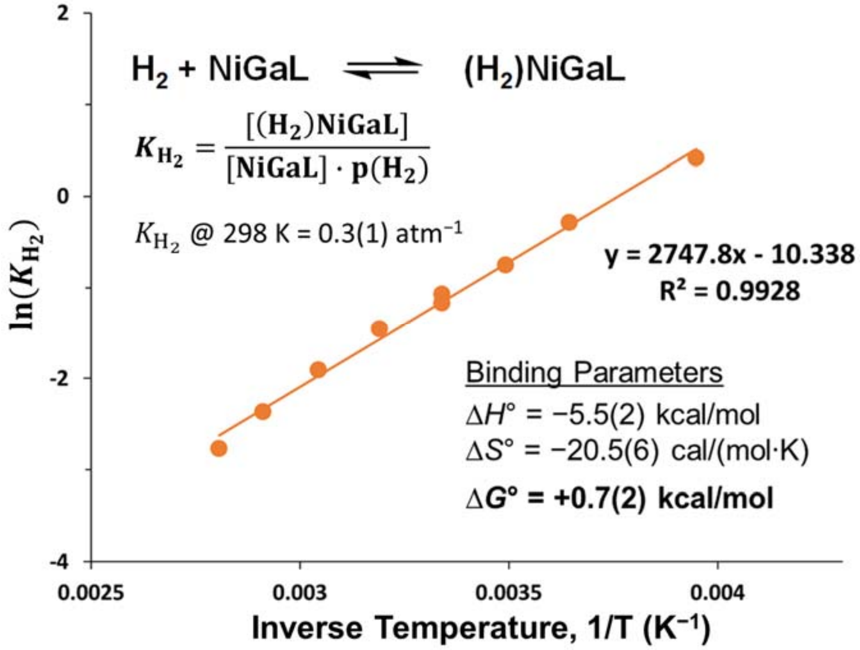

Figure S16. van't Hoff plot of ln(K_{H_2}) vs. 1/T for H_2 binding equilibrium to NiGaL (**2**), based on VT ^{31}P NMR data collected under 13.6 atm H_2 from 250 to 356 K. The thermodynamic binding parameters (Δ*H*°, Δ*S*°, and Δ*G*°) and the associated uncertainties obtained from linear regression are also displayed above (standard state: 298 K, 1 atm H_2, 1 M of all other species, toluene-d_8). The final Δ*G*° value for H_2 binding to **2** in toluene (0.6 ± 0.3 kcal/mol) was determined by a combined van't Hoff plot analysis of both the 6.8 and 13.6 atm datasets (Table S2).

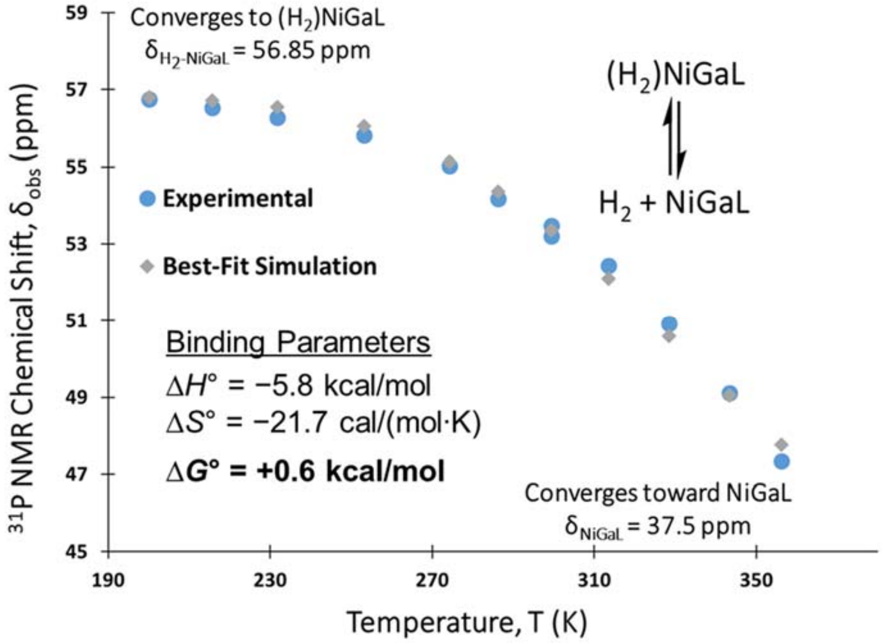

Figure S17. Plot of ^{31}P NMR chemical shift (δ_{obs}) vs. T for VT ^{31}P NMR data collected for NiGaL (**2**) under 13.6 atm of H_2 in toluene-d_8 from 193 to 356 K, with experimental data points (show as blue circles) and best-fit simulations (shown as gray diamonds).

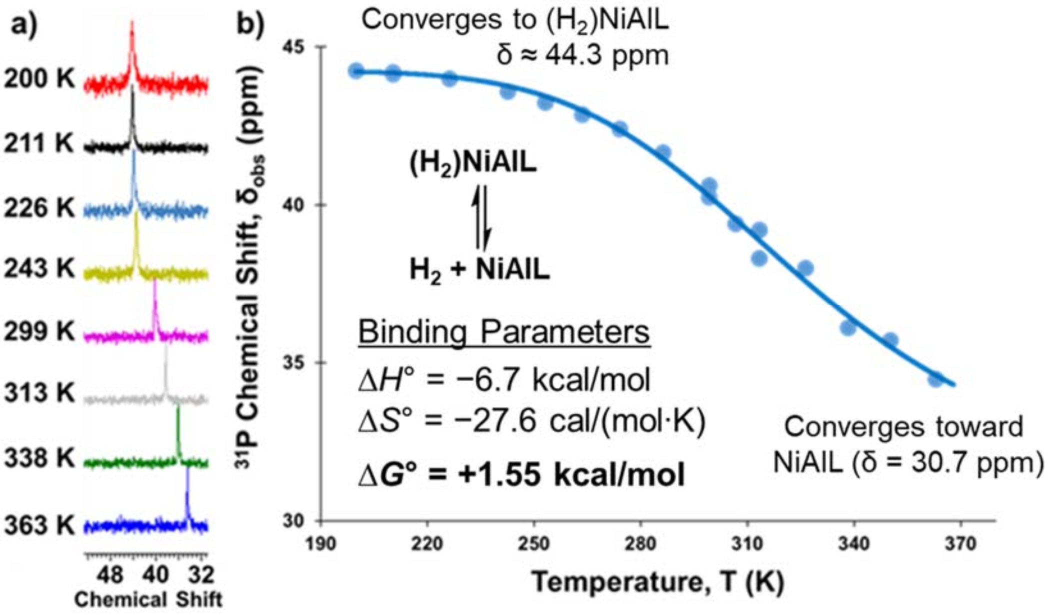

Figure S18. (a) Stacked VT ^{31}P NMR spectra (161.9 MHz) of NiAlL (**1**) in toluene-d_8 under 34 atm H_2 from 210 to 363 K. (b) Plot of observed ^{31}P NMR chemical shift (δ_{obs}) vs. T, where experimental data are shown as points and the solid trace represents the best-fit curve obtained by non-linear fitting of thermodynamic parameters (best-fit parameters shown above).

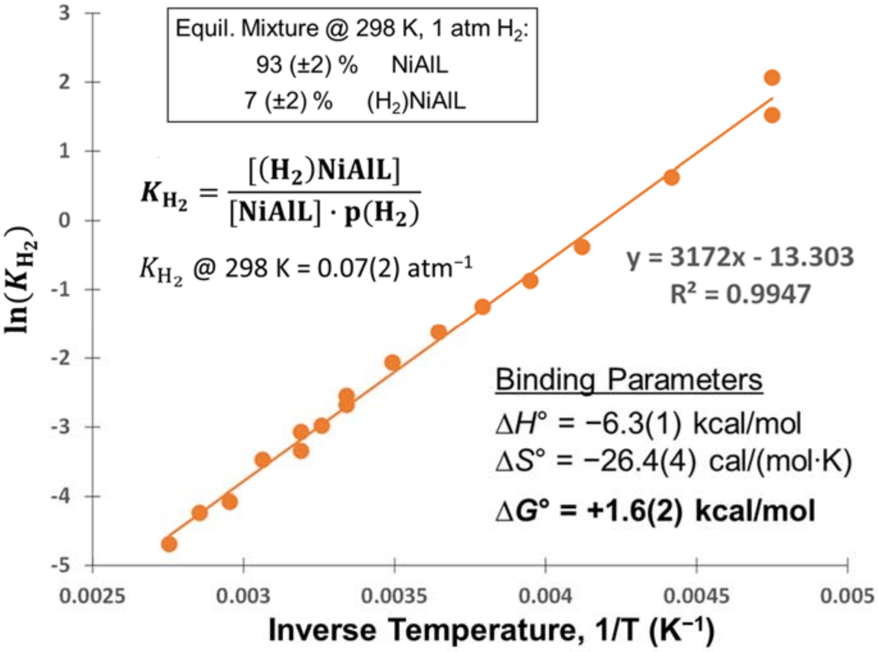

Figure S19. van't Hoff plot of ln(K_{H_2}) vs. 1/T for H_2 binding to NiAlL (**1**), based on VT ^{31}P NMR data collected under 34 atm H_2 from 210 to 363 K. The thermodynamic binding parameters and the associated uncertainties obtained from linear regression are also displayed above (standard conditions: 298 K, 1 atm H_2, 1 M of all other species, toluene-d_8).

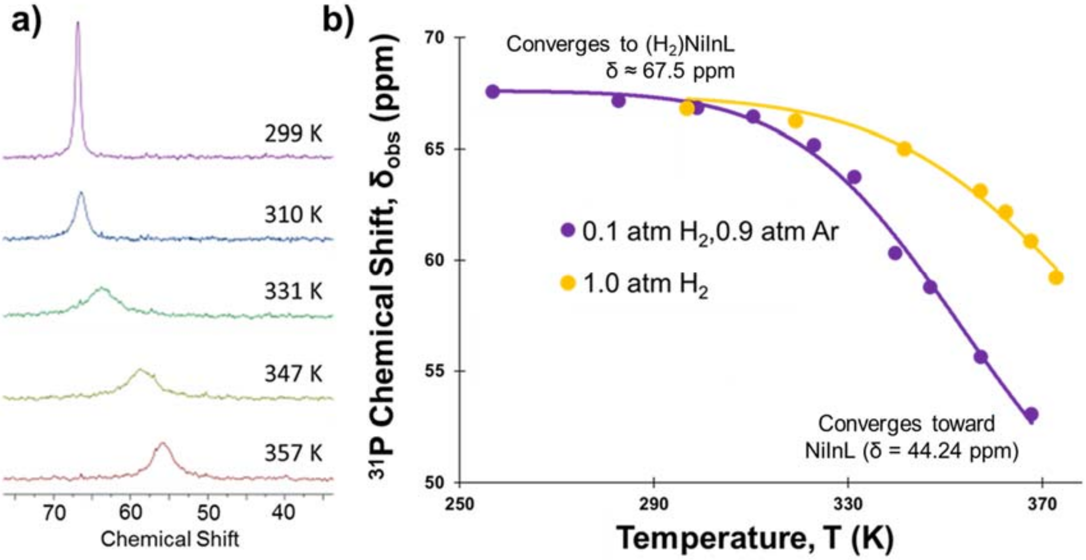

Figure S20. (a) Stacked VT ^{31}P NMR (161.9 MHz) of NiInL (**3**) in toluene-d$_8$ (~14 mM in 0.42 mL) under 1 atm of 10% H_2/90% Ar mixture (0.1 atm H_2, or ~1.5 equiv H_2 relative to **3**) from 299 to 357 K. (b) Plots of ^{31}P NMR chemical shift (δ_{obs}) vs. T for VT ^{31}P NMR data collected for **3** under 0.1 and 1.0 atm H_2. The observed peak broadening concurrent with peak shifting indicates that fast exchange may not be the best assumption,[1,2] and the typical remedy of increasing the H_2 pressure to allow faster chemical exchange cannot be applied in this case due to prohibitively strong H_2 binding to **3**.

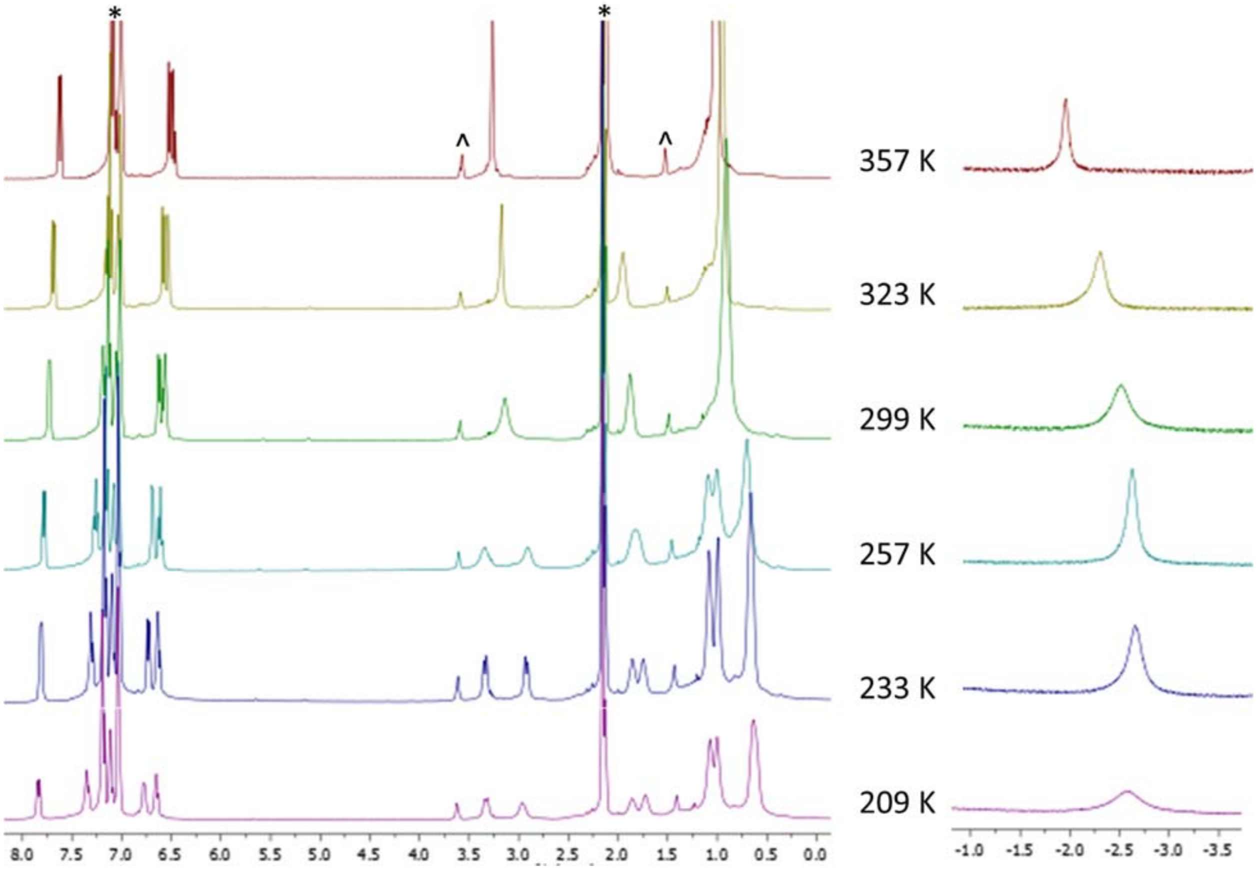

Figure S21. Stacked VT ^{1}H NMR (400 MHz) of NiInL (**3**) in toluene-d$_8$ (~14 mM in 0.42 mL) under 1 atm of 10% H_2/90% Ar mixture (0.1 atm H_2). Residual solvent peaks for toluene (*) and THF (^) are denoted in the top spectrum. Based on the volumes of the J. Young tube and solvent, ~1.5 equiv of H_2 were introduced relative to **3**. A bound H_2 resonance is observable at all T from 209 to 367 K. The peak shifts from ~1.8 ppm at 357 K to its typical position at ~2.6 ppm at lower T, indicating a relatively fast equilibrium between free H_2 (~4.57 ppm) and Ni-bound H_2 relative to the ^{1}H NMR timescale.

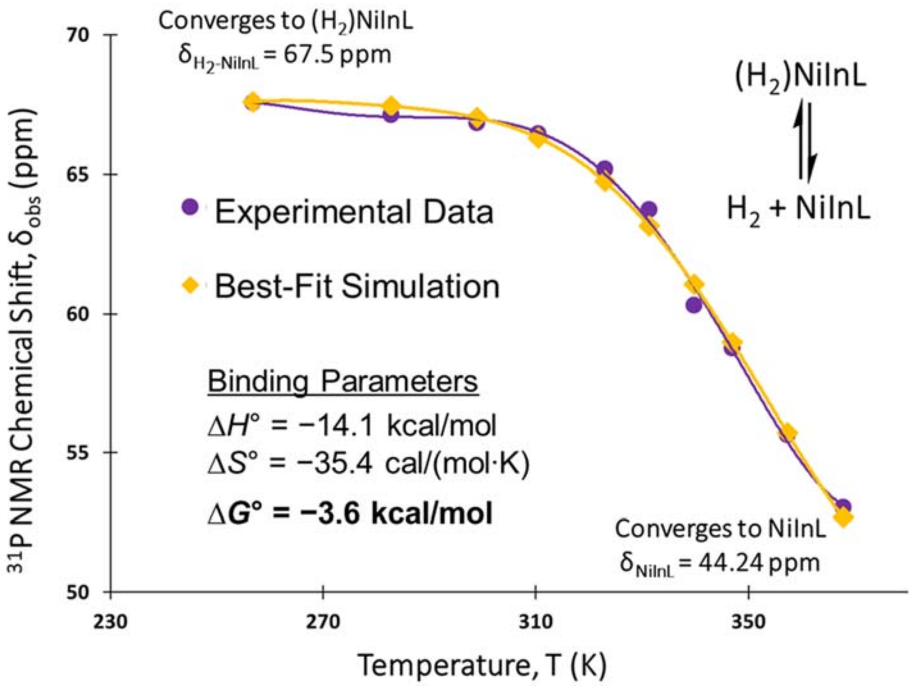

Figure S22. Plot of ^{31}P NMR chemical shift (δ_{obs}) vs. T for VT ^{31}P NMR data collected for NiInL (**3**) under 1 atm of 10% H_2/90% Ar mixture from 255 to 368 K. Experimental data points are shown as purple circles, while the best-fit profile is shown as orange diamonds.

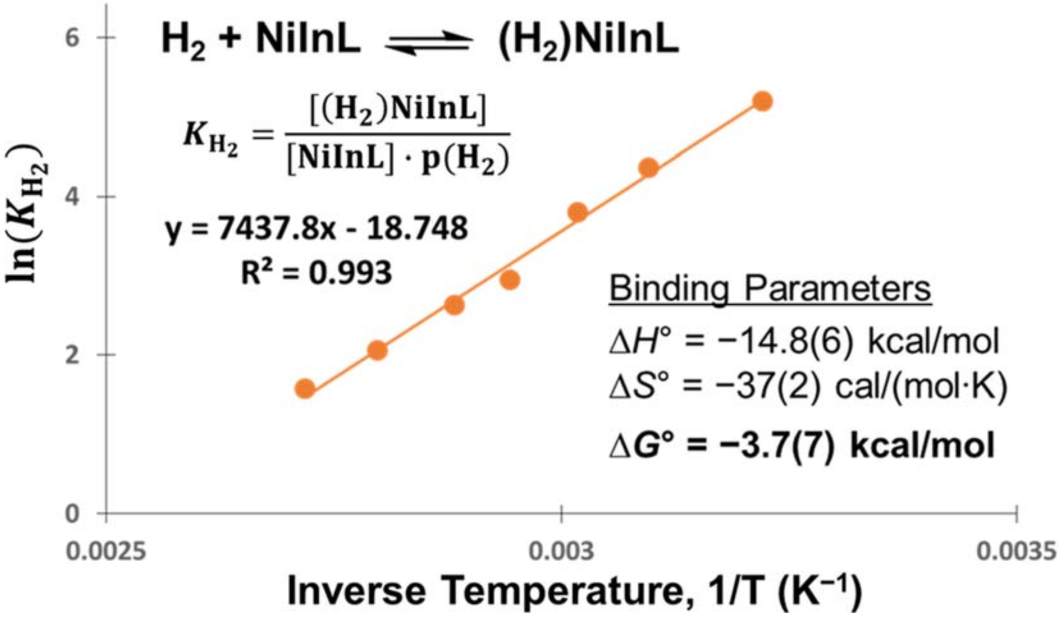

Figure S23. van't Hoff plot of $\ln(K_{H_2})$ vs. 1/T for H_2 binding equilibrium to NiInL (**3**), based on VT ^{31}P NMR data collected under 0.1 atm H_2 from 299 to 368 K. The thermodynamic binding parameters and the associated uncertainties obtained from linear regression are also displayed above (standard conditions: 298 K, 1 atm H_2, 1 M of all other species, toluene-d_8).

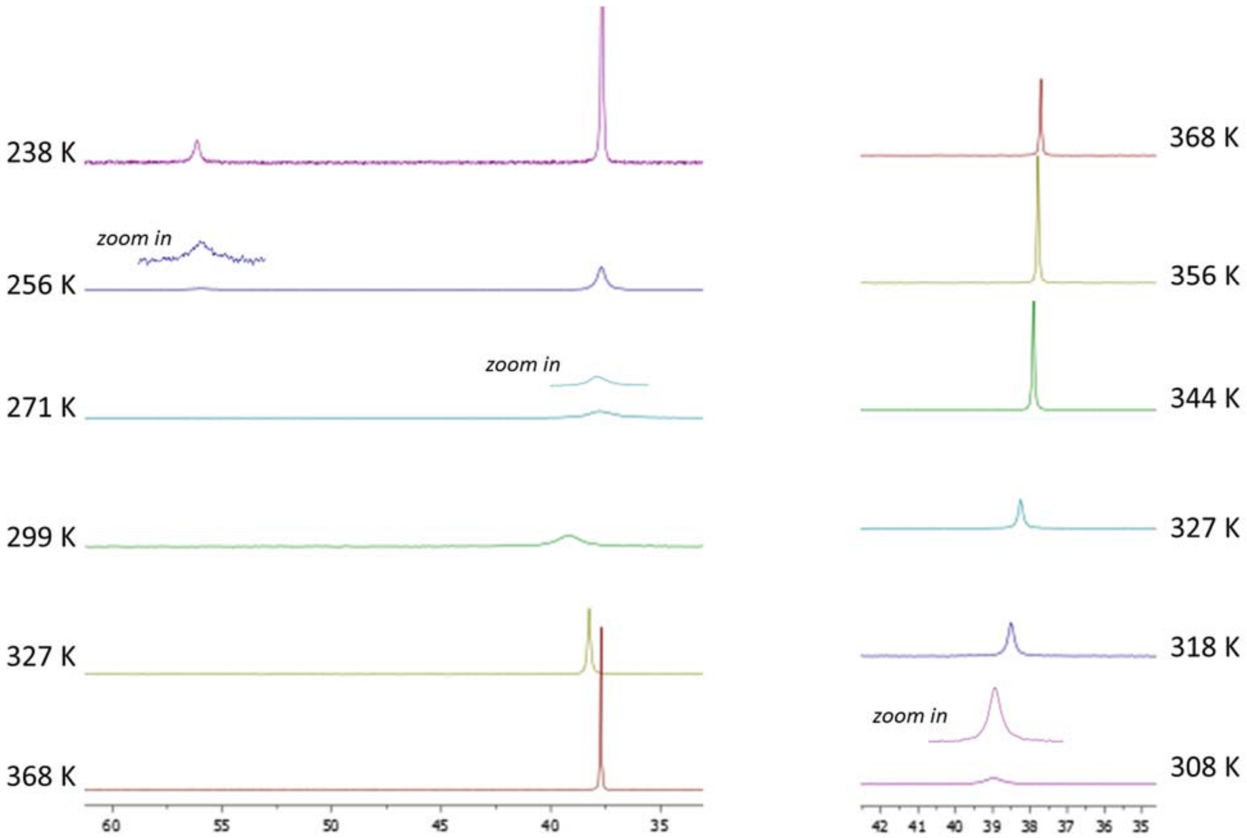

Figure S24. Stacked VT ^{31}P NMR (161.9 MHz) of NiGaL (**2**) in toluene-d_8, (~13.5 mM in 0.45 mL) under 1 atm of 10% H_2/90% Ar mixture (0.1 atm H_2, ~1.5 equiv H_2). The stacked spectra show the ^{31}P NMR profiles for both the entire T range examined (left, 238 K to 368 K) and the fast/fast-intermediate exchange regime (right, T > 300 K). Chemical exchange is slow < 260 K, with distinct peaks for both **2** and **2**−H_2 observable. This VT study allows for comparison between the H_2 binding parameters for complex **2** obtained under fast-intermediate exchange conditions at low H_2 pressure (0.1 atm) and those determined under higher H_2 pressures where rigorously fast chemical exchange is occurring (6.8, 13.6 atm). This empirical difference for complex **2** was utilized as one means of better estimating H_2 binding parameters to complex **3** (refer to Figures S20-S23 and S26), which were only obtained under 0.1 atm H_2.

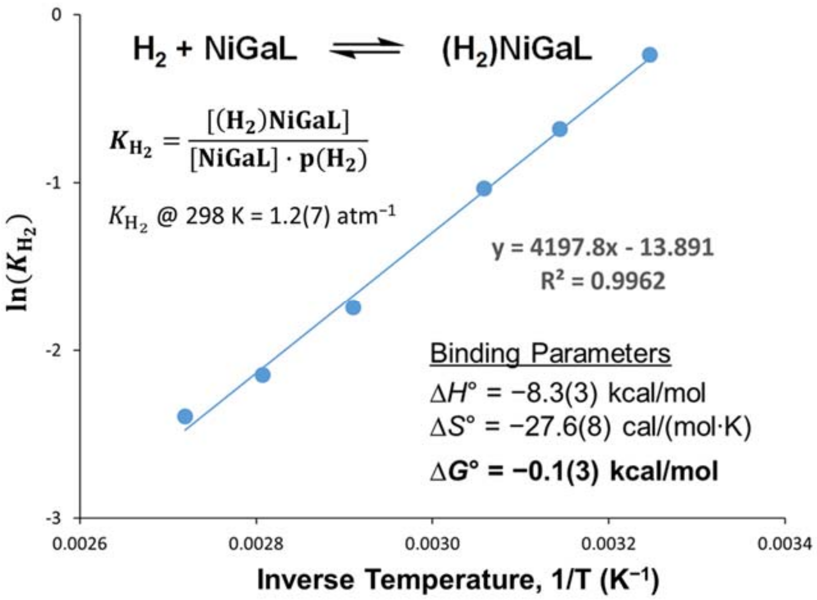

Figure S25. van't Hoff plot of $\ln(K_{H_2})$ vs. 1/T for H_2 binding to NiGaL (**2**), based on VT ^{31}P NMR data collected at T > 300 K under 0.1 atm H_2. The thermodynamic binding parameters and the associated uncertainties obtained from linear regression are also displayed above (standard conditions: 298 K, 1 atm H_2, 1 M of all other species, toluene-d_8). These values are expected to deviate from those obtained under high H_2 pressures because the assumption of fast exchange is not rigorously valid for this dataset. Δ*G*° for H_2 binding to **2** was found to be −0.1(3) kcal/mol under 0.1 atm H_2, whereas it was found to be +0.6(3) kcal/mol under ideal fast-exchange conditions (6.8 and 13.6 atm H_2). Thus, an empirical Δ*G*° correction factor of +0.7 kcal/mol was applied to Δ*G*° obtained under 0.1 atm H_2 for **3**, which gives a better estimate of Δ*G*° = −3.0(7) kcal/mol for H_2 binding to **3**.

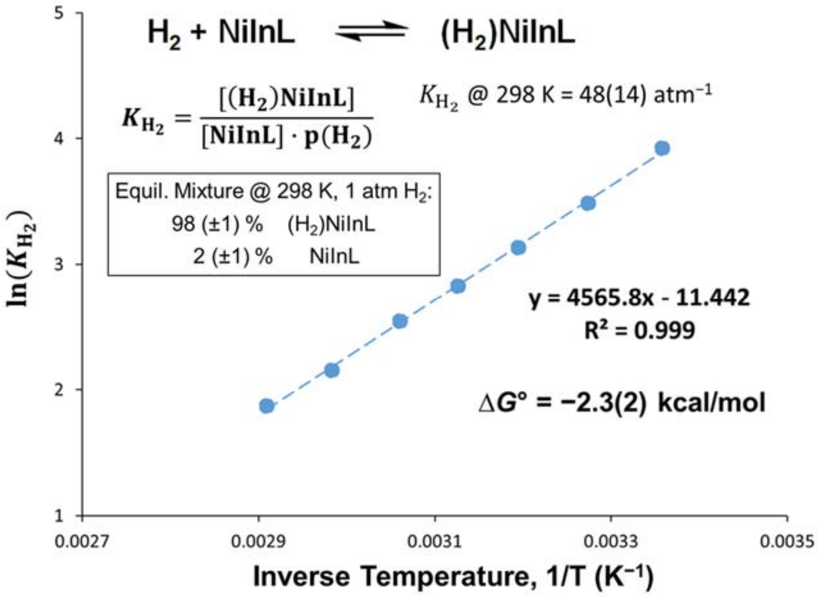

Figure S26. van't Hoff plot of $\ln(K_{H_2})$ vs. 1/T for H_2 binding to NiInL (**3**) based on relative concentrations of **3** and **3**−H_2 determined from best-fit lineshape simulations for VT ^{31}P NMR data collected under 1.0 atm H_2 from 298 K to 344 K. Standard conditions are 298 K, 1 atm H_2, and 1 M of all other species in toluene-d_8. Importantly, the Δ*G*° value for H_2 binding to **3** from this plot, −2.3(2) kcal/mol, is within experimental error of the empirically corrected value of −3.0(7) kcal/mol.

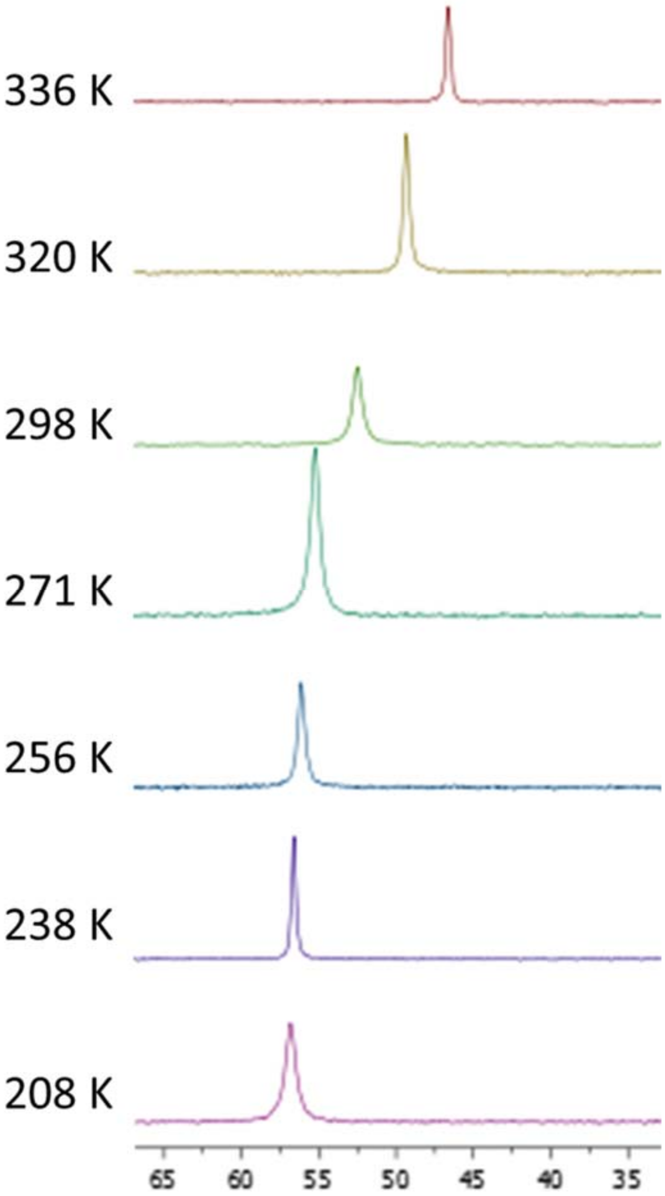

Figure S27. Stacked VT ^{31}P NMR spectra (161.9 MHz) of NiGaL (**2**) in THF (~12.2 mM in 0.62 mL) under 3.8 atm H_2 from 218 K to 336 K. This VT study was carried out to investigate the effect of changing the solvent from toluene to THF on the binding equilibrium of H_2 to **2**. The validity of the fast exchange assumption can be seen qualitatively in the lack of significant ^{31}P peak broadening, which allowed for the inclusion of all T > 210 K in the van't Hoff plot (Figure S29).

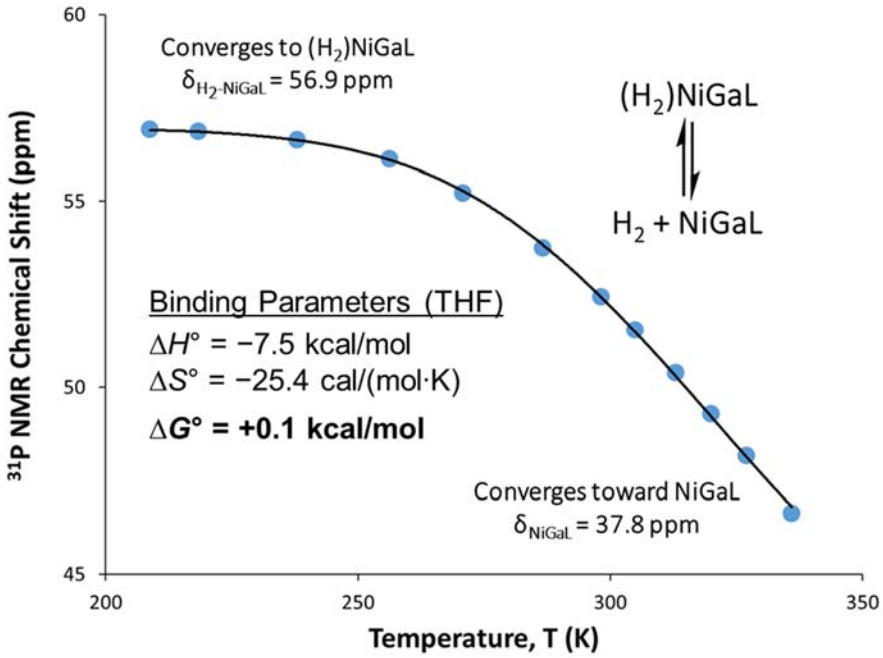

Figure S28. Plot of ^{31}P NMR chemical shift (δ_{obs}) vs. T for VT ^{31}P NMR data collected for NiGaL (**2**) under 3.8 atm of H_2 in THF, with experimental data shown as blue circles and the best non-linear fit shown as a black line (with best-fit parameters shown above).

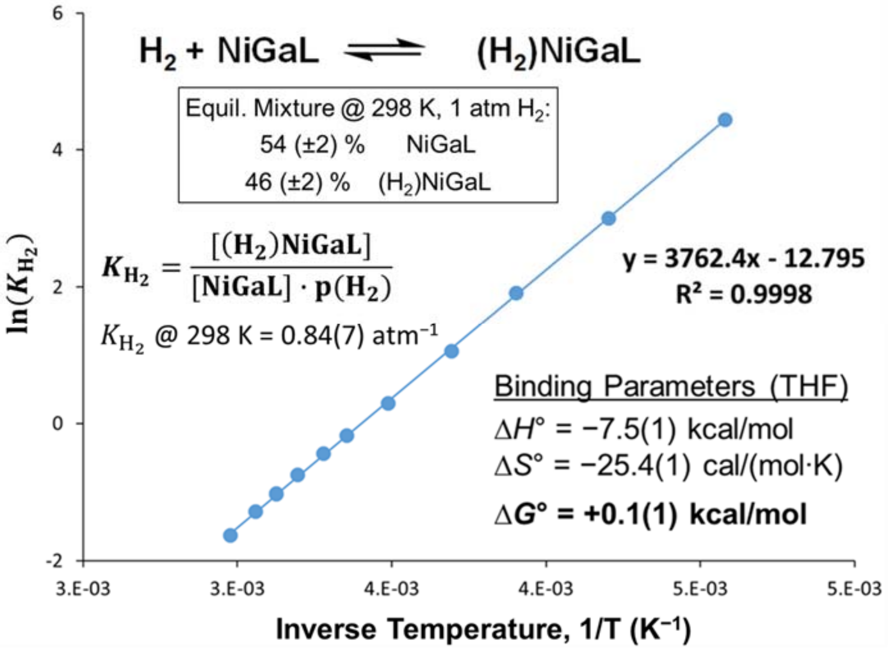

Figure S29. van't Hoff plot of $\ln(K_{H_2})$ vs. 1/T for H_2 binding equilibrium to NiGaL (**2**) in THF, based on VT ^{31}P NMR data collected under 3.8 atm H_2 from 218 to 336 K. The thermodynamic binding parameters and the associated uncertainties obtained from linear regression are also displayed above (standard conditions: 298 K, 1 atm H_2, 1 M of all other species, THF). The free energy of H_2 binding to **2** ($\Delta G°$) was found to be slightly more favorable in THF than in toluene (by ~0.5 kcal/mol), albeit nearly within experimental error. This minor solvent effect was reproduced by DFT calculated binding energies (Table S16) and has literature precedent.[34,35]

VT NMR Experiments for N_2 Binding

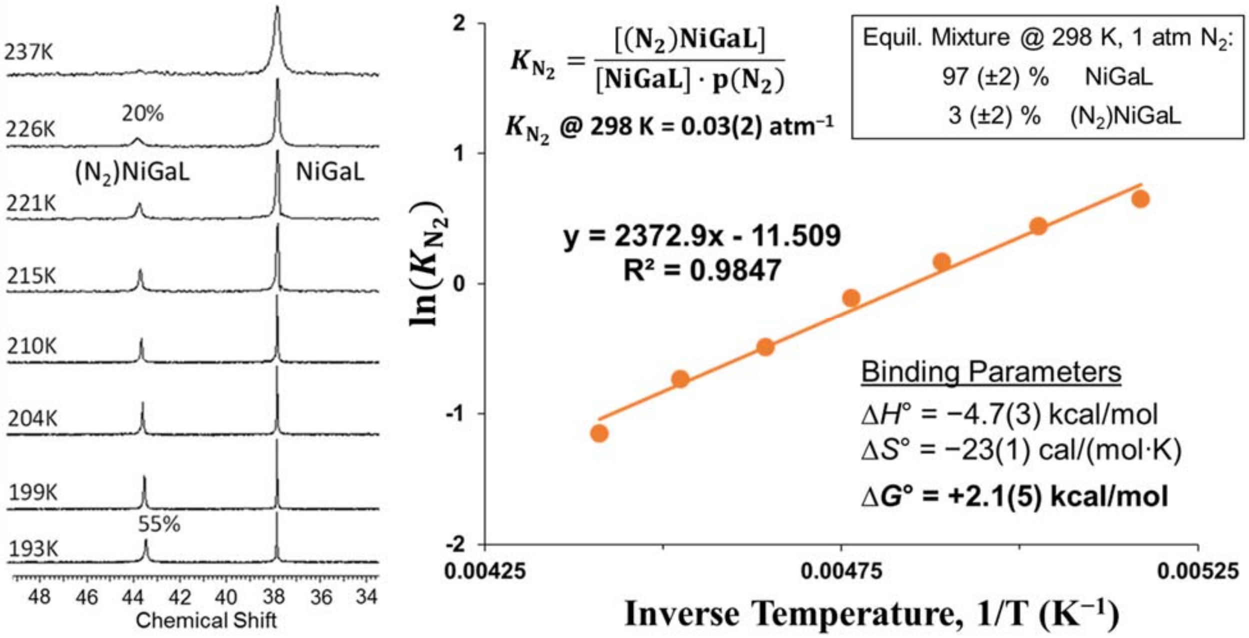

Figure S30. Stacked VT ^{31}P NMR spectra (161.9 MHz) of NiGaL (**2**) in toluene (~15 mM in 0.41 mL) under 1 atm N_2 (left) and the resulting van't Hoff plot from evaluating K_{N_2} at various T from 226 to 193 K (right). The thermodynamic binding parameters and the associated uncertainties obtained from linear regression are also displayed above (standard conditions: 298 K, 1 atm N_2, 1 M of all other species in toluene). The concentration of (N_2)NiGaL (**2**−N_2; ~43.5 ppm) increases compared to that of **2** (~37.8 ppm) as T decreases from 226 K to 193 K.

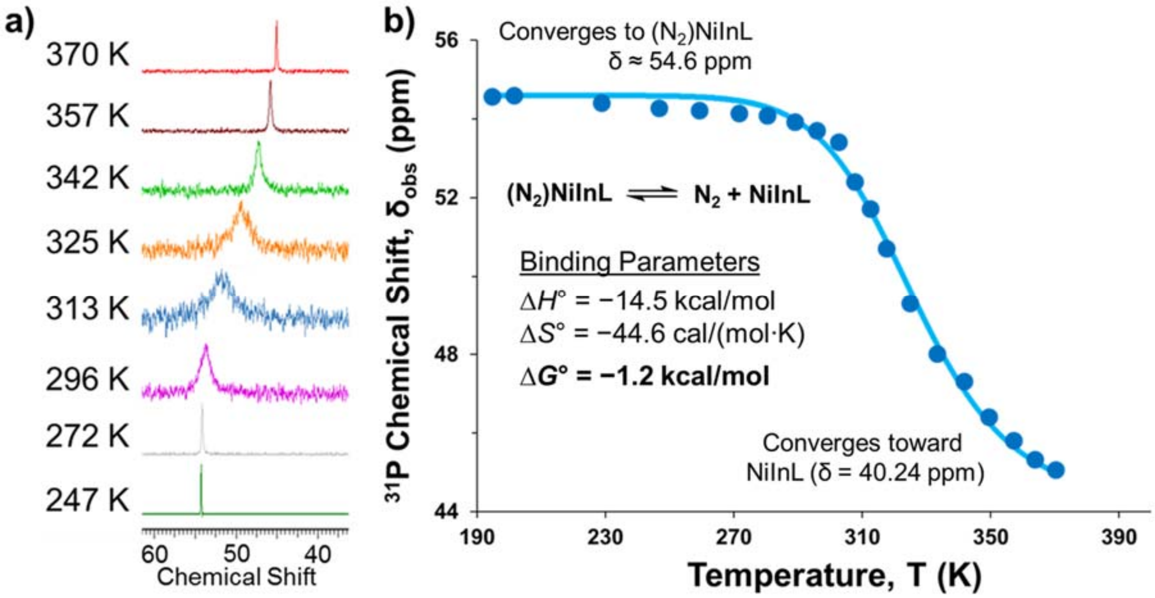

Figure S31. (a) Stacked VT ^{31}P NMR spectra (161.9 MHz) of NiInL (**3**) under 1 atm N_2 in toluene-d$_8$ (~11 mM in 0.55 mL) from 370 to 247 K. A single ^{31}P resonance is observed at all T, with chemical shift (δ) approximately equal to the population-weighted average of δ for **3** (44.24 ppm) and (N_2)NiInL (**3**−N_2; 54.6 ppm). The peak begins to broaden from 296 K to 342 K, but van't Hoff analysis in different T regimes supports the notion that fast chemical exchange is a reasonable assumption (Figure S6). (b) Plot of ^{31}P δ vs. T, with data shown as blue circles and the solid blue trace representing the best non-linear fit (best-fit parameters shown above).

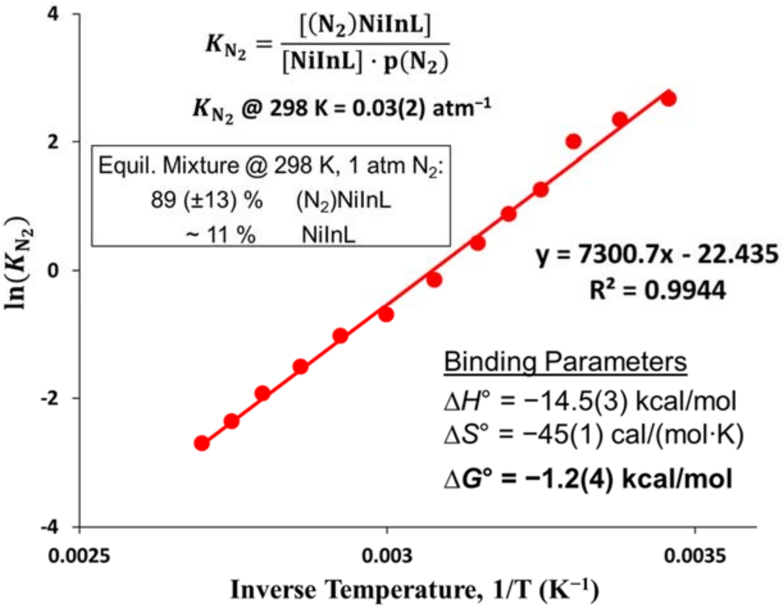

Figure S32. van't Hoff plot of $\ln(K_{N_2})$ vs. 1/T for N_2 binding equilibrium to NiInL (**3**), based on VT ^{31}P NMR data collected under 1.0 atm N_2 from 288 to 370 K. Thermodynamic binding parameters and their associated uncertainties obtained from linear regression are also displayed above (standard conditions: 298 K, 1 atm N_2, 1 M of all other species, toluene-d$_8$).

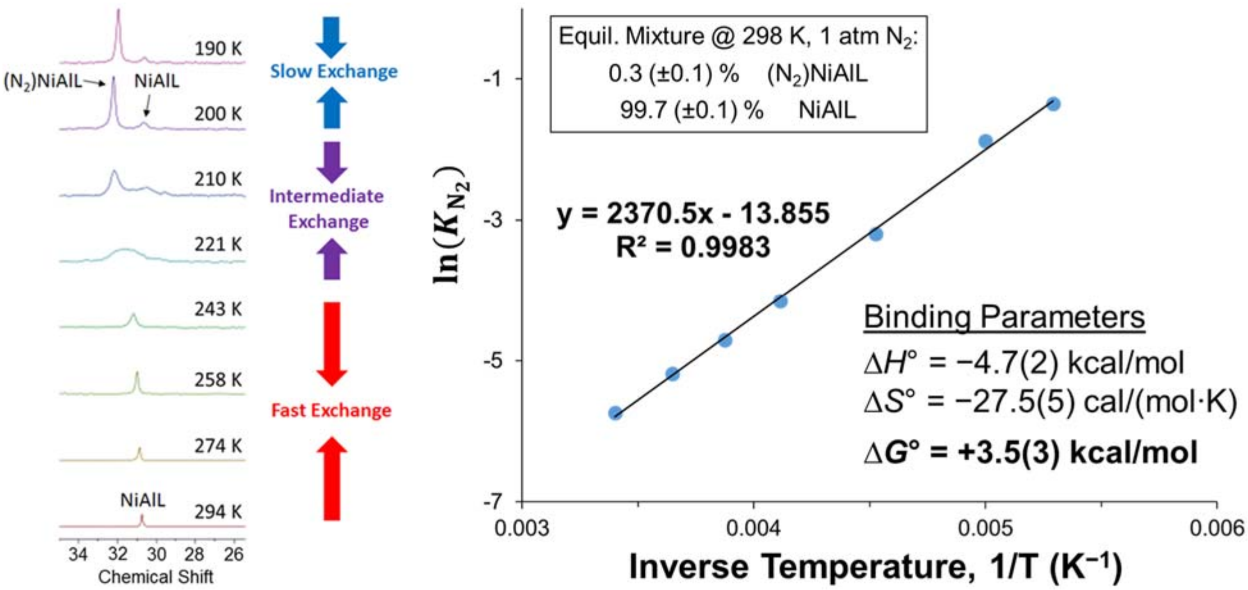

Figure S33. Stacked VT ^{31}P NMR spectra (202.4 MHz) of NiAlL (**1**) in toluene-d_8 (~16 mM in 0.30 mL) under 51 atm N_2 (left), and the resulting van't Hoff plot from evaluating K_{N_2} at various T from 294 K to 190 K (right). A fast equilibrium relative to the ^{31}P NMR timescale is observable from 294 K to ~243 K. The ^{31}P peak broadens at 221 K, indicating an intermediate exchange regime, and two distinct peaks are observed below 210 K (slow exchange). All spectra shown were included in the van't Hoff analysis (right), except for that obtained at 210 K where the peaks for **1** and **1**−N_2 overlapped. The thermodynamic binding parameters and the associated uncertainties obtained from linear regression are also displayed above (standard conditions: 298 K, 1 atm N_2, 1 M of all other species, toluene-d_8). Under slow exchange conditions at 200 K and 190 K, the two distinct ^{31}P peaks were integrated to determine K_{N_2}, while the observed ^{31}P δ relative to ^{31}P δ for **1** and **1**−N_2 allowed for the determination of K_{N_2} at T ≥ 243 K. **1**−N_2 was taken to have ^{31}P δ ~ 32.2 ppm based on the convergence of δ at low T. The fact that δ for **1** at 190 K matches that obtained for **1** under Ar supports the notion that δ for **1**−N_2 has also converged at 190 K. It should be noted that the close proximity of δ for the bound (**1**−N_2, ~32.2 ppm) and unbound (**1**, 30.7 ppm) species likely results in a greater amount of error in both K_{N_2} and the determined binding parameters than that given by linear regression of the van't Hoff plot.

Comparison with Binding Parameters of Literature Complexes

Table S6. H_2 thermodynamic binding parameters (for 1 atm H_2 standard state) reported for literature complexes and **1-3**[a]

Complex	$\Delta H^{\circ}_{\mathrm{1atm}}$ (kcal/mol)	$\Delta S^{\circ}_{\mathrm{1atm}}$ (cal/mol•K)	$\Delta G^{\circ}_{\mathrm{1atm}}$ (kcal/mol)	$\Delta G^{\circ}_{\mathrm{1M}}$ (kcal/mol)
1 [c]	−6.3 (0.1)	−26.4 (0.4)	**+1.6 (0.2)**	−1.9 (0.2)
2 [c]	−6.0 (0.8)	−22 (2)	**+0.6 (0.2)**	−2.9 (0.2)
$\mathrm{Mo(CO)_3(PCy_3)_2}$ [d]	−6.5 (0.2)	−23.8 (2.1)	**+0.6 (0.1)**	−2.9 [b]
$\mathrm{Cr(CO)_3(PCy_3)_2}$ [d]	−7.3 (0.2)	−25.6 (1.7)	**+0.3 (0.1)**	−3.2 [b]
$\mathrm{[Fe(P_4N_2)]^+}$ [e]	−2.48 (0.07)	−8.5 (0.2)	**+0.05 (0.09)** [i]	−3.5 [b]
$\mathrm{W(CO)_3(PCy_3)_2}$ [d]	−10 (1) [f]	−29 (3) [g]	**−1.4**	−4.5 (0.1) [h]
3 [c]	−14.8 (0.6)	−37 (2)	**−3.7 (0.7)** [j]	−7.1 (0.7) [j]

[a] Standard state is defined as 1 atm H_2 and 1 M of all other species, at 298 K. Values were measured in either toluene (complexes **1**-**3**) or THF (all other complexes unless otherwise noted), with standard deviations given in parenthesis; it should be noted that similar binding energies were determined for **2** in both toluene and THF (see Figures S27-S29).
[b] Estimated value based on approximate conversion factor between 1 atm and 1 M standard states for H_2 in toluene.
[c] Measured via VT ^{31}P NMR spectroscopy in this work.
[d] Measured in THF via VT IR spectroscopy.[34,35] Similar ΔH° values were measured in both THF and toluene by calorimetry.
[e] Measured via VT UV-Vis spectroscopy in PhF.[36]
[f] Measured via calorimetry.
[g] Estimated value based on measured $\Delta H^{\circ}_{\mathrm{1atm}}$ and estimated $\Delta G^{\circ}_{\mathrm{1atm}}$ values.
[h] Measured via time-resolved step-scan FTIR and UV-Vis spectroscopies.
[i] Adjusted to 298 K based on ΔH° and ΔS° determined from 268 K to 288 K. $\Delta G^{\circ}_{\mathrm{1atm}}$ reported at 268 K to be −0.20(7) kcal/mol.[36]
[j] Estimated values extracted from fast-intermediate exchange regime ^{31}P NMR data. See main text for discussion: −3.0(7) and −6.5(7) kcal/mol are proposed to be better estimates for $\Delta G^{\circ}_{\mathrm{1atm}}$ and $\Delta G^{\circ}_{\mathrm{1M}}$, respectively.

Table S7. H_2 thermodynamic binding parameters (for 1 M H_2 standard state) reported in the literature compared with those for complexes **1-3**[a]

Complex	$\Delta H^{\circ}_{\mathrm{1M}}$ (kcal/mol)	$\Delta S^{\circ}_{\mathrm{1M}}$ (cal/mol•K)	$\Delta G^{\circ}_{\mathrm{1M}}$ (kcal/mol)	$\Delta G^{\circ}_{\mathrm{1atm}}$ (kcal/mol)
$\mathrm{RuH(Cl)(CO)(P^{\mathit{i}}Pr_3)_2}$ [c]	−7.7 (0.2)	−23.2 (1.0)	**−0.8 (0.1)**	+2.7 [b]
$\mathrm{Ir(H)_2(Cl)(P^{\mathit{t}}Bu_2Ph)_2}$ [c]	−6.8 (0.2)	−19.2 (0.7)	**−1.1 (0.1)**	+2.4 [b]
1 [d]	−7.7 (0.1)	−19.5 (0.4)	**−1.9 (0.2)**	+1.6 (0.2)
$\mathrm{Ir(H)_2(Br)(P^{\mathit{t}}Bu_2Ph)_2}$ [c]	−7.9 (0.9)	−19.7 (3.2)	**−2.0 (0.2)**	+1.5 [b]
$\mathrm{Ir(H)(Cl)_2(P^{\mathit{i}}Pr_3)_2}$ [c]	−7.1 (0.2)	−16 (1)	**−2.3 (0.4)**	+1.2 [b]
$\mathrm{Ir(H)_2(I)(P^{\mathit{t}}Bu_2Ph)_2}$ [c]	−9.3 (0.2)	−22.7 (0.8)	**−2.5 (0.1)**	+1.0 [b]
2 [d]	−7.4 (0.8)	−15 (2)	**−2.9 (0.2)**	+0.6 (0.2)
Co(TPB) [e]	−12.5 (0.3)	−26 (3)	**−4.8 (0.9)**	−1.3 [b]
$\mathrm{[Re(CNR)_3(PCy_3)_2]^+}$ [f]	−18.0 (0.7)	−44(2)	**−4.8 (1.3)**	−1.3 [b]
3 [d]	−16.2 (0.6)	−30 (2)	**−7.1 (0.7)** [g]	−3.7 (0.7) [g]

[a] Standard state is defined as 1 M for all species at 298 K. All values were determined in toluene unless otherwise noted, with standard deviations shown in parenthesis.
[b] Estimated value based on approximate conversion factor between 1 atm and 1 M standard states for H_2 in toluene.
[c] Measured by VT NMR spectroscopy.[37-41]
[d] Measured by VT ^{31}P NMR spectroscopy in this work. Values for **1**-**2** are based on the assumption that [H_2] in toluene is proportional to pressure at high pressures.
[e] Measured by VT UV-Vis spectroscopy.[9,42]
[f] Measured in $CDCl_2$ via VT NMR spectroscopy for R=^{t}Bu.[42]
[g] Estimated values extracted from fast-intermediate exchange regime VT ^{31}P NMR data. See main text for discussion: −6.5(7) and −3.0(7) kcal/mol are proposed to be better estimates for $\Delta G^{\circ}_{\mathrm{1M}}$ and $\Delta G^{\circ}_{\mathrm{1atm}}$, respectively.

Table S8. N_2 thermodynamic binding parameters (for 1 atm N_2 standard state) reported for literature complexes and **1-3**[a]

Complex	ΔH°_{1atm} (kcal/mol)	ΔS°_{1atm} (cal/mol•K)	**ΔG°_{1atm} (kcal/mol)**	ΔG°_{1M} (kcal/mol)
1 [c]	−4.7 (0.2)	−27.5 (0.5)	**+3.5 (0.3)**	+0.4 (0.1)
2 [c]	−4.7 (0.3)	−23 (1)	**+2.1 (0.5)**	−1.0 (0.5)
$Cr(CO)_3(PCy_3)_2$ [d]	−9.3 (0.2)	−35.4 (2.3)	**+1.3 (0.7)**	−1.8 [b]
$Mo(CO)_3(PCy_3)_2$ [d]	−9.0 (0.6)	−32.1 (3.2)	**+0.6 (0.1)**	−2.5 [b]
$[Fe(P_4N_2)]^+$ [f]	−6.6 (0.1)	−23.4 (0.4)	**+0.41 (0.05)**	−2.7 [b]
$W(CO)_3(PCy_3)_2$ [d]	−13.5 (1.0) [e]	–	**–**	–
3 [c]	−14.5 (0.3)	−45 (1)	**−1.2 (0.4)**	−4.3 (0.4)
$Fe(P_4N_2)$	–	–	**−7.0** [g]	−10.1 [b]

[a] Standard state is defined as 1 atm N_2 and 1 M of all other species, at 298 K. Standard deviations are given in parenthesis for each value. [b] Estimated value based on approximate conversion factor between 1 atm and 1 M standard states for N_2 (for toluene). [c] Measured in toluene via VT ^{31}P NMR spectroscopy in this work. [d] Measured in THF via VT IR spectroscopy.[34] Similar ΔH° values were measured in both THF and toluene by calorimetry. [e] Measured via calorimetry.[35] [f] Measured in fluorobenzene by VT UV-Vis spectroscopy.[43] [g] Measured in fluorobenzene by using CV data and the known cation binding parameters to construct a thermochemical cycle. ΔG°_{1atm} for N_2 binding to the analogous Fe(II) dicationic species was estimated to be > +30 kcal/mol.

Table S9. Compilation of N_2 thermodynamic binding parameters (for 1 M N_2 standard state) reported in the literature compared with those for complexes **1-3**[a]

Complex	ΔH°_{1M} (kcal/mol)	ΔS°_{1M} (cal/mol•K)	**ΔG°_{1M} (kcal/mol)**	ΔG°_{1atm} (kcal/mol)
1 [c]	−5.4 (0.1)	−19.5 (0.4)	**+0.4 (0.1)**	+3.5 (0.3)
$[(N_2)Fe_2(\mu\text{-}H)_2(SiP_2O)]$ [d]	−9.0 (0.4)	−30 (2)	**−0.1 (0.1)**	+3.0 [b]
2 [c]	−5.5 (0.3)	−14.9 (1.3)	**−1.0 (0.5)**	+2.1 (0.5)
3 [c]	−15.2 (0.3)	−36.6 (1.0)	**−4.3 (0.4)**	−1.2 (0.4)
Co(TPB) [e]	−13.9 (0.7)	−32 (5)	**−4.4 (1.6)**	−1.3 [b]
$[(N_2)Fe_2(\mu\text{-}H)_2(SiP_2O)]^-$ [f]	−18 [g]	−30 [g]	**−8.8**	−5.7 [b]

[a] Standard state is defined as 1 M N_2 and 1 M of all other species, at 298 K. Standard deviations are given in parenthesis for each value. [b] Estimated value based on approximate conversion factor between 1 atm and 1 M standard states for N_2 (for toluene). [c] Measured in toluene via VT ^{31}P NMR spectroscopy in this work. Value for **1** requires the assumption that $[N_2]$ in toluene is proportional to pressure even at high pressures. [d] Measured in hexanes via VT UV-Vis spectroscopy.[44] [e] Measured in toluene by VT UV-Vis spectroscopy.[9] [f] Measured in THF via CV simulation.[44] [g] Estimated based on assumption of similar ΔS° to that determined for analogous neutral species (see "d").

Profiles for H_2 and N_2 Binding to NiML Complexes (at Constant T and Variable P)

Table S10. Percentages (%) of (L')NiML and NiML at equilibrium at 298K and 1 atm L', as determined from Δ*G*° values[a]

Complex	% of Each Species Present at Equilibrium (1 atm, 298 K)			
	(η^2-H_2)NiML	NiML	(N_2)NiML	NiML
1	7(2)	93	0.3(1)	99.7
2	55(16)	45	3(2)	97
3	99(1)	1	90(10)	10

[a] Standard deviations in % (L')NiML species are given in parenthesis and are based on propagation of the standard deviation in the Δ*G*° values. The % bound and unbound species necessarily sum to 100%.

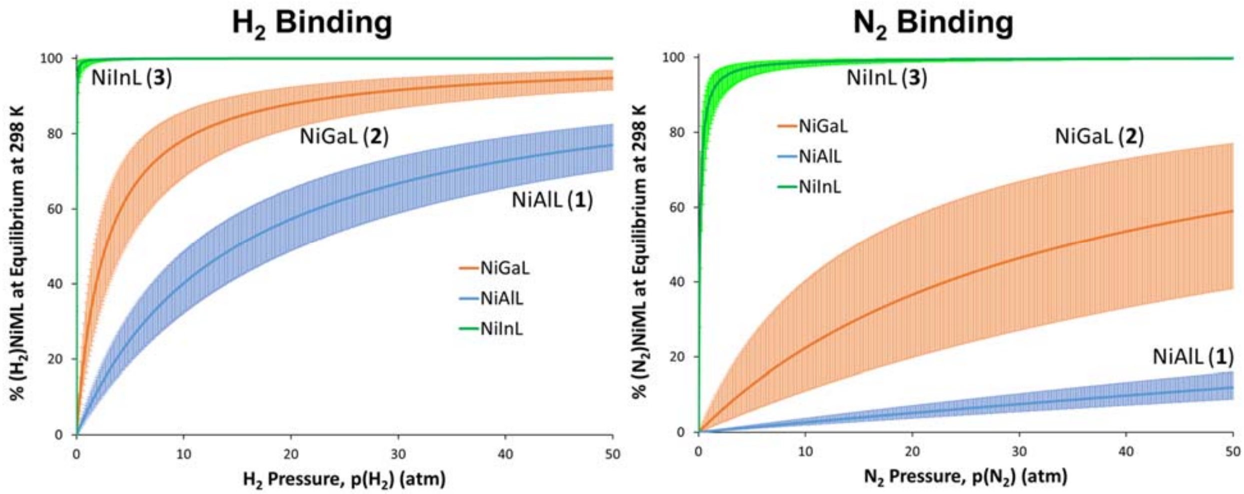
H_2 Binding

N_2 Binding

Figure S34. Plots of % (L')NiML at equilibrium at 298 K in toluene vs. L' gas pressure (L'= H_2 on left, and N_2 on right). The binding curves were calculated based on the experimental Δ*G*° values, and the shaded regions represent the range of uncertainty in % bound species that correspond to one standard deviation. The relative uncertainty in % (L')NiML is larger for small |Δ*G*°| values (i.e., close to 0 kcal/mol). For example, **2** has a small absolute error in its H_2 binding Δ*G*° value, 0.6 (± 0.2) kcal/mol, but because its Δ*G*° value is closer to 0 kcal/mol there is greater uncertainty in % **2**−H_2 at equilibrium. On the other hand, **3** has the largest absolute error in its estimated H_2 binding Δ*G*° value, −3.0(7) kcal/mol, but binding constants of −2.3 or −3.7 kcal/mol (adding or subtracting the standard deviation) would both lead to nearly full binding of H_2 to form **3**−H_2 at any substantial pressure, so the error bars are very small for % **3**−H_2. The relative trends in binding can be visualized nicely in these plots. N_2 binding is by far the most favorable for NiInL (**3**), with pressures as small as 1.2 atm N_2 resulting in >90% **3**−N_2 at equilibrium at 298 K. NiAlL (**1**) binds N_2 the weakest, requiring ~41 atm N_2 in order to reach >10% **1**−N_2 at equilibrium at 298 K. H_2 binds more favorably than N_2 in all cases, and H_2 pressures as small as 0.4 atm H_2 result in >98% **3**−H_2 at equilibrium at 298 K. In contrast, **1** binds H_2 the weakest, requiring ~45 atm H_2 to reach >75% **1**−H_2 at equilibrium at 298 K. Complex **2** binds H_2 moderately relative to the other NiML complexes, only requiring ~8 atm H_2 to reach >75% **2**−H_2 at 298 K.

IV. Data for Kinetics Studies: Rates of H_2 Self-Exchange and H_2 Loss via VT ^{31}P NMR Lineshape Analysis

VT ^{31}P and ^{1}H NMR Spectra

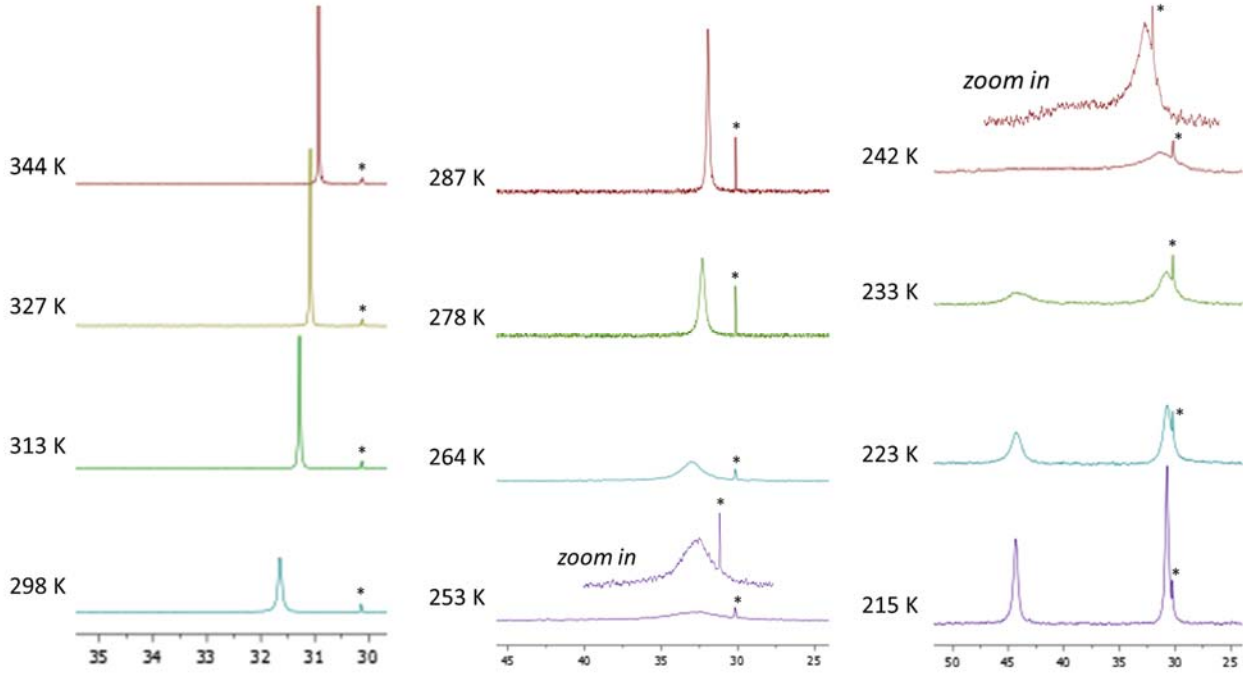

Figure S35. Stacked VT ^{31}P NMR spectra (161.9 MHz) of NiAlL (**1**) in toluene-d_8 (~7.5 mM in 0.70 mL) under 1 atm H_2 from 344 to 215 K. A small peak at 30.15 ppm for $NiLH_3$, which is generated from trace H_2O, is denoted with an asterisk (*). The $NiLH_3$ peak was used as an internal reference standard for chemical shift. The lineshape of the lone ^{31}P resonance shifts with minimal broadening from 344 K to 313 K (i.e., fast chemical exchange), begins to broaden as it shifts from 298 K to 253 K (intermediate exchange), and de-coalesces into two distinct peaks at $T < 242$ K (slow exchange). These VT NMR spectra were used to extract self-exchange rates for the interconversion between **1** and (η^2-H_2)NiAlL (**1**−H_2) via lineshape analysis (Figure S42).

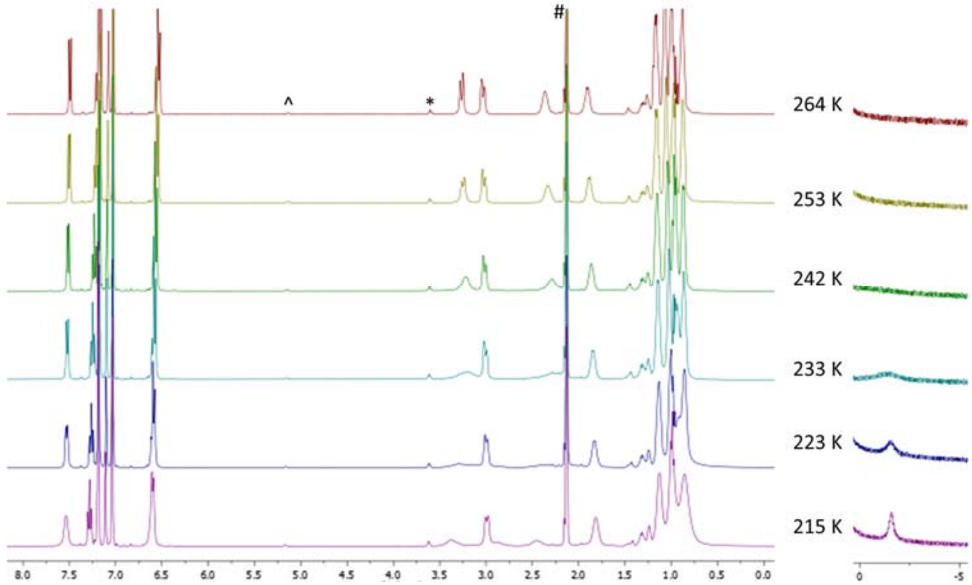

Figure S36. Stacked VT ^{1}H NMR spectra (400 MHz) of NiAlL (**1**) in toluene-d_8 (~7.5 mM in 0.70 mL) under 1 atm H_2 at low T (215 to 264 K). Residual solvent peaks for toluene (#) and THF (*) are denoted, along with the N*H* peak (^) of the $NiLH_3$ impurity, which forms from trace H_2O. A peak for Ni-bound H_2 is observable at ~ −1.6 ppm, which sharpens upon cooling to 215 K. No peak for free H_2 was observed.

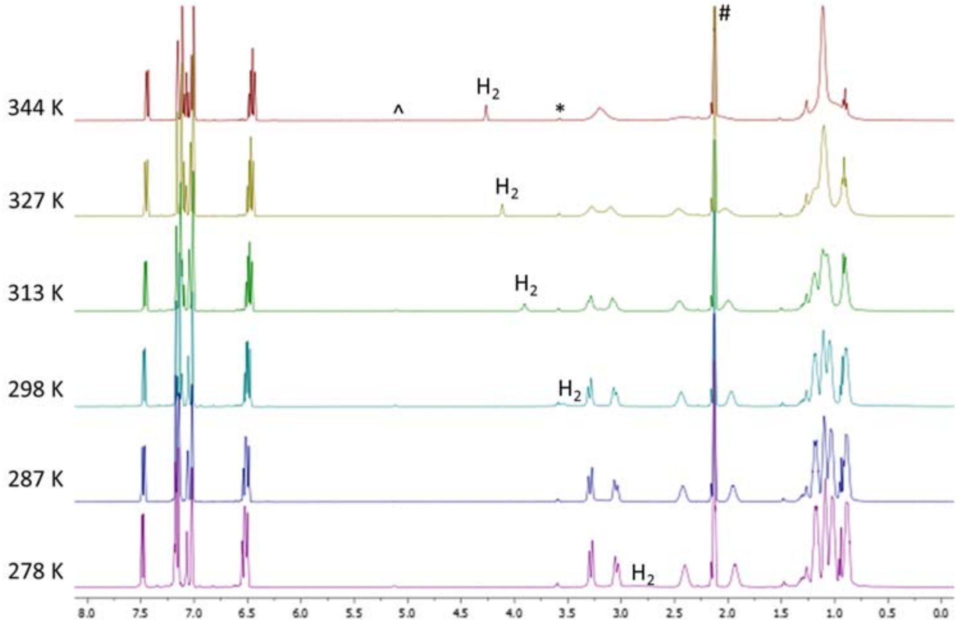

Figure S37. Stacked VT ^{1}H NMR spectra (400 MHz) of NiAlL (**1**) in toluene-d_8 (~7.5 mM in 0.70 mL) under 1 atm H_2 at high T (278 to 344 K). Residual solvent peaks for toluene (#) and THF (*) are denoted, along with the N*H* peak (^) of the $NiLH_3$ impurity, which forms from trace H_2O. A peak for "free" H_2 is observable, with its chemical shift changing from 4.27 ppm at 344 K to 2.86 ppm at 278 K. The NMR dynamics are consistent with a rapid binding equilibrium between free H_2 (4.57 ppm) and Ni-bound H_2 (−1.6 ppm), where free H_2 at is favored at high T (under 1 atm H_2).

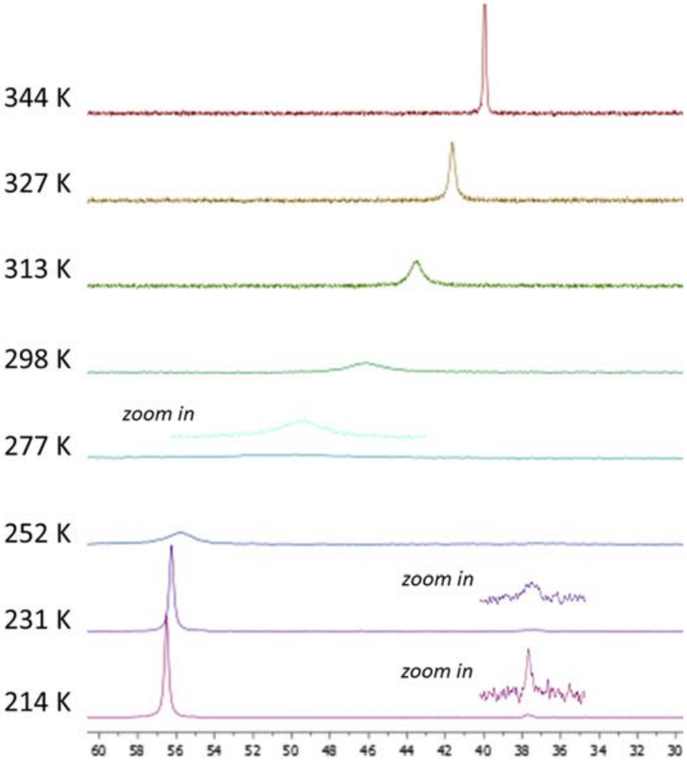

Figure S38. Stacked VT ^{31}P NMR spectra (161.9 MHz) of NiGaL (**2**) in toluene-d$_8$ (~7.5 mM in 0.70 mL) under 1 atm H_2 from 344 to 277 K, which were used to extract self-exchange rates for the interconversion between **2** and (η^2-H_2)NiGaL (**2**−H_2) via lineshape analysis (Figure S43).

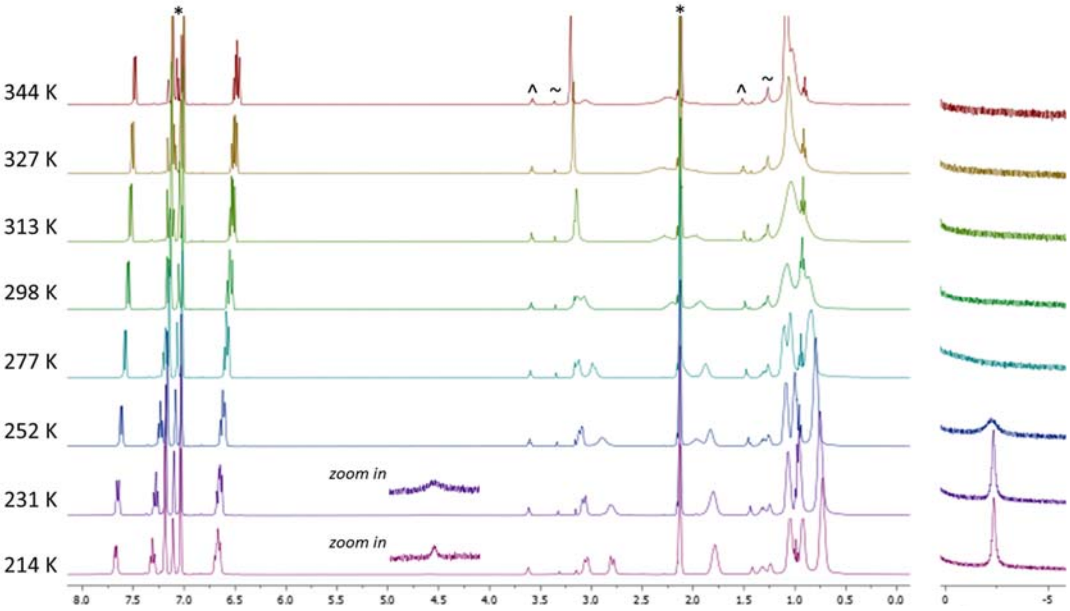

Figure S39. Stacked VT ^{1}H NMR spectra (400 MHz) of NiGaL (**2**) in toluene-d$_8$ (~7.5 mM in 0.70 mL) under 1 atm H_2. Residual solvent peaks for toluene (*), THF (^), and diethyl ether (~) are denoted. Both free H_2 and bound H_2 are observable at T < 240 K, indicating that the binding equilibrium between free H_2 and Ni-bound H_2 becomes slow at low T. The diastereotopic CH_2 protons of the ligand arm (~3.14 ppm) become equivalent at T > 300 K.

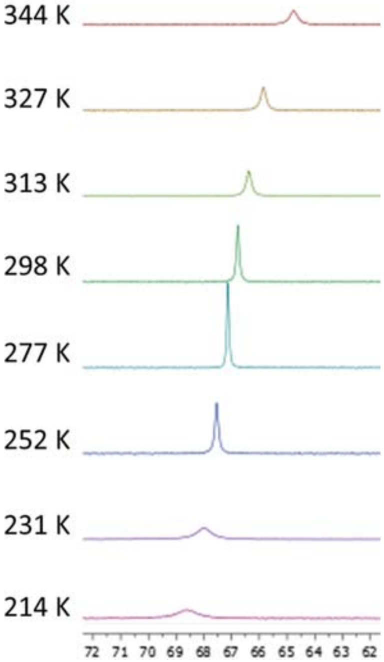

Figure S40. Stacked VT ^{31}P NMR spectra (161.9 MHz) of NiInL (**3**) in toluene-d$_8$ (~7.5 mM in 0.70 mL) under 1 atm H_2 from 344 to 214 K, which were used to extract self-exchange rates for the interconversion between **3** and (η^2-H_2)NiInL (**3**−H_2) via lineshape analysis (Figure S44).

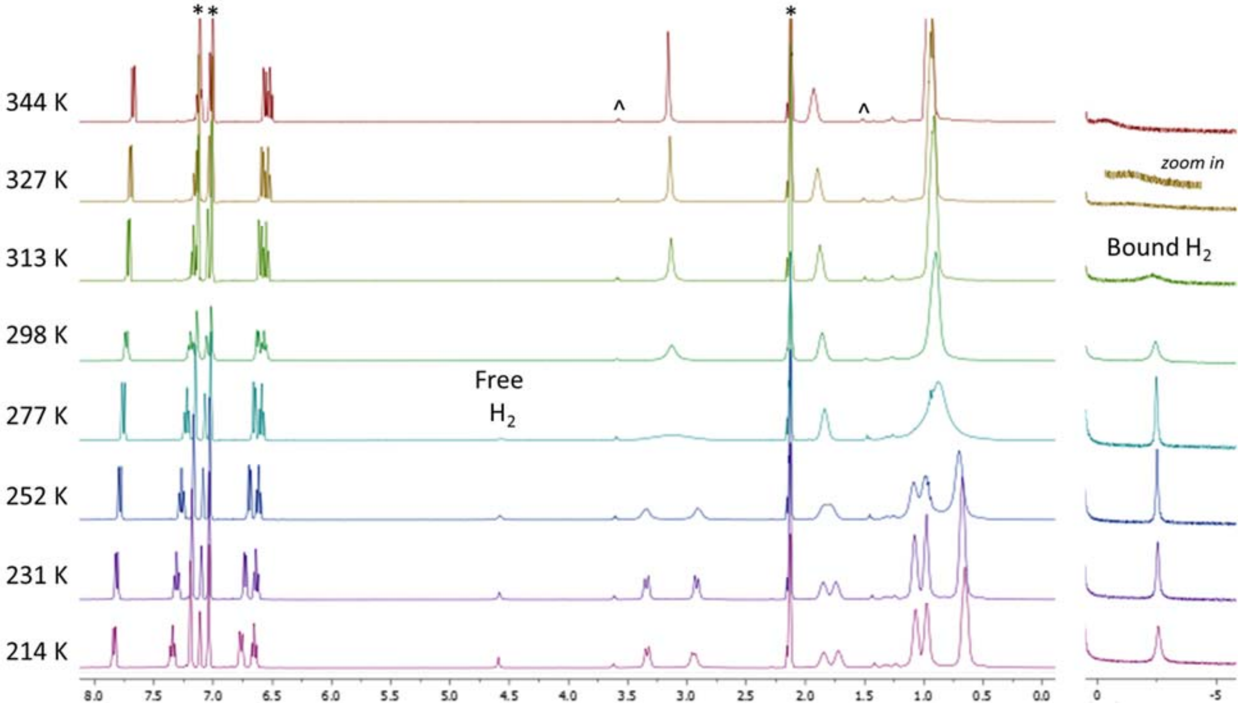

Figure S41. Stacked VT ^{1}H NMR spectra (400 MHz) of NiInL (**3**) in toluene-d$_8$ (~7.5 mM in 0.70 mL) under 1 atm H_2 from 344 to 214 K. Residual solvent peaks for toluene (*) and THF (#) are denoted. Peaks for both free H_2 and bound H_2 are observable at T < 300 K, indicating that interconversion between free H_2 and Ni-bound H_2 slows at low T. The diastereotopic C*H₂* protons of the ligand arm (~3.14 ppm) become equivalent at T > 277 K.

Lineshape Analysis of VT ^{31}P NMR Spectra

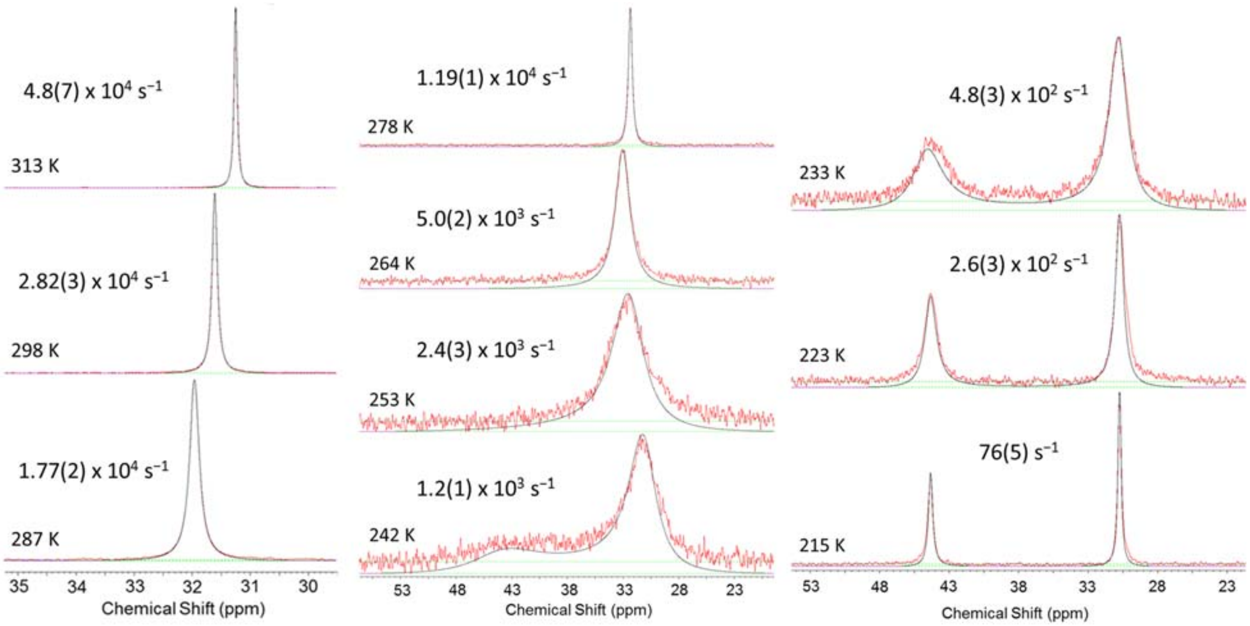

Figure S42. Comparison of VT ^{31}P NMR data (red traces, 161.9 MHz) and best-fit lineshape simulations (black traces) for NiAlL (**1**) in toluene-d_8 (~7.5 mM in 0.70 mL) under 1 atm H_2 from 215 to 313 K. The exchange rates at each T and the associated uncertainties are shown. Due to large uncertainties in exchange rates at high T, only data at T < 323 K were considered in Eyring analysis (see Figure 3b).

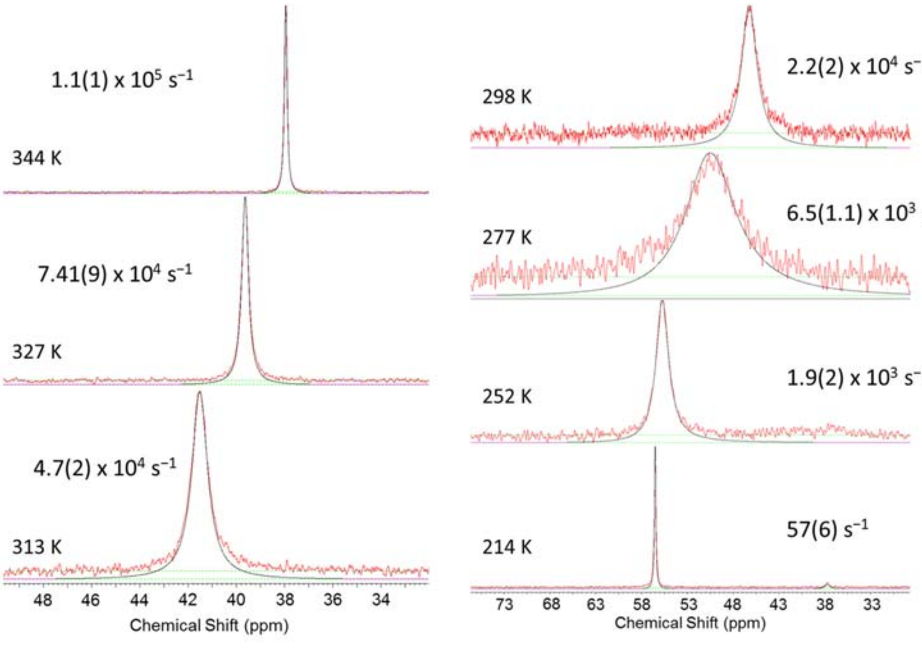

Figure S43. Comparison of VT ^{31}P NMR data (red traces, 161.9 MHz) and best-fit lineshape simulations (black traces) for NiGaL (**2**) in toluene-d_8 (~7.5 mM in 0.70 mL) under 1 atm H_2 from 214 to 344 K. The exchange rates at each T and the associated uncertainties are shown, which were used to determine the activation parameters for H_2 loss (refer to Eyring plot in Figure S49).

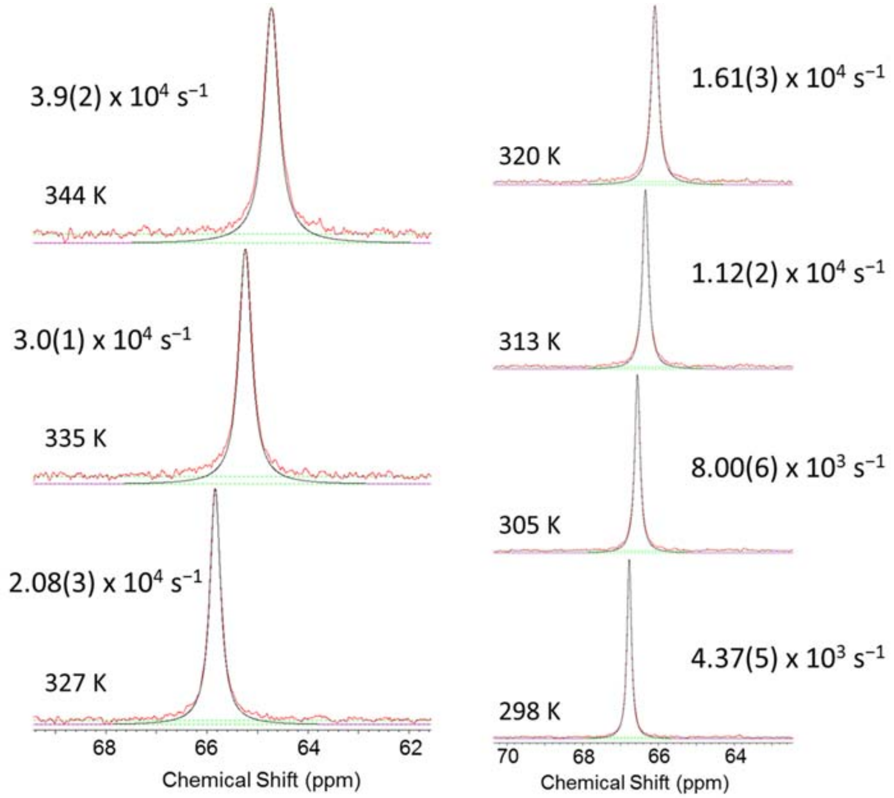

Figure S44. Comparison of VT ^{31}P NMR data (red traces, 161.9 MHz) and best-fit lineshape simulations (black traces) for NiInL (**3**) in toluene-d_8 (~7.5 mM in 0.70 mL) under 1 atm H_2 from 298 to 344 K. The exchange rates at each T and the associated uncertainties are shown, which were used to determine the activation parameters for H_2 loss (refer to Eyring plot in Figure S50). Data below T < 298 K were not analyzed due to the unreliability in determining exchange rates when the binding equilibrium lies nearly completely towards bound H_2 (> 98% **3**−H_2).

Table S11. Final parameters for ^{31}P NMR total lineshape simulations for NiAlL (**1**, top), NiGaL (**2**, middle), and NiInL (**3**, bottom) under 1 atm H_2 in toluene-d_8. Input parameters included chemical shifts (δ), intrinsic linewidths (W), and relative concentrations ([C]), as described in methods section C. In a few isolated instances indicated by an asterisk (*), slight alterations to the values for either δ or [C] of the bound species were used to obtain better fits for low T spectra; in these instances, the extracted exchange rates should be considered estimates.

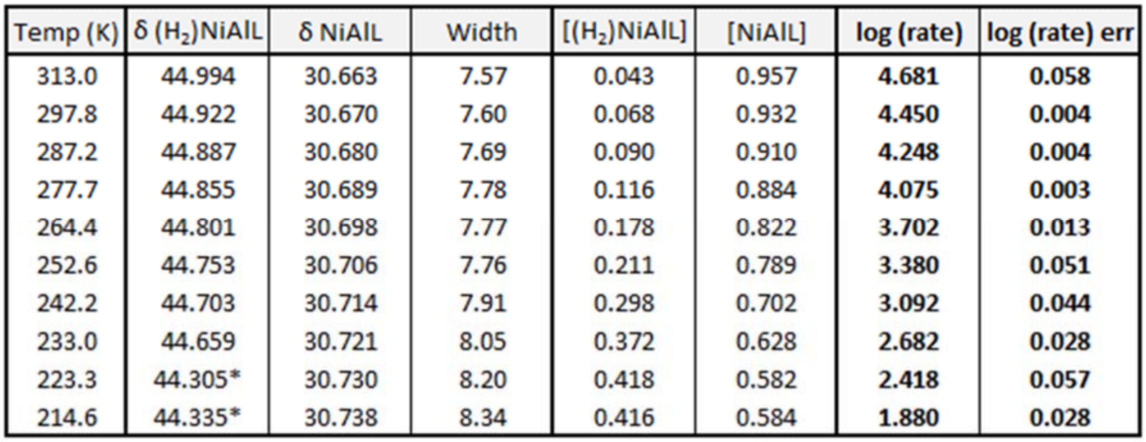

Temp (K)	δ (H_2)NiAlL	δ NiAlL	Width	[(H_2)NiAlL]	[NiAlL]	**log (rate)**	**log (rate) err**
313.0	44.994	30.663	7.57	0.043	0.957	**4.681**	**0.058**
297.8	44.922	30.670	7.60	0.068	0.932	**4.450**	**0.004**
287.2	44.887	30.680	7.69	0.090	0.910	**4.248**	**0.004**
277.7	44.855	30.689	7.78	0.116	0.884	**4.075**	**0.003**
264.4	44.801	30.698	7.77	0.178	0.822	**3.702**	**0.013**
252.6	44.753	30.706	7.76	0.211	0.789	**3.380**	**0.051**
242.2	44.703	30.714	7.91	0.298	0.702	**3.092**	**0.044**
233.0	44.659	30.721	8.05	0.372	0.628	**2.682**	**0.028**
223.3	44.305*	30.730	8.20	0.418	0.582	**2.418**	**0.057**
214.6	44.335*	30.738	8.34	0.416	0.584	**1.880**	**0.028**

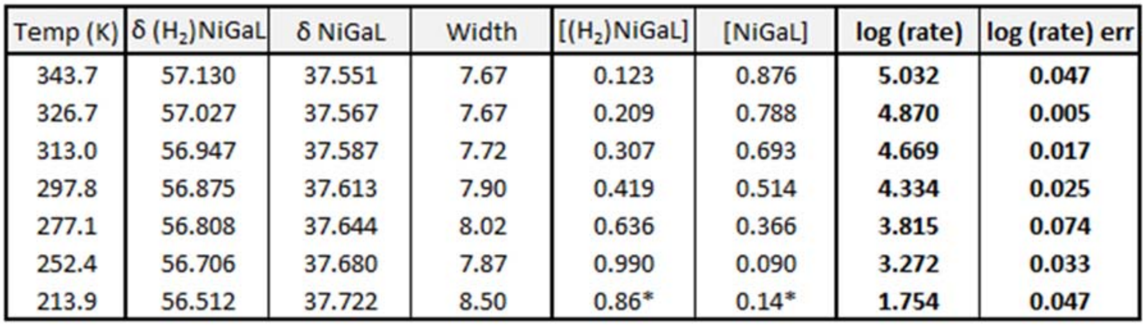

Temp (K)	δ (H_2)NiGaL	δ NiGaL	Width	[(H_2)NiGaL]	[NiGaL]	**log (rate)**	**log (rate) err**
343.7	57.130	37.551	7.67	0.123	0.876	**5.032**	**0.047**
326.7	57.027	37.567	7.67	0.209	0.788	**4.870**	**0.005**
313.0	56.947	37.587	7.72	0.307	0.693	**4.669**	**0.017**
297.8	56.875	37.613	7.90	0.419	0.514	**4.334**	**0.025**
277.1	56.808	37.644	8.02	0.636	0.366	**3.815**	**0.074**
252.4	56.706	37.680	7.87	0.990	0.090	**3.272**	**0.033**
213.9	56.512	37.722	8.50	0.86*	0.14*	**1.754**	**0.047**

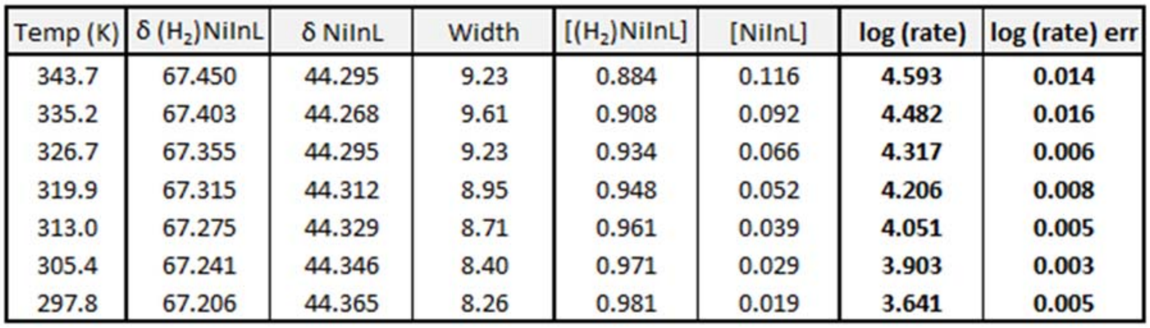

Temp (K)	δ (H_2)NiInL	δ NiInL	Width	[(H_2)NiInL]	[NiInL]	**log (rate)**	**log (rate) err**
343.7	67.450	44.295	9.23	0.884	0.116	**4.593**	**0.014**
335.2	67.403	44.268	9.61	0.908	0.092	**4.482**	**0.016**
326.7	67.355	44.295	9.23	0.934	0.066	**4.317**	**0.006**
319.9	67.315	44.312	8.95	0.948	0.052	**4.206**	**0.008**
313.0	67.275	44.329	8.71	0.961	0.039	**4.051**	**0.005**
305.4	67.241	44.346	8.40	0.971	0.029	**3.903**	**0.003**
297.8	67.206	44.365	8.26	0.981	0.019	**3.641**	**0.005**

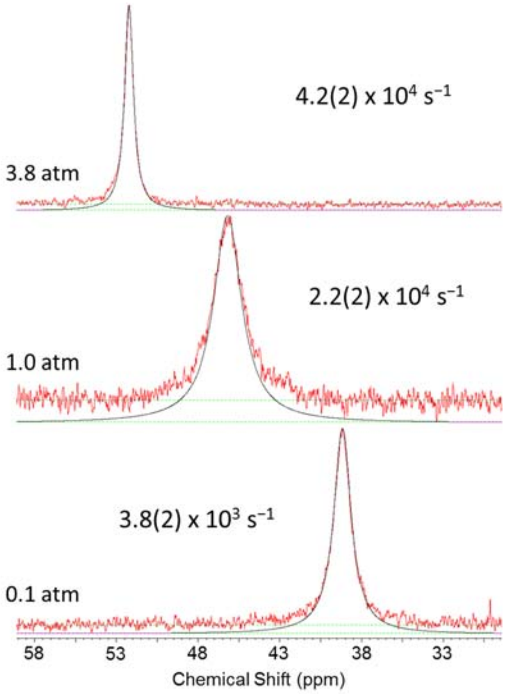

Figure S45. Comparison of experimental VT ^{31}P NMR data (red, 161.9 MHz) and best fit lineshape simulations (black traces) for NiGaL (**2**) in toluene-d$_8$ (~7.5 mM in 0.70 mL) under various pressures of H_2 (0.1, 1.0, and 3.8 atm) at 298(±1) K.

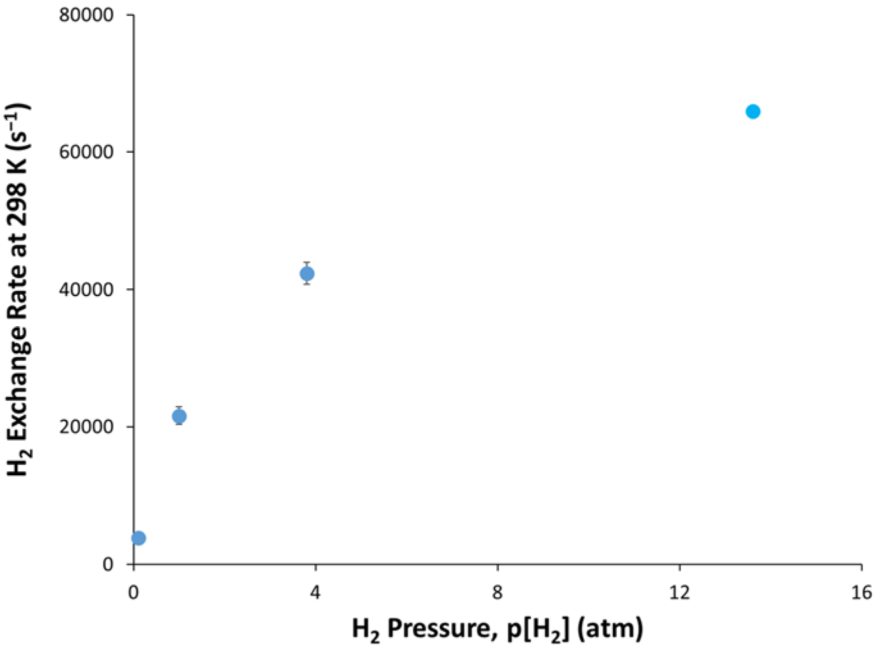

Figure S46. Plot of H_2 chemical exchange rate vs. H_2 gas pressure, for the interconversion between **2** and **2**−H_2 (self-exchange) in toluene-d$_8$ at 298 K ([Ni] ~ 7.5 mM). As the H_2 pressure increases, the exchange rate increases (see exchange rate determinations in the above figure). At 13.6 atm H_2, the exchange rate was estimated to be ~6.6 x 10^4 s^{-1}; however, this value has large uncertainty of >1.0 x 10^4 s^{-1}.

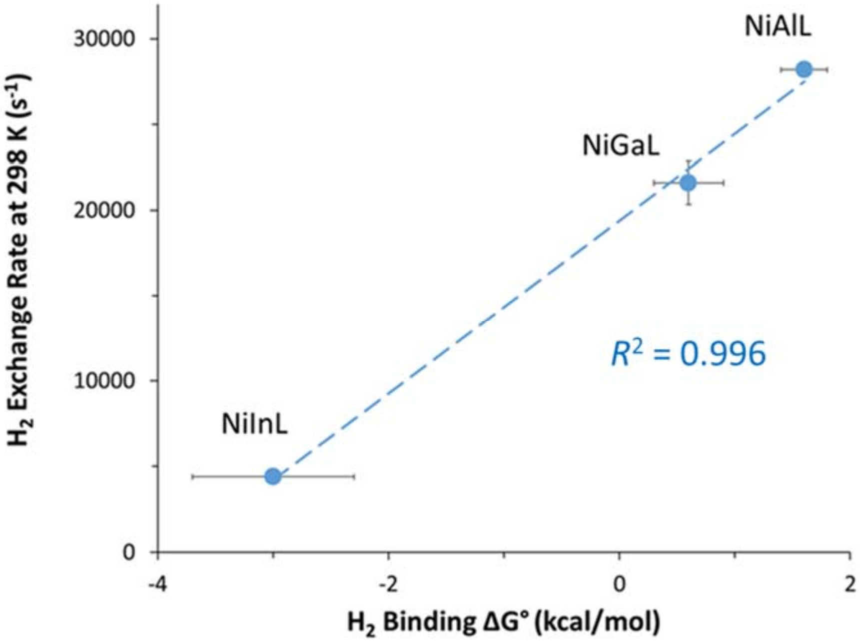

Figure S47. Plot of H_2 self-exchange rates at 298 K for interconversion between NiML and (η^2-H_2)NiML (in s^{-1}) vs. thermodynamic free energy for H_2 binding ($\Delta G°$ in kcal/mol), with the standard deviation in all values shown by error bars. A good correlation is observed (R^2=0.996), with more thermodynamically favorable H_2 binding manifesting in slower chemical exchange rates between free and bound H_2.

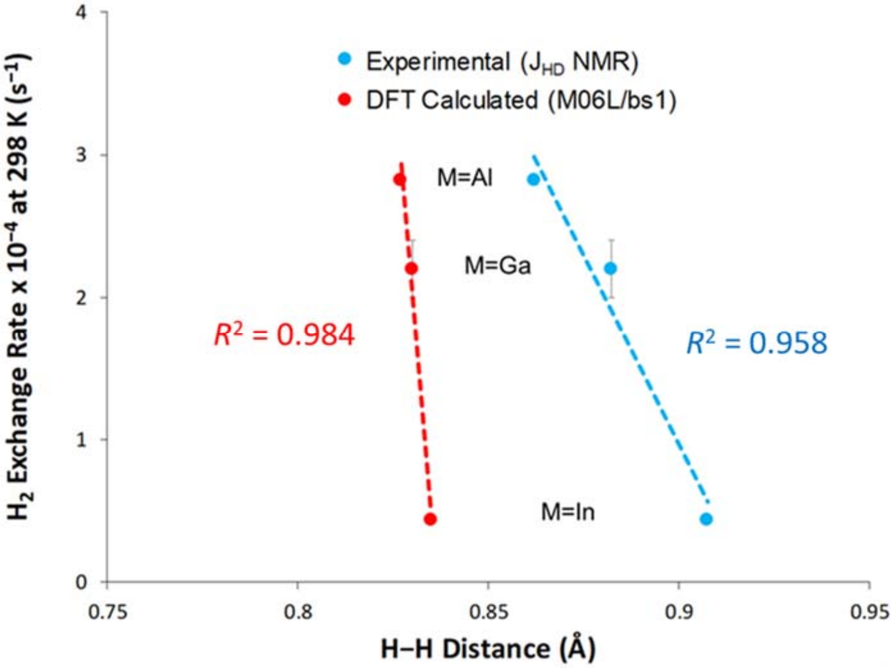

Figure S48. Plot of H_2 exchange rates at 298 K for NiML (in s^{-1}) vs. experimental (blue) and DFT calculated (red) H-H distances in (η^2-H_2)NiML, with the standard deviation in the exchange rates represented by error bars. Experimental distances are based on J_{HD} values determined at 213 K in toluene-d_8 (500 MHz, [NiML] = 7.5 mM under HD atm: 34.4, 33.2, and 31.7 Hz for **1**-HD, **2**-HD, and **3**-HD, respectively).[45] Good correlations are observed, with a shorter H−H distance that is closer to that of free H_2 manifesting in faster exchange rates between free and bound H_2.

Eyring Analyses for H_2 Loss Activation Parameters

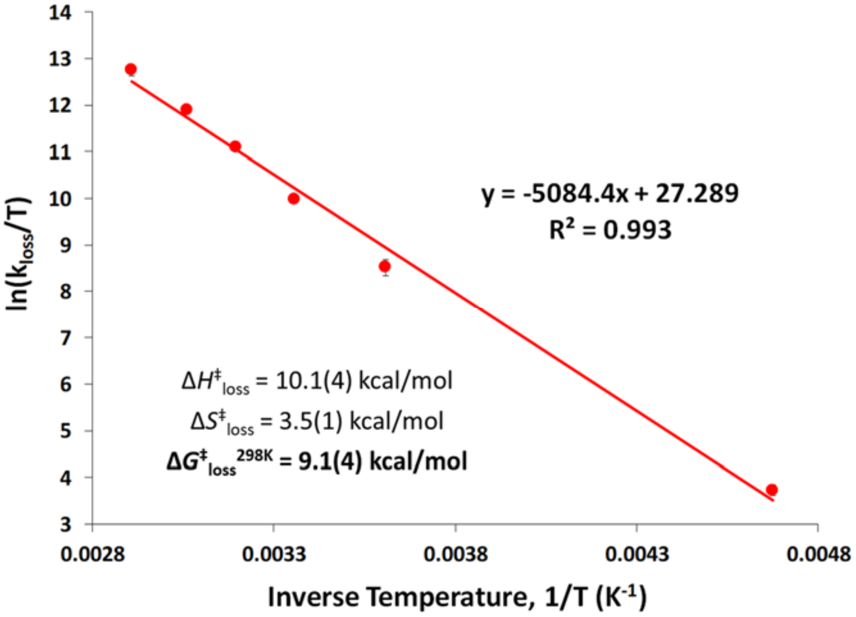

Figure S49. Eyring plot of ln(k_{loss}/T) vs. 1/T for H_2 loss from (η^2-H_2)NiGaL (**2**−H_2) to give NiGaL (**2**), where k_{loss} is the first-order rate constant for H_2 loss (in s^{-1}) extracted from VT ^{31}P NMR lineshape analysis (Figure S43). The activation parameters for H_2 loss ($\Delta H^{\ddagger}_{loss}$, $\Delta S^{\ddagger}_{loss}$, and $\Delta G^{\ddagger}_{loss}$) and the associated uncertainties obtained from linear regression are also shown, with the standard state defined as 1 M in toluene-d_8. Vertical error bars are difficult to see due to their small size.

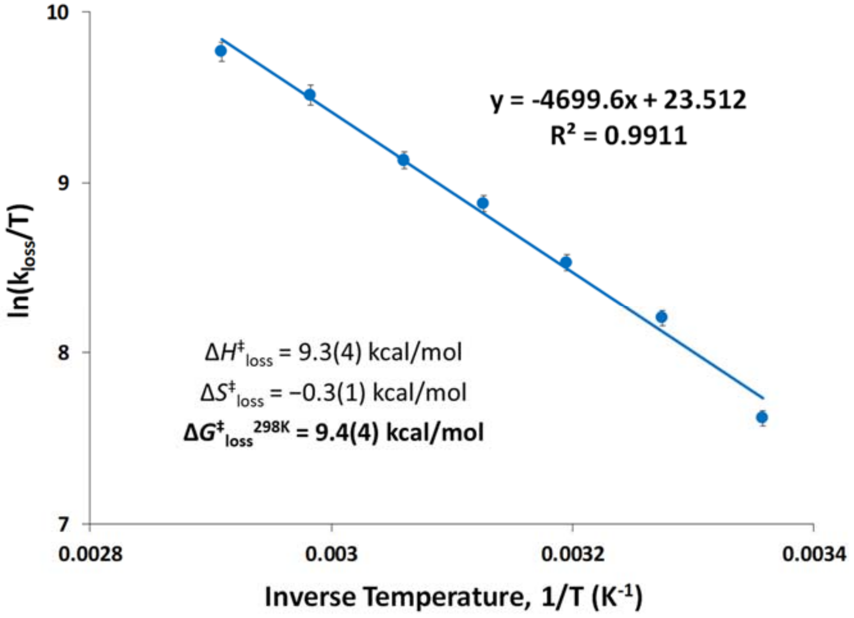

Figure S50. Eyring plot of ln(k_{loss}/T) vs. 1/T for H_2 loss from (η^2-H_2)NiInL (**3**−H_2) to give NiInL (**3**), where k_{loss} is the first-order rate constant for H_2 loss (in s^{-1}) extracted from VT ^{31}P NMR lineshape analysis (Figure S44). The activation parameters for H_2 loss ($\Delta H^{\ddagger}_{loss}$, $\Delta S^{\ddagger}_{loss}$, and $\Delta G^{\ddagger}_{loss}$) and the associated uncertainties obtained from linear regression are also shown, with the standard state defined as 1 M in toluene-d_8. Vertical error bars are difficult to see due to their small size.

Comparison of Kinetic and Thermodynamic Parameters for H_2 Binding to NiML Complexes

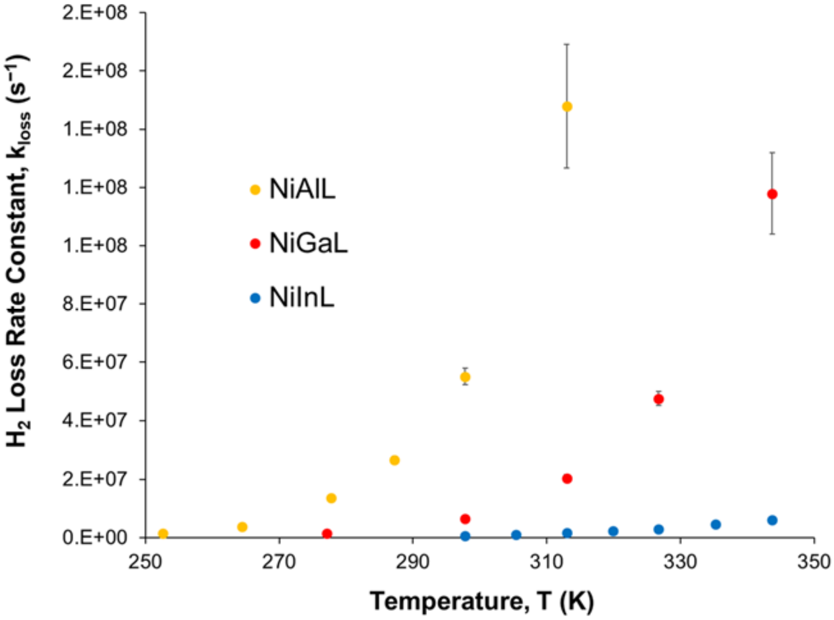

Figure S51. Comparison plot of H_2 loss rate constant (k_{loss} in s^{-1}) vs. T, with the standard deviation in all values shown by error bars. Smaller rate constants for H_2 loss (dissociation) are observed at a given T (In < Ga < Al) for more thermodynamically favorable H_2 binding equilibria.

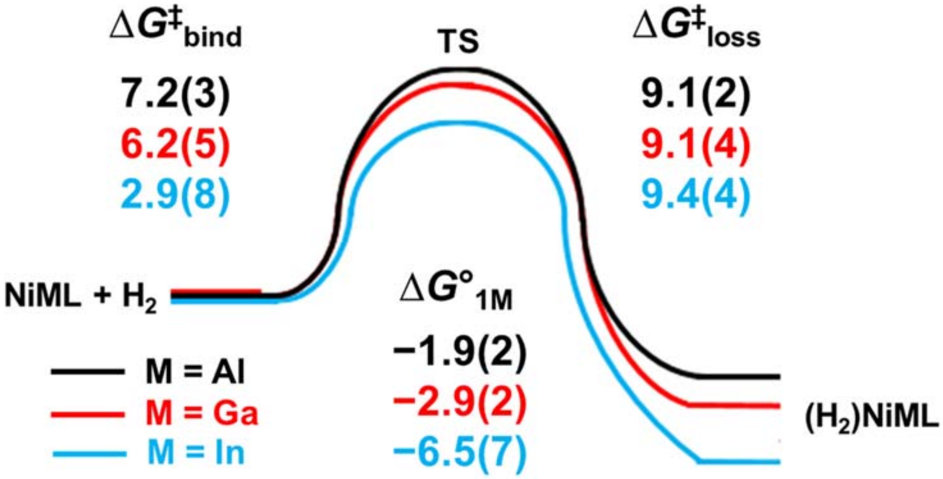

Figure S52. Reaction coordinate diagrams for H_2 binding to NiML, with all values given in kcal/mol. Note that although the diagram is not rigorously to scale, it correctly shows the relative trends in $\Delta G^{\ddagger}_{bind}$ and ΔG°_{1M} values for H_2 binding (Al > Ga > In), while showing similar $\Delta G^{\ddagger}_{loss}$ for H_2 loss from all (η^2-H_2)NiML complexes. Looking at the H_2 self-exchange diagram proposed in Figure 3c, the net reaction coordinate from the intermediate to either side simplifies to that for the binding of H_2 to NiML to form (η^2-H_2)NiML, yielding the more typical reaction coordinate diagram shown here.

Table S12. Rate constants (k_{bind}, k_{loss}), equilibrium constants (K_{H_2}), free energies ($\Delta G°$), and free energies of activation ($\Delta G^{‡}_{bind}$, $\Delta G^{‡}_{loss}$) for H_2 binding equilibria with NiML complexes.

	NiML Complex		
Value	M=Al	M=Ga	M=In
k_{bind} (x 10^9 M^{-1} s^{-1})[a]	1.4(1)	1.8(1)	10.5(5)
$k_{bind, rel}$	1.0	1.3(1)	7.5(6)
k_{loss} (x 10^5 s^{-1})[a]	550(30)	65(5)	6.0(3)
$k_{loss, rel}$	92(7)	10.7(8)	1.0
K_{H_2} (M^{-1})[b]	24(2)	270(30)	1.7(1) x 10^4
$\Delta G^{‡}_{loss}$ (kcal/mol)	9.1(2)	9.1(4)	9.4(4)
$\Delta G^{‡}_{bind}$ (kcal/mol)[c]	7.2(3)	6.2(5)	2.9(8)
$\Delta G°_{1M}$ (kcal/mol)[d]	−1.9(2)	−2.9(2)	−6.5(7)

[a] Determined via ^{31}P NMR lineshape analysis at 298 K (standard state: 1 M concentrations of all species, including H_2, in toluene-d_8). $k_{bind, rel}$ and $k_{loss, rel}$ are the relative rate constants at 298 K. [b] K_{H_2}= k_{bind}/k_{loss}, where k_{bind} and k_{loss} were determined at 298 K. Evaluating ln(K_{H_2}) vs. 1/T via lineshape analysis gives thermodynamic binding parameters that match within experimental error with those obtained under elevated pressures from the equilibrium studies (based on observed ^{31}P chemical shifts). At 298 K, the values for NiAlL (**1**) obtained from the equilibrium study under 34 atm H_2 (K_{H_2}= 25 ± 3) was within error of that obtained by lineshape analysis at 1 atm H_2 (24 ± 2). The corresponding values for NiGaL (**2**) at 298 K are K_{H_2}= 140 ± 60 (from 6.8 atm H_2 equilibrium study) and 270 ± 30 (from lineshape analysis), which are close to matching within experimental error ($\Delta G°_{bind}$ = −2.9 ± 0.2 kcal/mol vs. −3.3 ± 0.1 kcal/mol, respectively). For NiInL (**3**), the relevant comparison is K_{H_2}= 1.7(1) x 10^4 (from lineshape analysis) and K_{H_2}= 5(6) x 10^4 (from equilibrium study under 0.1 atm H_2), which both are within experimental error of one another and predict >98% bound **3**−H_2 species (relative to < 2 % of **3**) at equilibrium under 1 atm H_2 at 298 K. [c] $\Delta G^{‡}_{bind}$ was determined based on known $\Delta G^{‡}_{loss}$ and $\Delta G°$ values. [d] Based on van't Hoff plots for thermodynamic equilibrium studies.

V. Data for Quantum Chemical Studies and UV-Vis Spectroscopy

Table S13. Comparison between experimental and DFT-calculated structural metrics, as well as H_2 binding energies, for NiInL (**3**) and (η^2-H_2)NiInL (**3**−H_2). Bond distances are in Å, bond angles are in degrees, and binding free energies are in kcal/mol.

		Expt.	DFT-Calculated								
		X-ray/ Neutron	M06-L					M06-D3		PBE0	PBE0-D3
			bs0	bs1	bs2	bs3	bs4	bs1	bs4	bs1	bs1
NiInL	**Ni-In**	**2.457**	**2.522**	**2.522**	**2.510**	**2.474**	**2.490**	**2.513**	**2.469**	**2.492**	**2.478**
	In-N_{apical}	2.308	2.245	2.245	2.262	2.290	2.281	2.247	2.279	2.264	2.263
	Ni-N_{apical}	4.765	4.766	4.766	4.772	4.764	4.771	4.759	4.747	4.756	4.741
	Ni-P	2.252	2.243	2.243	2.247	2.211	2.250	2.262	2.257	2.252	2.240
	M-N_{amide}	2.118	2.044	2.044	2.061	2.070	2.069	2.041	2.065	2.053	2.053
	$\sum(\angle P{-}Ni{-}P)$	357.0	356.8	356.8	356.7	357.3	357.1	356.9	357.6	357.4	356.9
	$\sum(\angle N_{eq}\text{-}M\text{-}N_{eq})$	345.3	350.9	350.9	350.0	348.7	349.1	351.0	349.5	350.1	349.5
	Ni to P_3-plane	0.227	0.234	0.234	0.238	0.213	0.224	0.233	0.203	0.212	0.228
	M to N_3-plane	0.477	0.360	0.360	0.381	0.407	0.400	0.357	0.390	0.377	0.389
(H_2)NiInL	**Ni-In**	**2.492**	**2.602**	**2.603**	**2.580**	**2.555**	**2.561**	**2.579**	**2.531**	**2.564**	**2.542**
	In-N_{apical}	2.366	2.293	2.292	2.312	2.320	2.318	2.301	2.322	2.310	2.310
	Ni-N_{apical}	4.844	4.895	4.895	4.892	4.874	4.878	4.880	4.853	4.874	4.852
	Ni-H	1.61	1.639	1.639	1.636	1.624	1.631	1.645	1.628	1.603	1.598
	Ni-H	1.61	1.639	1.633	1.635	1.622	1.626	1.641	1.624	1.599	1.593
	H-H	0.80	0.836	0.835	0.837	0.844	0.845	0.825	0.837	0.839	0.841
	Ni-P	2.268	2.288	2.287	2.293	2.243	2.282	2.302	2.292	2.286	2.269
	M-N_{amide}	2.116	2.051	2.051	2.068	2.080	2.081	2.050	2.079	2.060	2.059
	$\sum(\angle P{-}Ni{-}P)$	355.1	352.4	352.3	352.5	353.2	352.7	352.6	353.2	353.7	353.4
	$\sum(\angle N_{eq}\text{-}M\text{-}N_{eq})$	344.0	347.4	347.5	346.3	346.4	346.1	347.2	345.9	346.8	346.1
	Ni to P_3-plane	0.32	0.369	0.370	0.366	0.341	0.358	0.365	0.349	0.334	0.340
	M to N_3-plane	0.51	0.426	0.425	0.448	0.449	0.455	0.429	0.458	0.438	0.450
ΔG°_{H2}	**kcal/mol**	**-3.0 ± 0.7**	**-2.3**	**-1.9**	**-2.7**	**-1.0**	**-3.4**	**1.4**	**-1.2**	**-0.4**	**-1.8**

Table S14. Differences in structural metrics between experiment and theory for NiInL (**3**) and (η^2-H_2)NiInL (**3**−H_2). Bond distances are in Å, and bond angles are in degrees. MSE and MUE are the mean signed and unsigned errors for bond distances.

		DFT-Calculated Differences Relative to Experiment								
		m06l					m06-d3		pbe0	pbe0-d3
		bs0	bs1	bs2	bs3	bs4	bs1	bs4	bs1	bs1
NiInL	Ni-In	0.064	0.064	0.053	0.017	0.033	0.056	0.012	0.035	0.021
	In-N_{apical}	-0.063	-0.063	-0.046	-0.018	-0.027	-0.061	-0.029	-0.044	-0.045
	Ni-N_{apical}	0.001	0.001	0.007	-0.001	0.006	-0.006	-0.018	-0.009	-0.024
	Ni-P	-0.009	-0.009	-0.005	-0.041	-0.002	0.010	0.005	0.000	-0.012
	M-N_{amide}	-0.075	-0.075	-0.057	-0.049	-0.050	-0.077	-0.054	-0.065	-0.065
	∑(∠P−Ni−P)	-0.2	-0.2	-0.3	0.3	0.1	-0.1	0.6	0.4	-0.1
	∑(∠N_{eq}-M-N_{eq})	5.6	5.6	4.7	3.4	3.8	5.7	4.3	4.8	4.2
	Ni to P_3-plane	0.007	0.007	0.011	-0.015	-0.004	0.006	-0.025	-0.015	0.001
	M to N_3-plane	-0.116	-0.116	-0.096	-0.070	-0.077	-0.119	-0.087	-0.099	-0.088
	MSE	-0.016	-0.016	-0.010	-0.018	-0.008	-0.016	-0.017	-0.017	-0.025
	MUE	0.043	0.043	0.034	0.025	0.024	0.042	**0.023**	0.031	0.033
(H_2)NiInL	Ni-In	0.110	0.111	0.088	0.063	0.069	0.087	0.039	0.072	0.050
	In-N_{apical}	-0.073	-0.074	-0.054	-0.046	-0.048	-0.065	-0.044	-0.056	-0.056
	Ni-N_{apical}	0.051	0.051	0.048	0.030	0.034	0.036	0.009	0.030	0.008
	Ni-H	0.029	0.029	0.026	0.014	0.021	0.035	0.018	-0.007	-0.012
	Ni-H	0.029	0.023	0.025	0.012	0.016	0.031	0.014	-0.011	-0.017
	H-H	0.036	0.035	0.037	0.044	0.045	0.025	0.037	0.039	0.041
	Ni-P	0.020	0.019	0.025	-0.025	0.014	0.034	0.024	0.018	0.001
	M-N_{amide}	-0.065	-0.065	-0.048	-0.036	-0.035	-0.066	-0.037	-0.056	-0.057
	∑(∠P−Ni−P)	-2.7	-2.8	-2.6	-1.9	-2.4	-2.5	-1.9	-1.4	-1.7
	∑(∠N_{eq}-M-N_{eq})	3.4	3.5	2.3	2.4	2.1	3.2	1.9	2.8	2.1
	Ni to P_3-plane	0.049	0.050	0.046	0.021	0.038	0.045	0.029	0.014	0.020
	M to N_3-plane	-0.084	-0.085	-0.062	-0.061	-0.055	-0.081	-0.052	-0.072	-0.060
	MSE	0.017	0.016	0.018	0.007	0.014	0.015	0.007	0.004	-0.005
	MUE	0.052	0.051	0.044	0.034	0.035	0.047	**0.028**	0.036	0.030

Table S15. Comparison of experimental and DFT-calculated structures for $(N_2)NiInL$ (**3**−N_2) with different DFT methods. Bond distances are in Å and bond angles are in degrees. MSE and MUE are the mean signed and unsigned errors for bond distances.

(N_2)NiInL	expt.	calc.				
		m06l/bs1	m06l/bs4	pbe0/bs1	pbe0-d3/bs1	m06-d3/bs4
		Structural Metrics				
Ni-In	2.5256(7)	2.664	2.63	2.621	2.598	2.586
Ni-N_2	1.848(3)	1.846	1.832	1.834	1.831	1.843
N-N	1.103(5)	1.115	1.123	1.103	1.103	1.109
Ni-P	2.311(1)	2.342	2.353	2.338	2.318	2.349
In-N_{apical}	2.385(3)	2.314	2.345	2.33	2.331	2.349
In-N_{amide}	2.118(2)	2.052	2.077	2.06	2.058	2.075
∑(∠P−Ni−P)	352.06(7)	349	350	351	351	351
∑(∠N−In−N)	341.4(2)	346	344	345	344	344
Ni to P_3-plane	0.38	0.45	0.44	0.41	0.41	0.41
In to N_3-plane	0.54	0.45	0.49	0.46	0.48	0.49
ν(N-N) cm^{-1}	2144 (KBr)	2207	2195	2315	2319	2285
		Differences in Structural Metrics				
Ni-In		0.138	0.104	0.095	0.072	0.060
Ni-N_2		-0.002	-0.016	-0.014	-0.017	-0.005
N-N		0.011	0.019	-0.001	-0.001	0.005
Ni-P		0.031	0.042	0.027	0.007	0.038
In-N_{apical}		-0.071	-0.040	-0.055	-0.054	-0.036
In-N_{amide}		-0.066	-0.041	-0.058	-0.060	-0.043
∑(∠P−Ni−P)		-3.1	-2.1	-1.1	-1.1	-1.1
∑(∠N−In−N)		4.6	2.6	3.6	2.6	2.6
Ni to P_3-plane		0.07	0.06	0.03	0.03	0.03
In to N_3-plane		-0.09	-0.05	-0.08	-0.06	-0.05
MSE		0.003	0.010	-0.007	-0.010	0.000
MUE		0.060	0.047	0.045	0.038	0.033

Table S16. Comparison of experimental and calculated H_2 binding energies for NiML complexes with different DFT methods (see Table S3 for method details; SMD solvent model used in all cases).

$\Delta G^\circ(H_2)$ binding (kcal/mol)					
M	expt.	m06l/bs1	pbe0/bs1	pbe0-d3/bs1	m06-d3/bs4
Solvent = toluene (298 K, 1 atm)					
none[a]	-	6.25	8.54	7.75	6.72
Al	1.6 ± 0.2	**2.76**	4.14	2.9	3.93
Ga	0.6 ± 0.3	**0.92**	2.18	0.83	0.71
In	-3.0 ± 0.7	**-1.85**	-0.35	-1.75	-1.16
Solvent = THF (298 K, 1 atm)					
none[a]		6.21	8.36	7.63	7.18
Al		2.62	3.91	2.67	3.52
Ga		-0.26	-0.26	1.66	0.33
In		-2.22	-2.22	-0.65	-2.01
Solvent = CH_3CN (298 K, 1 atm)					
none[a]		6.23	8.31	7.59	7.31
Al		2.65	3.87	2.64	3.44
Ga		-0.34	-0.34	1.46	0.19
In		-2.21	-2.21	-0.72	-2.04

[a] none indicates $NiLH_3$, which does not have a supporting metal.

Table S17. Comparison of experimental and calculated N_2 binding energies for NiML complexes with different DFT methods (see Table S3 for method details; SMD solvent model used in all cases).

$\Delta G^\circ(N_2)$ binding (kcal/mol)					
M	expt.	m06l/bs1	pbe0/bs1	pbe0-d3/bs1	m06-d3/bs4
Solvent = toluene (298 K, 1 atm)					
none[a]	-	5.86	15.36		8.02
Al	3.5 ± 0.3	6.25	13.58	9.95	6.05
Ga	2.1 ± 0.5	3.61	12.23	9.42	3.82
In	-1.2 ± 0.4	0.15	8.75	5.75	-1.81
Solvent = THF (298 K, 1 atm)					
none[a]		5.60	15.18		8.29
Al		6.13	13.48	9.87	6.33
Ga		3.15	11.69	8.92	4.07
In		-0.74	8.32	5.38	0.17
Solvent = CH_3CN (298 K, 1 atm)					
none[a]		5.64	15.15		8.59
Al		6.14	13.51	9.88	6.24
Ga		3.13	11.59	8.84	3.32
In		-0.81	8.25	5.36	-0.01

[a] none indicates $NiLH_3$, which does not have a supporting metal.

Table S18. Calculated structural metrics for $NiLH_3$, (η^2-H_2)$NiLH_3$, and (N_2)$NiLH_3$ with different DFT methods. Bond distances are in Å and bond angles are in degrees.

Functionals	M06-L/bs1	PBE0/bs1	PBE0-D3/bs1	M06-D3/bs4
		$NiLH_3$		
Ni-P	2.190	2.196	2.179	2.197
P-Ni-P	360	360	360	360
Ni-P_3	0.006	0.026	0.007	0.029
		(η^2-H_2)$NiLH_3$		
Ni-H	1.670	1.619	1.618	1.654
Ni-H	1.666	1.625	1.624	1.650
H-H	0.829	0.838	0.837	0.827
Ni-P	2.236	2.241	2.223	2.251
P-Ni-P	353	353	353	353
Ni-P_3	0.347	0.355	0.337	0.349
ν(H-H) cm^{-1}	3303	3089	3090	3383
		(N_2)$NiLH_3$		
Ni-N_2	1.853	1.834	1.841	1.853
N-N	1.119	1.108	1.108	1.114
Ni-P	2.278	2.276	2.262	2.279
P-Ni-P	344	343	344	344
Ni-P_3	0.531	0.544	0.533	0.539
ν(N-N) cm^{-1}	2175	2271	2272	2241

Table S19. Structural metrics of NiAlL, (η^2-H_2)NiAlL, and (N_2)NiAlL, as calculated with different DFT methods. Bond distances are in Å and bond angles are in degrees.

Functionals	M06-L/bs1	PBE0/bs1	PBE0-D3/bs1	M06-D3/bs4
NiAlL				
Ni-Al	2.488	2.487	2.474	2.489
Ni-P	2.194	2.204	2.190	2.205
Al-N_{apical}	2.100	2.107	2.104	2.098
Al-N_{amide}	1.878	1.880	1.880	1.884
P-Ni-P	359	359	359	359
N-Al-N	356	356	355	356
Ni-P_3	0.13	0.12	0.14	0.12
Al-N_3	0.23	0.23	0.24	0.22
(η^2-H_2)NiAlL				
Ni-Al	2.600	2.601	2.564	2.575
Ni-H	1.662	1.620	1.613	1.657
Ni-H	1.663	1.624	1.618	1.653
H-H	0.827	0.832	0.834	0.822
Ni-P	2.227	2.232	2.216	2.245
Al-N_{apical}	2.149	2.157	2.160	2.159
Al-N_{amide}	1.884	1.886	1.885	1.892
P-Ni-P	355	356	355	355
N-Al-N	353	353	352	353
Ni-P_3	0.29	0.28	0.28	0.28
Al-N_3	0.29	0.29	0.30	0.29
ν(H-H) cm^{-1}	3318	3162	3138	3435
(N_2)NiAlL				
Ni-Al	2.649	2.646	2.611	2.610
Ni-N_2	1.879	1.855	1.851	1.874
N-N	1.115	1.104	1.104	1.110
Ni-P	2.262	2.271	2.251	2.276
Al-N_{apical}	2.146	2.157	2.159	2.160
Al-N_{amide}	1.881	1.881	1.881	1.889
P-Ni-P	351	352	352	352
N-Al-N	354	353	353	353
Ni-P_3	0.39	0.37	0.38	0.37
Al-N_3	0.28	0.28	0.29	0.29
ν(N-N) cm^{-1}	2206	2304	2306	2277

Table S20. Structural metrics of NiGaL, (η^2-H$_2$)NiGaL, and (N$_2$)NiGaL, as calculated with different DFT methods. Bond distances are in Å and bond angles are in degrees.

	expt.			calc.	
Functional	crystal	M06-L/bs1	PBE0/bs1	PBE0-D3/bs1	M06-D3/bs4
			NiGaL		
Ni-Ga	2.379	2.431	2.440	2.432	2.417
Ni-P	2.210	2.211	2.218	2.204	2.219
M-N$_{apical}$	2.216(3)	2.217	2.204	2.198	2.202
M-N$_{amide}$	1.954(2)	1.952	1.937	1.936	1.936
P-Ni-P	359.01(9)	358	359	359	359
N-Ga-N	349.5(3)	351	352	352	352
Ni-P$_3$	0.13	0.16	0.13	0.15	0.12
Ga-N$_3$	0.37	0.34	0.31	0.32	0.32
			(η^2-H$_2$)NiGaL		
Ni-Ga		2.499	2.509	2.482	2.473
Ni-H		1.650	1.613	1.607	1.644
Ni-H		1.649	1.609	1.602	1.641
H-H		0.830	0.835	0.837	0.825
Ni-P		2.248	2.248	2.233	2.261
Ga-N$_{apical}$		2.291	2.281	2.281	2.287
Ga-N$_{amide}$		1.960	1.945	1.944	1.948
P-Ni-P		355	356	355	356
N-Ga-N		346	348	347	347
Ni-P$_3$		0.30	0.27	0.28	0.27
Ga-N$_3$		0.42	0.39	0.41	0.41
ν(H-H) cm^{-1}		3282	3127	3105	3406
			(N$_2$)NiGaL		
Ni-Ga		2.571	2.582	2.551	2.532
Ni-N$_2$		1.870	1.848	1.845	1.871
N-N		1.114	1.102	1.102	1.108
Ni-P		2.295	2.293	2.276	2.300
Ga-N$_{apical}$		2.310	2.297	2.301	2.312
Ga-N$_{amide}$		1.959	1.942	1.941	1.946
P-Ni-P		352	353	353	354
N-Ga-N		345	347	346	346
Ni-P$_3$		0.37	0.35	0.35	0.34
Ga-N$_3$		0.44	0.41	0.43	0.43
ν(N-N) cm^{-1}		2217	2321	2323	2291

Table S21. Energy decomposition analysis (EDA) of Ni−H_2 binding interaction for (η^2-H_2)$NiLH_3$ and the (η^2-H_2)NiML series, as computed with PBE0-D3 using ADF.

Energy (kcal/mol)	H_2-$NiLH_3$	H_2-NiAlL	H_2-NiGaL	H_2-NiInL
ΔE_{elstat}	-60.3	-56.3	-57.2	-58.9
ΔE_{Pauli}	89.2	78.5	78.1	77.6
ΔE_{disp}	-2.1	-2.2	-2.2	-2.2
ΔE_{orb}	-41.9	-37.5	-38.2	-39.9
ΔE_{int}(PBE0-D3)	-15.1	-17.5	-19.5	-23.4
ΔE_{int}(M06-L)[a]	-14.9	-16.9	-18.6	-21.3

[a] The M06-L interaction energies (ΔE_{int}) are listed to show that M06-L and PBE0-D3 interaction energies have moderately good agreement with each other.

Table S22. Orbital interaction energy contributions from the top three NOCV pairs to Ni−H_2 bonding.

NOCV	Type	(H_2)$NiLH_3$	(H_2)NiAlL	(H_2)NiGaL	(H_2)NiInL
1	σ_{H2} → 4p (Ni)	-18.3 (44%)	-14.5 (39%)	-14.8 (39%)	-15.2 (38%)
2	$3d_{xz}$(Ni) → σ^*_{H2}	-14.6 (35%)	-12.8 (34%)	-13.0 (34%)	-13.9 (35%)
3	σ_{H2} → 4p (Ni)	-6.4 (15%)	-6.9 (18%)	-6.9 (18%)	-7.3 (18%)
sub-total[a]		-39.3	-34.2	-34.7	-36.4

[a] The sub-total of the orbital interaction energies for the top 3 NOCV pairs accounts for the majority of the ΔE_{orb} value in the prior table.

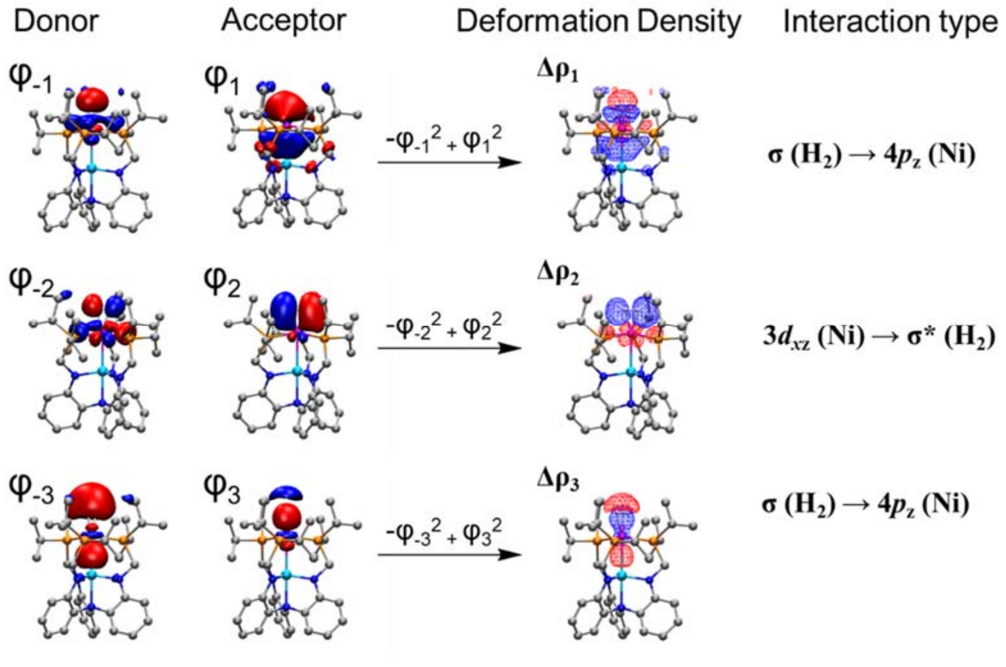

Figure S53. Deformation density contributions ($\Delta\rho_n$, isovalue 0.04 a.u.) of NOCV pairs for Ni−H_2 bonding in (η^2-H_2)NiInL. Similar densities were computed for (η^2-H_2)$NiLH_3$, (η^2-H_2)NiAlL, and (η^2-H_2)NiGaL.

Table S23. Energy decomposition analysis of the Ni−N_2 binding interaction for $(N_2)NiLH_3$ and the (N_2)NiML series, as computed with PBE0-D3 using ADF.

Energy (kcal/mol)	$(N_2)NiLH_3$	(N_2)NiAlL	(N_2)NiGaL	(N_2)NiInL
ΔE_{elstat}	-71.9	-60.7	-59.4	-62.4
ΔE_{Pauli}	115.9	96.1	92.4	95.3
ΔE_{disp}	-5.8	-5.0	-5.0	-4.9
ΔE_{orb}	-61.5	-51.2	-49.7	-54.5
ΔE_{int}(PBE0-D3)	-23.4	-20.7	-21.7	-26.5
ΔE_{int}(M06-L)	-25.1	-23.2	-23.5	-26.9

Table S24a. Orbital interaction energy contributions from the top four NOCV pairs to Ni−N_2 bonding.

NOCV	Type	$(N_2)NiLH_3$	(N_2)NiAlL	(N_2)NiGaL	(N_2)NiInL
1	$3d_{xz}$ (Ni) → π*(N-N)	-17.2	-16.8	-12.9	-14.6
2	$3d_{yz}$ (Ni) → π*(N-N)	-17.2	-12.7	-12.9	-14.6
3	N LP → $4p_z$ (Ni)	-20.5	-13.7	-15.7	-16.6
4	N LP → $4p_z$ (Ni)	-5.4	-5.1	-5.4	-5.9
1+2	3d (Ni) → π*(N-N)	-34.4 57%	-29.5 61%	-25.8 55%	-29.1 56%
3+4	N LP → $4p_z$ (Ni)	-25.9 43%	-18.8 39%	-21.1 45%	-22.5 44%
sub-total		-60.2	-48.3	-46.9	-51.6

[a]The sub-total of the orbital interaction energies for the top 4 NOCV pairs accounts for the majority of the ΔE_{orb} value in the prior table.

Table S24b. The donor-acceptor stabilization energy of the Ni→M dative interaction in NiAlL (**1**), NiGaL (**2**), and NiInL (**3**), as determined by natural bond orbital analysis using M06-L/bs1 method.

	Donor-Acceptor Stabilization Energy (kcal/mol)		
Interaction type	NiAlL	NiGaL	NiInL
Ni ($3d_{z2}$) → M (s)	39.8	71.7	135.0
Ni ($3d_{z2}$) → M (p)	4.9	12.5	27.9
Ni → M interaction	44.7	84.2	162.9

Donation from Ni to M via Ni(3dz2) → Al(3pz/3s), Ga(4pz/4s), and In(5pz/5s).

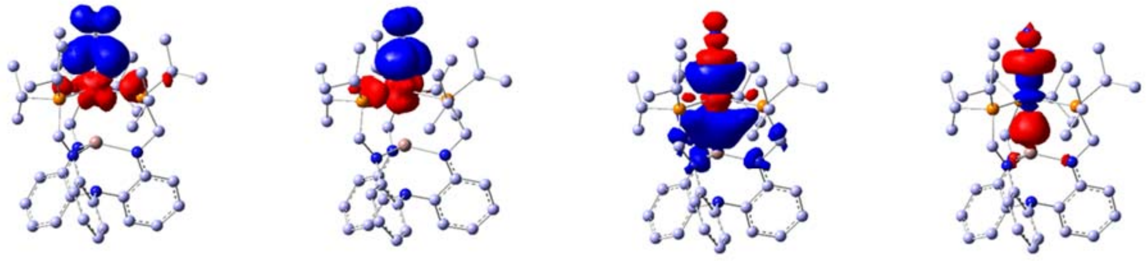

$\Delta\rho_{NOCV1}$
d_{xz} (Ni) → π*(N-N)

$\Delta\rho_{NOCV2}$
d_{yz} (Ni) → π*(N-N)

$\Delta\rho_{NOCV3}$
N LP→ $4p_z$ (Ni)

$\Delta\rho_{NOCV4}$
N LP→ $4p_z$ (Ni)

Figure S54. Deformation density contributions ($\Delta\rho_n$, isovalue 0.04 a.u.) of NOCV pairs for Ni−N_2 in (N_2)NiInL. Similar densities were computed for the $(N_2)NiLH_3$, (N_2)NiAlL, (N_2)NiGaL complexes.

Table S25. Structural comparison of (η^2-H_2)NiML (**B**), the transition state (**TS**) for H−H cleavage, and H−Ni(μ−H)ML (**C**, see image), as optimized with M06-L/bs1 for M = Al, Ga, and In.

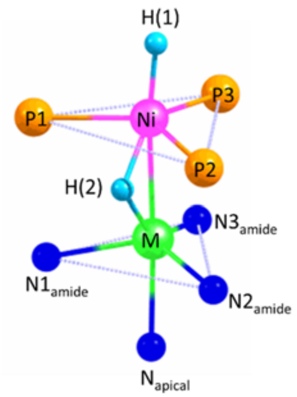

	Al			Ga			In		
	B	**TS**	**C**	**B**	**TS**	**C**	**B**	**TS**	**C**
Ni-H(1)	1.662	1.575	1.502	1.650	1.468	1.510	1.633	1.561	1.515
Ni-H(2)	1.663	1.465	1.489	1.649	1.562	1.501	1.639	1.476	1.500
M-H(2)		2.815	1.749		2.665	1.831		2.682	1.960
H(1)-H(2)	0.827	2.299	2.885	0.830	2.331	2.835	0.835	2.398	2.857
∠H(1)-Ni-H(2)	28.8	98.3	149.4	29.2	100.6	140.6	29.6	104.3	142.8
H(2) to P_3-plane		0.04[a]	1.073		0.06[a]	0.993		0.09[a]	0.914
∠Ni-H(2)-M		64.7	110.9		66.0	98.6		69.3	97.2
img. Freq. (cm^{-1})		277			298			328	
Ni-M	2.6	2.558	2.670	2.499	2.464	2.536	2.603	2.565	2.613
Ni-P	2.227	2.200	2.225	2.248	2.219	2.233	2.287	2.255	2.281
Al-N_{apical}	2.149	2.148	2.076	2.291	2.279	2.207	2.292	2.276	2.236
Al-N_{amide}	1.884	1.889	1.886	1.960	1.966	1.960	2.051	2.054	2.051
∑(∠P−Ni−P)	355	356.8	358.1	355.0	357.0	358.4	352.3	355.4	356.9
∑(∠N_{eq}-M-N_{eq})	353	353.2	356.8	346.0	347.2	351.7	347.5	348.7	351.6
Ni to P_3-plane	0.29	0.23	0.18	0.30	0.22	0.16	0.37	0.28	0.23
M to N_3-plane	0.29	0.29	0.20	0.42	0.41	0.33	0.43	0.40	0.35

[a] The close to zero values for the H(2) to P_3-plane distance in all the TS structures means that H(2) is co-planar with the phosphines. This value changes dramatically in **C**, which shows that the hydride is re-positioned below the P_3-plane and becomes a bridging hydride in the product of H−H cleavage. This suggests that the supporting metal does not assist directly in the **TS** for H−H cleavage, but subsequently stabilizes the resulting nickel dihydride species that initially forms via oxidative addition. This H−H activation sequence is also consistent with the dramatic shortening of the M−H(2) distance upon moving from **TS** to **C**. Related Ni→B diphosphine complexes affect heterolytic H_2 cleavage where both Ni and B participate in the TS for H−H cleavage,[46-48] whereas the more sterically protected group 13 supporting metal in NiML complexes cannot directly interact with H_2 to affect cleavage. Instead, the resulting Ni dihydride species is stabilized as HNi(μ-H)ML (though not enough to allow it to be observed experimentally); this is proposed to be an important intermediate in olefin hydrogenation catalysis.[32,49]

Table S26. Free energies (kcal/mol) in THF and toluene for isomerization between (η^2-H_2)NiML (**B**) and H−Ni(μ−H)ML (**C**) complexes via H−H cleavage. Both standard conditions (298.15 K, 1 atm) and high pressure and low T (193 K, 34 atm) were considered. All calculations were performed with the M06L/bs1 method and SMD solvation model. Note that **A** = NiML and **TS** = transition state between **B** and **C**.

Index	**solvent = THF (SMD)**	298.15 K, 1 atm			193K, 34 atm		
	Reactions for energy (kcal/mol) calculation	Al	Ga	In	Al	Ga	In
A	NiML(solv)	0	0	0	0	0	0
B	H_2(gas) + NiML(solv)→ (η^2-H_2)NiML	2.6	-0.3	-2.2	0.3	-4.2	-6.3
TS		22.2	18.9	18.4	19.3	14.2	12.7
C	H_2(gas) + NiML(solv)→ H−Ni(μ−H)ML	14.9	17.0	16.3	12.2	14.3	12.0
	solvent = Toluene (SMD)	298.15 K, 1 atm			193K, 34 atm		
	Reactions for energy (kcal/mol) calculation	Al	Ga	In	Al	Ga	In
A	NiML(solv)	0	0	0	0	0	0
B	H_2(gas) + NiML(solv)→ (η^2-H_2)NiML	2.8	0.9	-1.9	0.5	-3.0	-5.9
TS		23.5	21.0	20.2	20.5	16.3	14.5
C	H_2(gas) + NiML(solv)→ H−Ni(μ−H)ML	15.2	18.1	17.3	12.5	15.5	13.0

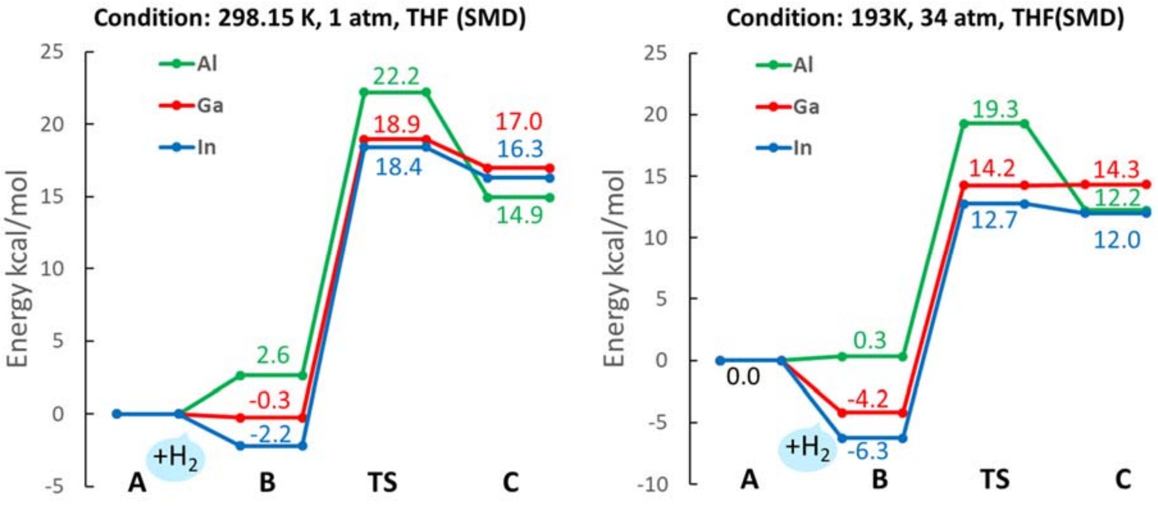

Figure S55. Energy profile for H−H cleavage via (η^2-H_2)NiML (**B**) and (H−Ni(μ−H)ML (**C**) complexes and the calculated transition state (**TS**). Free energies (kcal/mol) in THF (SMD) are computed using M06-L/bs1 method under the same two conditions described in Table S26 (above).

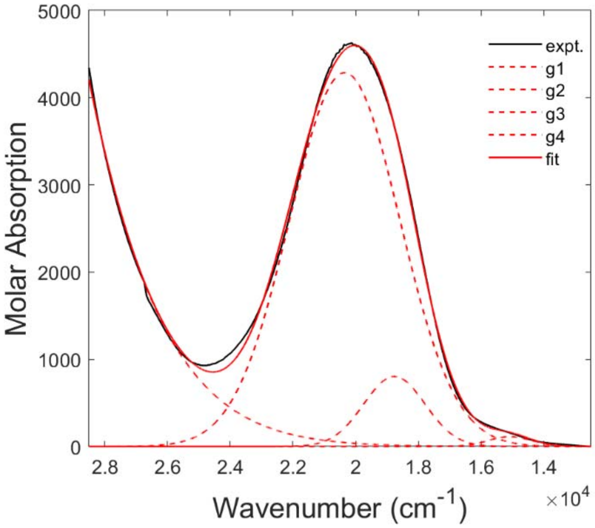

Figure S56. The experimental UV-Vis spectrum of $NiLH_3$ and fittings with four Gaussian functions, $f(x) = a_0 \times e^{-((a_1 - x)/a_2)^2}$, with the parameters shown in the following table.

Table S27. Parameters of the fitted Gaussian functions, $f(x) = a_0 \times e^{-((a_1 - x)/a_2)^2}$, for the experimental UV-Vis spectrum of $NiLH_3$.

Gaussian Function	1	2	3	4
a_0, Intensity (molar abs)	78920 ± 51800	4286.2 ± 58.7	802.57 ± 103	112.66 ± 8.92
a_1, Energy (cm^{-1})	42181 ± 2790	20350 ± 35.8	18766 ± 24.3	15084 ± 84.1
a_2, Linewidth (cm^{-1})	7990.9 ± 741	2486.8 ± 20.5	1382.4 ± 77.9	977.12 ± 106
Peak energies				
Energy (cm^{-1})	42181	20350	18766	15084
Energy (nm)	**237**	**491**	**533**	**663**
Energy (eV)	5.23	2.52	2.33	1.87

Table S28. UV-Vis data for $NiLH_3$ and **1-3** with TD-DFT data (in parentheses) and assignments (in eV).

Peak	**Transition**	**$NiLH_3$**	**1**	**2**	**3**
I	$d_{x^2-y^2}/d_{xy}$ → LUMO	1.87 (2.53)	2.07 (2.16)	1.94 (1.91)	1.77 (1.93)
II	d_{yz}/d_{xz} → LUMO	2.53 (3.00)	2.53 (2.84)	2.44 (2.59)	2.34 (2.61)
III	π-ligand + d_{z^2} → LUMO	2.33 (2.80)[a]	2.88 (3.02)	2.67 (2.60)	2.54 (2.76)

[a] Pure Ni d_{z^2} → LUMO transition.

Table S29. (**a**) Predicted TD-DFT transitions (***in nm***) for UV-Vis spectra of $NiLH_3$ and NiML complexes using multiple functionals and basis sets. Note: all methods predict similar transitions for NiGaL and NiInL.

$NiLH_3$	M06-D3/bs4	M06/bs1	M06-L/bs1	PBE0/bs1	PBE0-D3/bs1
$d_{x^2-y^2}/d_{xy}$ → LUMO	490	474	500	472	461
d_{z^2} → LUMO	443	402	499	430	421
d_{yz}/d_{xz} → LUMO	413	384	455	401	391

NiAlL	M06-D3/bs4	M06/bs1	M06-L/bs1	PBE0/bs1	PBE0-D3/bs1
$d_{x^2-y^2}/d_{xy}$ → LUMO	573	552	542	551	539
d_{yz}/d_{xz} → LUMO	437	405	440	420	409
Ligands N,C + d_{z^2} → LUMO	410	397	500	406	401
Ligands N,C + d_{xz}/d_{yz} → LUMO	343	338	400	339	336
d_{z^2} → LUMO	363	347	368	355	347

NiGaL	M06-D3/bs4	M06/bs1	M06-L/bs1	PBE0/bs1	PBE0-D3/bs1
$d_{x^2-y^2}/d_{xy}$ → LUMO	650	–	597	609	593
d_{yz}/d_{xz} → LUMO	478	–	438	453	440
Ligands N,C + d_{z^2} → LUMO	448	–	557	435	429
Ligands N,C + d_{xz}/d_{yz} → LUMO	388	–	497	377	373
d_{z^2} → LUMO	384	–	393	374	366

NiInL	M06-D3/bs4	M06/bs1	M06-L/bs1	PBE0/bs1	PBE0-D3/bs1
$d_{x^2-y^2}/d_{xy}$ → LUMO	642	607	583	598	584
d_{yz}/d_{xz} → LUMO	475	439	435	444	433
Ligands N,C + d_{z^2} → LUMO	449	424	537	428	422
Ligands N,C + d_{xz}/d_{yz} → LUMO	403	380	491	383	379
d_{z^2} → LUMO	385	382	402	372	364

Table S29. (**b**) Predicted TD-DFT transitions (***in eV***) for UV-Vis spectra of $NiLH_3$ and NiML complexes using multiple functionals and basis sets. Note: all methods predict similar transitions for NiGaL and NiInL.

$NiLH_3$	M06-D3/bs4	M06/bs1	M06-L/bs1	PBE0/bs1	PBE0-D3/bs1
$d_{x^2-y^2}/d_{xy}$ → LUMO	2.53	2.62	2.48	2.63	2.69
d_{z^2} → LUMO	2.80	3.08	2.48	2.88	2.94
d_{yz}/d_{xz} → LUMO	3.00	3.23	2.72	3.09	3.17

NiAlL	M06-D3/bs4	M06/bs1	M06-L/bs1	PBE0/bs1	PBE0-D3/bs1
$d_{x^2-y^2}/d_{xy}$ → LUMO	2.16	2.25	2.29	2.25	2.30
d_{yz}/d_{xz} → LUMO	2.84	3.06	2.82	2.96	3.03
Ligands N,C + d_{z^2} → LUMO	3.02	3.12	2.48	3.06	3.09
Ligands N,C + d_{xz}/d_{yz} → LUMO	3.61	3.67	3.10	3.66	3.69
d_{z^2} → LUMO	3.42	3.57	3.37	3.49	3.57

NiGaL	M06-D3/bs4	M06/bs1	M06-L/bs1	PBE0/bs1	PBE0-D3/bs1
$d_{x^2-y^2}/d_{xy}$ → LUMO	1.91	–	2.08	2.04	2.09
d_{yz}/d_{xz} → LUMO	2.59	–	2.83	2.74	2.82
Ligands N,C + d_{z^2} → LUMO	2.77	–	2.23	2.85	2.89
Ligands N,C + d_{xz}/d_{yz} → LUMO	3.20	–	2.49	3.29	3.32
d_{z^2} → LUMO	3.23	–	3.15	3.31	3.39

NiInL	M06-D3/bs4	M06/bs1	M06-L/bs1	PBE0/bs1	PBE0-D3/bs1
$d_{x^2-y^2}/d_{xy}$ → LUMO	1.93	2.04	2.13	2.07	2.12
d_{yz}/d_{xz} → LUMO	2.61	2.82	2.85	2.79	2.86
Ligands N,C + d_{z^2} → LUMO	2.76	2.92	2.31	2.90	2.94
Ligands N,C + d_{xz}/d_{yz} → LUMO	3.08	3.26	2.53	3.24	3.27
d_{z^2} → LUMO	3.22	3.24	3.08	3.34	3.41

Table S29. (**c**) Predicted TD-DFT transitions (***in cm***$^{-1}$) for UV-Vis spectra of $NiLH_3$ and NiML complexes using multiple functionals and basis sets. Note: all methods predict similar transitions for NiGaL and NiInL.

$NiLH_3$	M06-D3/bs4	M06/bs1	M06-L/bs1	PBE0/bs1	PBE0-D3/bs1
$d_{x^2-y^2}/d_{xy}$ → LUMO	20409	21118	20000	21199	21687
d_{z^2} → LUMO	22559	24855	20040	23247	23752
d_{yz}/d_{xz} → LUMO	24205	26019	21978	24925	25579

NiAlL	M06-D3/bs4	M06/bs1	M06-L/bs1	PBE0/bs1	PBE0-D3/bs1
$d_{x^2-y^2}/d_{xy}$ → LUMO	17457	18117	18450	18145	18553
d_{yz}/d_{xz} → LUMO	22897	24701	22727	23835	24465
Ligands N,C + d_{z^2} → LUMO	24384	25188	20000	24640	24953
Ligands N,C + d_{xz}/d_{yz} → LUMO	29152	29623	25000	29536	29769
d_{z^2} → LUMO	27558	28829	27174	28171	28827

NiGaL	M06-D3/bs4	M06/bs1	M06-L/bs1	PBE0/bs1	PBE0-D3/bs1
$d_{x^2-y^2}/d_{xy}$ → LUMO	15385	–	16750	16417	16863
d_{yz}/d_{xz} → LUMO	20921	–	22831	22097	22718
Ligands N,C + d_{z^2} → LUMO	22321	–	17953	22989	23296
Ligands N,C + d_{xz}/d_{yz} → LUMO	25773	–	20121	26526	26785
d_{z^2} → LUMO	26042	–	25445	26734	27353

NiInL	M06-D3/bs4	M06/bs1	M06-L/bs1	PBE0/bs1	PBE0-D3/bs1
$d_{x^2-y^2}/d_{xy}$ → LUMO	15570	16462	17153	16734	17112
d_{yz}/d_{xz} → LUMO	21064	22759	22989	22539	23077
Ligands N,C + d_{z^2} → LUMO	22248	23568	18622	23374	23685
Ligands N,C + d_{xz}/d_{yz} → LUMO	24805	26301	20367	26134	26398
d_{z^2} → LUMO	25975	26159	24876	26910	27497

Figure S57. **(A)** UV-Vis spectra and **(B)** TD-DFT (M06-D3) predicted spectra of $NiLH_3$ (gray), NiAlL (green), and NiGaL (red) in THF. **(C)** UV/Vis spectra of NiInL (blue), (η^2-H_2)NiInL (pink), and (N_2)NiInL (orange). The inset shows the corresponding simulated spectra. Spectra are plotted as a function of both wavenumbers (*top row*, **A1**-**C1**) and eV (*bottom row*, **A2**-**C2**).

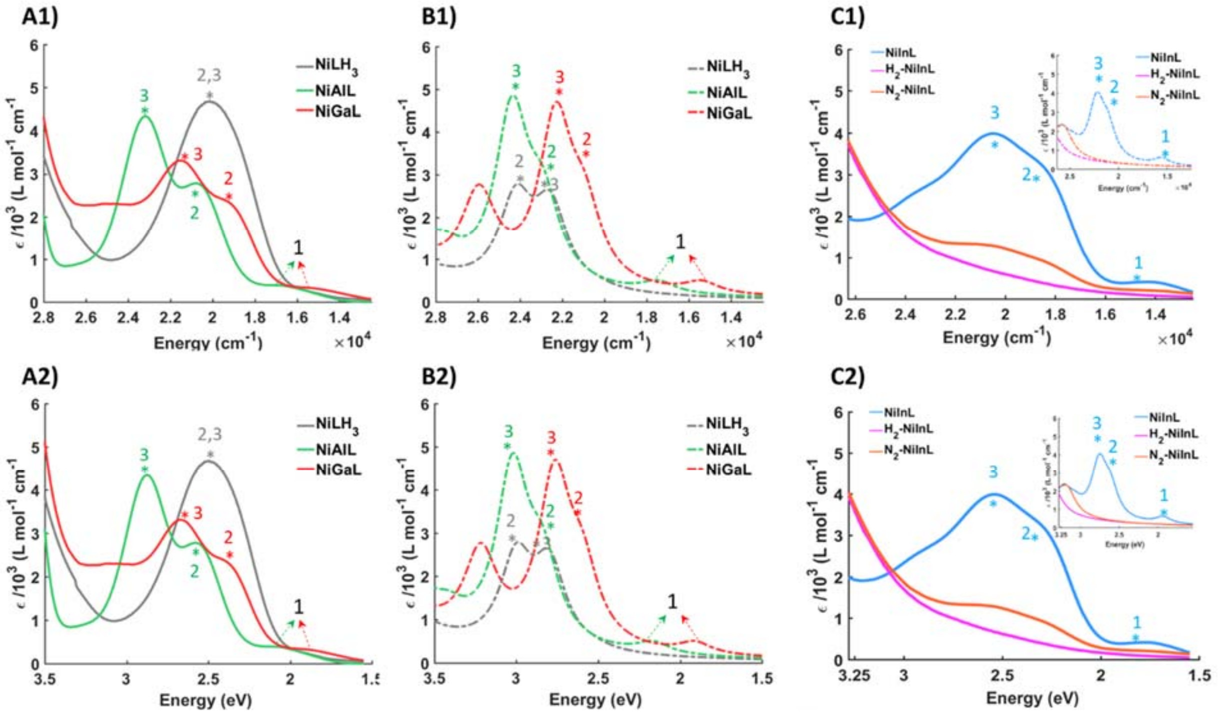

Figure S58. TD-DFT calculated UV-Vis spectra of $NiLH_3$, NiAlL, NiGaL, and NiInL using M06-D3/bs4 in THF (SMD).

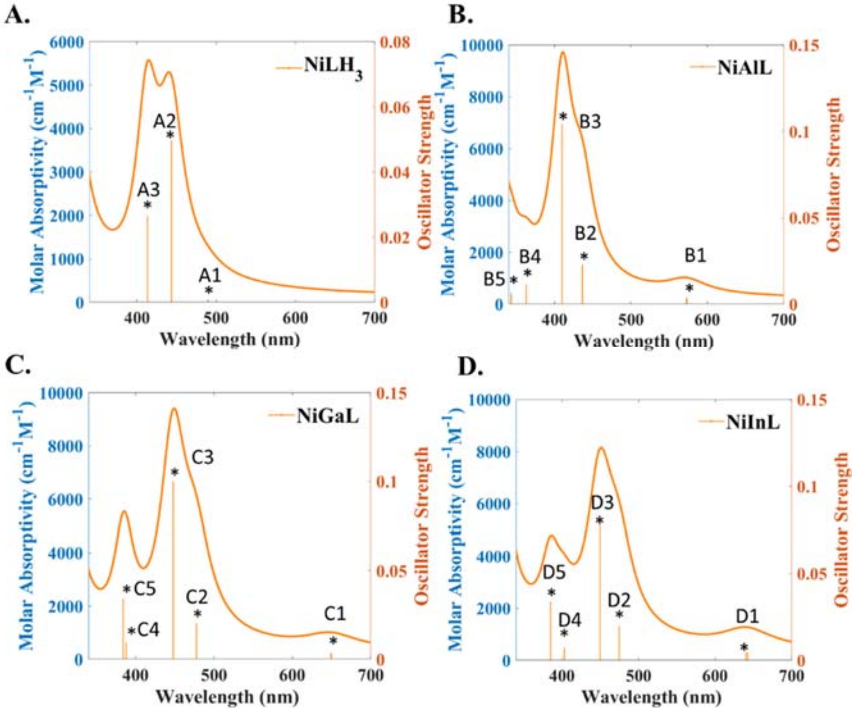

Table S30. M06-D3/bs4 TD-DFT transition assignments for NiLH$_3$, NiAlL, NiGaL, and NiInL (refer to prior figure for index labels).

Transition Types	M06-D3			expt.
NiLH$_3$	Index	nm	*f*	nm
$d_{x^2-y^2}/d_{xy}$ → LUMO	A1	490	0.0008	497
d_{yz}/d_{xz} → LUMO	A3	413	0.0264	
d_{z^2} → LUMO	A2	443	0.0497	
NiAlL	Index	nm	*f*	nm
$d_{x^2-y^2}/d_{xy}$ → LUMO	B1	573	0.0034	600
d_{yz}/d_{xz} → LUMO	B2	437	0.0225	490
Ligands N,C + (d_{z^2}) → LUMO	B3	410	0.1043	430
Ligands N,C + d_{xz}/d_{yz} → LUMO	B5	343	0.0063	
d_{z^2} → LUMO	B4	363	0.0114	
NiGaL	Index	nm	*f*	nm
$d_{x^2-y^2}/d_{xy}$ → LUMO	C1	650	0.0034	638
d_{yz}/d_{xz} → LUMO	C2	478	0.0202	508
Ligands N,C + d_{z^2} → LUMO	C3	448	0.0999	464
Ligands N,C + d_{xz}/d_{yz} → LUMO	C4	388	0.0094	
d_{z^2} → LUMO	C5	384	0.0344	
NiInL	Index	nm	*f*	nm
$d_{x^2-y^2}/d_{xy}$ → LUMO	D1	642	0.0046	699
d_{yz}/d_{xz} → LUMO	D2	475	0.0195	530
Ligands N,C + (d_{z^2}) → LUMO	D3	449	0.078	488
Ligands N,C + d_{xz}/d_{yz} → LUMO	D4	403	0.0071	
d_{z^2} → LUMO	D5	385	0.0337	

M06-D3/bs4 Kohn-Sham Molecular Orbitals

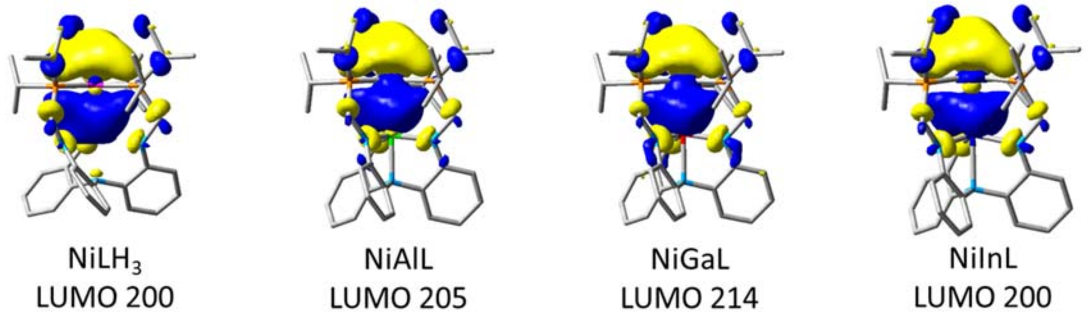

M06-L/bs1 Kohn-Sham Molecular Orbitals

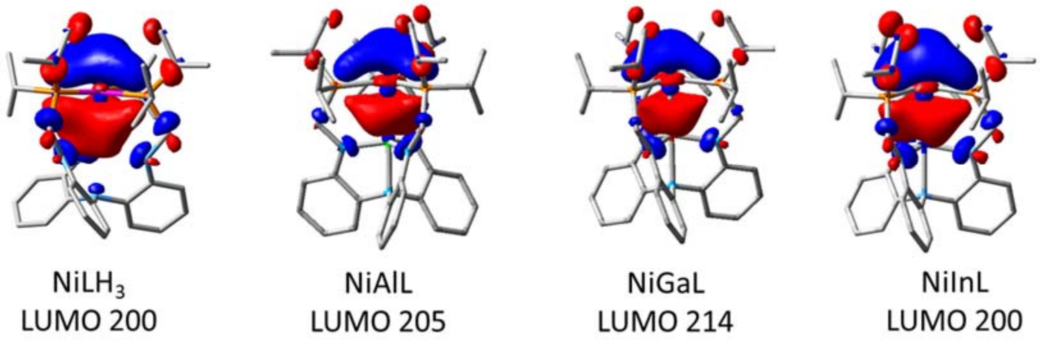

Figure S59. LUMOs of $NiLH_3$ and NiML complexes, as calculated with M06-D3/bs4. Note: The molecular orbital analyses below are shown for M06-L/bs1 using Mulliken population analysis, which is known to be basis set sensitive and may give erroneous atomic orbital contributions for some large basis set (bs4). We further note that the MOs for M06-L/bs1are identical to those for M06-D3/bs4.

Table S31. Molecular orbital composition analysis (M06-L/bs1) for the LUMOs of $NiLH_3$ and NiML.

M06-L/bs1			**Ni**			**M**		**P**
		# Orb	d	s	p	s	p	p
$NiLH_3$	LUMO	200			0.23			0.30
NiAlL	LUMO	205	0.06		0.14	0.16	0.10	0.18
NiGaL	LUMO	214	0.09		0.16	0.17	0.08	0.18
NiInL	LUMO	200	0.08	0.07	0.11	0.21	0.12	0.23

Table S32. Selected molecular orbitals of NiGaL, (η^2-H_2)NiGaL and (N_2)NiGaL (M06-D3/bs4).

	NiGaL	H_2-NiGaL	N_2-NiGaL
Acceptor MO (empty)	LUMO 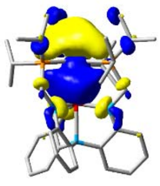	LUMO 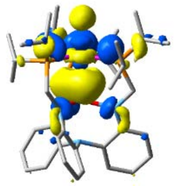	LUMO+2 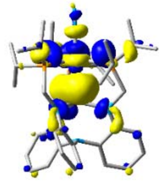
Occupied $d_{x^2-y^2}$	HOMO 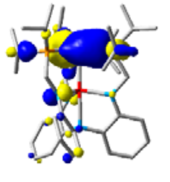	HOMO-3 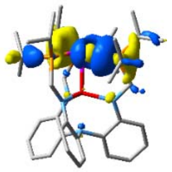	HOMO-3 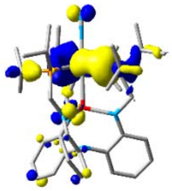
Occupied d_{xy}	HOMO-1 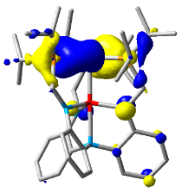	HOMO-4 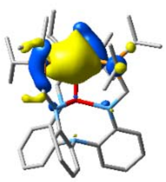	HOMO-4 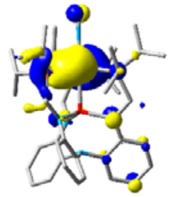
Occupied d_{z^2}	HOMO-5 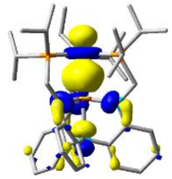	HOMO-5 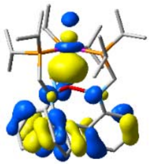	HOMO-5 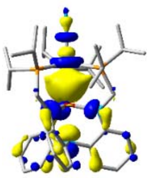

Table S33. The lowest-energy electronic transition of $NiLH_3$, NiML, and their respective H_2 and N_2 adducts. TD-DFT calculations were performed using M06-D3/bs4 with SMD solvation (solvent = THF).

	NiML	(η^2-H_2)NiML	(N_2)NiML
1st transition	$d_{x^2-y^2}/d_{xy} \rightarrow$ LUMO	$d_{x^2-y^2}/d_{xy}$ + Ligand P $\rightarrow$ LUMO	$d_{x^2-y^2}/d_{xy}$ + Ligand P $\rightarrow$ LUMO
Al	573	353	372(2nd transition) [a]
Ga	650	378	396
In	642	375	391

	$NiLH_3$	(η^2-H_2)$NiLH_3$	(N_2)$NiLH_3$
1st transition	$d_{x^2-y^2}/d_{xy} \rightarrow$ LUMO	$d_{z^2} \rightarrow$ H-H sigma*	$d_{z^2} \rightarrow$ N-N pi*
none[b]	490	340	418

[a] The lowest-energy transition for (N_2)NiAlL is Ni d_{xy} + Ligand P → N−N pi* (392 nm).

[b] none signifies $NiLH_3$, which has no supporting metal.

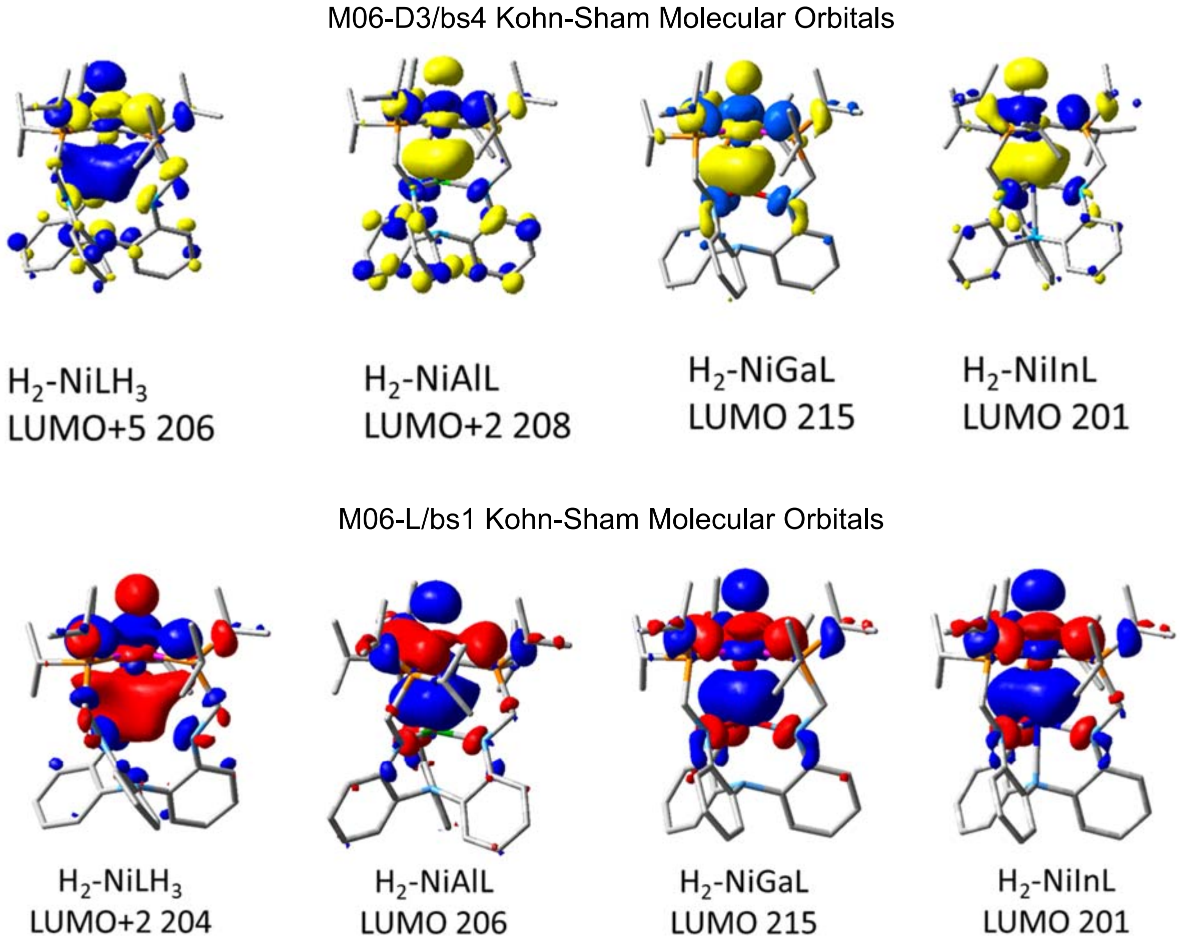

Figure S60. The primary acceptor MOs of (η^2-H_2)NiML and (η^2-H_2)NiLH$_3$, as calculated with M06-D3/bs4. They are referred to as "*acceptor MOs*" as not all of these are LUMOs. Note: The molecular orbital analyses below are shown for M06-L/bs1 using Mulliken population analysis, which is known to be basis set sensitive and may give erroneous atomic orbital contributions for some large basis set (bs4). We further note that the MOs for M06-L/bs1 are identical to those for M06-D3/bs4.

Table S34. Molecular orbital composition analysis (M06-L/bs1) of the *acceptor MO* of (η^2-H_2)NiLH$_3$ (LUMO+2), (η^2-H_2)NiAlL (LUMO), (η^2-H_2)NiGaL (LUMO), and (η^2-H_2)NiInL (LUMO).

M06-L/bs1[a]			**Ni**			**M**		**P**
No.		# Orb	d	s	p	s	p	p
(η^2-H_2)NiLH$_3$	LUMO+2	204	0.06		0.09			0.28
(η^2-H_2)NiAlL	LUMO	206	0.13		0.08	0.11	0.07	
(η^2-H_2)NiGaL	LUMO	215	0.18		0.07	0.16	0.07	
(η^2-H_2)NiInL	LUMO	201	0.13			0.23	0.12	0.05

[a] For the NiML-H$_2$ adducts, the *acceptor MO* are composed of Ni, M, and P atomic orbitals, similar to the composition of the LUMOs of the naked NiML species. The shape of the orbitals indicates a small contribution from H atomic orbitals (< 5%).

Figure S61. Simulated UV-Vis spectrum of (η^2-H_2)NiLH_3, (η^2-H_2)NiAlL, (η^2-H_2)NiGaL, and (η^2-H_2)NiInL as calculated by TD-DFT with M06-D3/bs4 in THF (SMD)

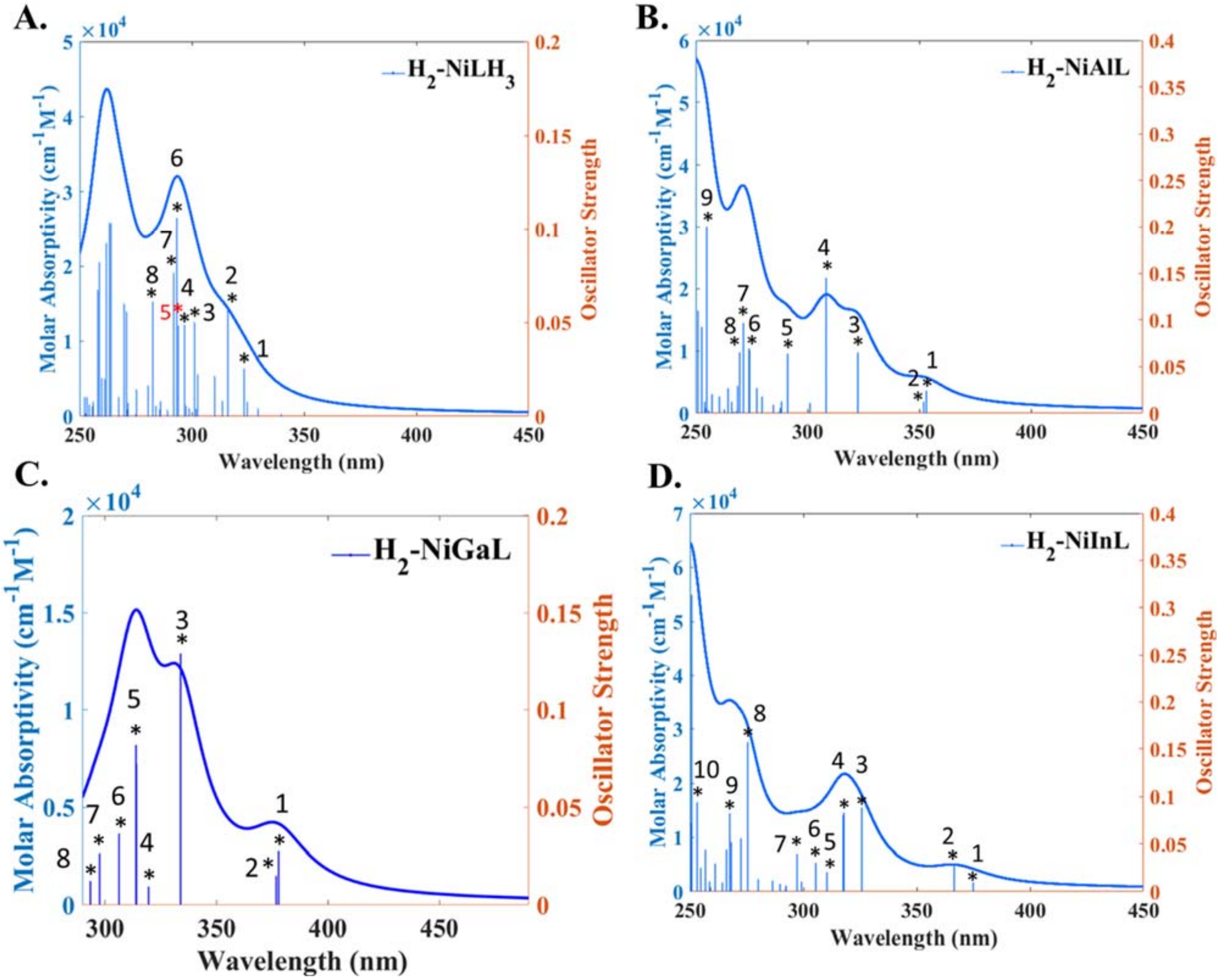

Table S35. Transition assignments for the first several excitations of H_2 adducts based on TD-DFT calculations (M06-D3/bs4). Note: LUMO+5 of (η^2-H_2)NiLH_3, LUMO+2 of (η^2-H_2)NiAlL, and LUMO of (η^2-H_2)NiGaL and (η^2-H_2)NiInL share similar compositions, and are referred to as the *acceptor MOs*.

(η^2-H_2)NiLH_3			(η^2-H_2)NiAlL		
1	340	d_{z^2} → H-H sigma*	1	353	$d_{x^2-y^2}$ → LUMO+2
2	329	$d_{x^2-y^2}$ → LUMO+5	2	352	d_{xy} → LUMO+2
3	324	d_{z^2} → Ligands C	3	323	Ligands N,C → Ligands C
7	310	d_{xy} → LUMO			
(η^2-H_2)NiGaL			(η^2-H_2)NiInL		
1	378	$d_{x^2-y^2}$ → LUMO	1	375	$d_{x^2-y^2}$ → LUMO
2	377	d_{xy} → LUMO	2	367	d_{xy} → LUMO
3	334	Ligands N, C → LUMO	3	326	Ligands N, C → LUMO

Table S36. Detailed transition assignments for excitations of H_2 adducts based on TD-DFT calculations (M06-D3/bs4). Note: the *acceptor MO* of (η^2-H_2)NiLH$_3$ is LUMO+5, of (η^2-H_2)NiAlL is LUMO+2, and of (η^2-H_2)NiGaL and (η^2-H_2)NiInL is LUMO.

(H_2)NiLH$_3$	nm	*f*	Transition	Description	
1	323	0.0256	200 → 202	d_{z^2} → Ligands C	HOMO → LUMO+1
2	316	0.0565	200 → 203	d_{z^2} → Ligands C	HOMO → LUMO+2
3	301	0.0502	200 → 206	d_{z^2} → *acceptor MO*	HOMO → LUMO+5
4	297	0.0487	198 → 201, 202	d_{xy} → Ligands C	HOMO-2 → LUMO,LUMO+1
5	294	0.0482	197 → 201	Ligands C → Ligands C	HOMO-3 → LUMO
6	293	0.1062	197 → 202	Ligands C → Ligands C	HOMO-3 → LUMO+1
7	292	0.0766	198 → 208	d_{xy} → H-H sigma*	HOMO-2 → LUMO+7
8	283	0.0611	198 → 209	d_{xy} → Ligands P,C	HOMO-2 → LUMO+8
(H_2)NiAlL	nm	*f*	Transition	Description	
1	353	0.024	202, 204 → 208	$d_{x^2+y^2}$ → *acceptor MO*	HOMO-1,-3 → LUMO+2
2	352	0.0124	201, 203 → 208	d_{xy} → *acceptor MO*	HOMO-2,-4 → LUMO+2
3	323	0.0645	205 → 206,207	Ligands N,C → Ligands C	HOMO → LUMO, LUMO+1
4	308	0.145	205 → 208	Ligands N,C → *acceptor MO*	HOMO → LUMO+2
5	291	0.0633	203,204 → 206,207	d_{xy}/$d_{x^2-y^2}$+Ligands N, C → Ligands C	HOMO-1,-2 → LUMO, LUMO+1
6	274	0.0691	205 → 210,211	Ligands N,C → Ligands C	HOMO → LUMO+4,+5
7	271	0.0965	200 → 208	d_{z^2} → *acceptor MO*	HOMO-5 → LUMO+2
8	270	0.065	202 → 207	$d_{x^2-y^2}$ + Ligands N,C → Ligands C, benzene	HOMO-3 → LUMO+1
9	255	0.2003	205 → 212	Ligands N, C → Ligands C, benzene	HOMO → LUMO+6
(H_2)NiGaL	nm	*f*	Transition	Description	
1	378	0.0275	210,211 → 215	d_{xy}/$d_{x^2-y^2}$ → *acceptor MO*	HOMO-3,-4 → LUMO
2	334	0.129	214 → 215	Ligands N, C → *acceptor MO*	HOMO → LUMO
3	319	0.0093	207 → 215	Ligands N,C → *acceptor MO*	HOMO-7 → LUMO
4	314	0.0719	214 → 216,217	Ligands N, C → Ligand C, benzene	HOMO → LUMO+1,+2
5	306	0.0364	206,212,213 → 215	Ligands N,C → *acceptor MO*	HOMO-1,-2,-8 → LUMO
6	297	0.0263	212 → 215	Ligands N,C → *acceptor MO*	HOMO-2 → LUMO
7	293	0.0122	206 → 215	Ligands N,C → *acceptor MO*	HOMO-8 → LUMO
8	286	0.0169	213 → 216	Ligands N, C → Ligand C, benzene	HOMO-1 → LUMO+1
(H_2)NiInL	nm	*f*	Transition	Description	
1	375	0.0097	197 → 201	$d_{x^2-y^2}$ → *acceptor MO*	HOMO-3 → LUMO
2	367	0.0276	196 → 201	d_{xy} → *acceptor MO*	HOMO-4 → LUMO
3	326	0.0882	200 → 201	Ligands N, C → *acceptor MO*	HOMO → LUMO
4	318	0.0830	200 → 202	Ligands N, C → Ligands C, benzene	HOMO → LUMO+1
5	318	0.0801	200 → 202,203	Ligands N, C → Ligands C, benzene	HOMO → LUMO +1,2
5	310	0.0203	193,198 → 201	d_{xz} → *acceptor MO*	HOMO-7 → LUMO
6	305	0.0304	199 → 201	Ligands N,C → *acceptor MO*	HOMO-1 → LUMO
8	275	0.1570	200 → 204	Ligands N,C → Ligands C, benzene	HOMO → LUMO+3
9	268	0.0822	195 → 201	d_{z^2} → *acceptor MO*	HOMO-5 → LUMO
10	253	0.0940	196→203	d_{xy} → Ligands C, benzene	HOMO-4 → LUMO+2

Figure S62. Selected MOs of $(N_2)NiML$ and $(N_2)NiLH_3$, as calculated with M06-D3/bs4.

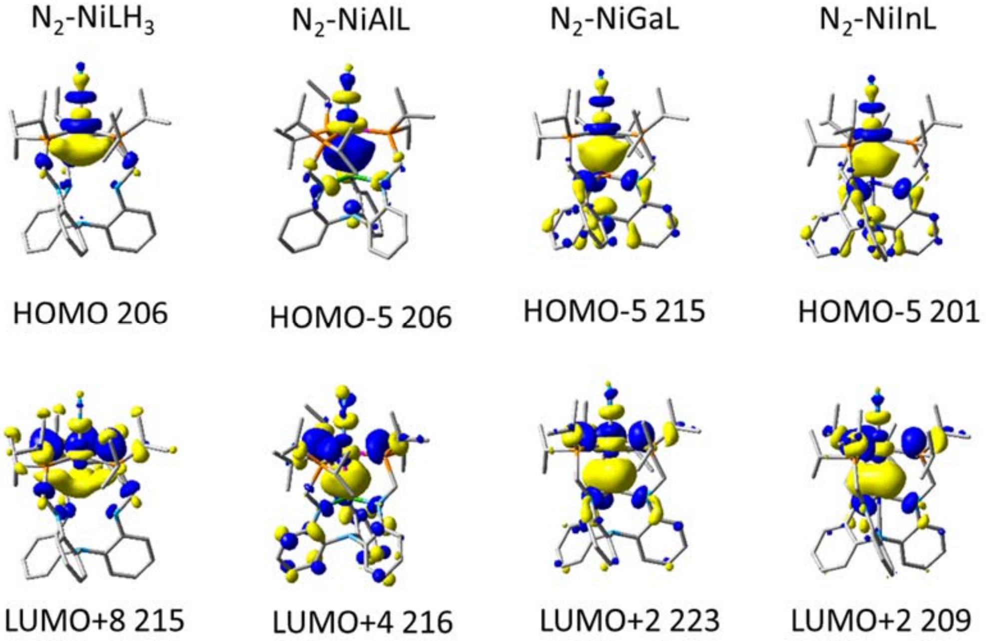

Table S37. Molecular orbital composition analysis (M06-D3/bs4) of the *acceptor MOs* in $(N_2)NiML$ and $(N_2)NiLH_3$.

M06-D3				Ni	M			N (terminal)	P
	No.	# Orb	Assignment	d	s	p	d	p	p
N_2-NiLH$_3$	HOMO	206	d_{z2}	0.70					0.21
	LUMO+8	215	acceptor MO	0.07					0.48
N_2-NiAlL	HOMO-5	206	d_{z2}	0.55	0.08	0.15	0.02		0.03
	LUMO+4	216	acceptor MO	0.15		0.09		0.03	0.29
N_2-NiGaL	HOMO-5	215	d_{z2}	0.44	0.08	0.11	0.04		0.06
	LUMO+2	223	acceptor MO	0.21	0.09	0.09			0.26
N_2-NiInL	HOMO-5	201	d_{z2}	0.48		0.06	0.09		
	LUMO+2	209	acceptor MO	0.21	0.04	0.11	0.07		0.30

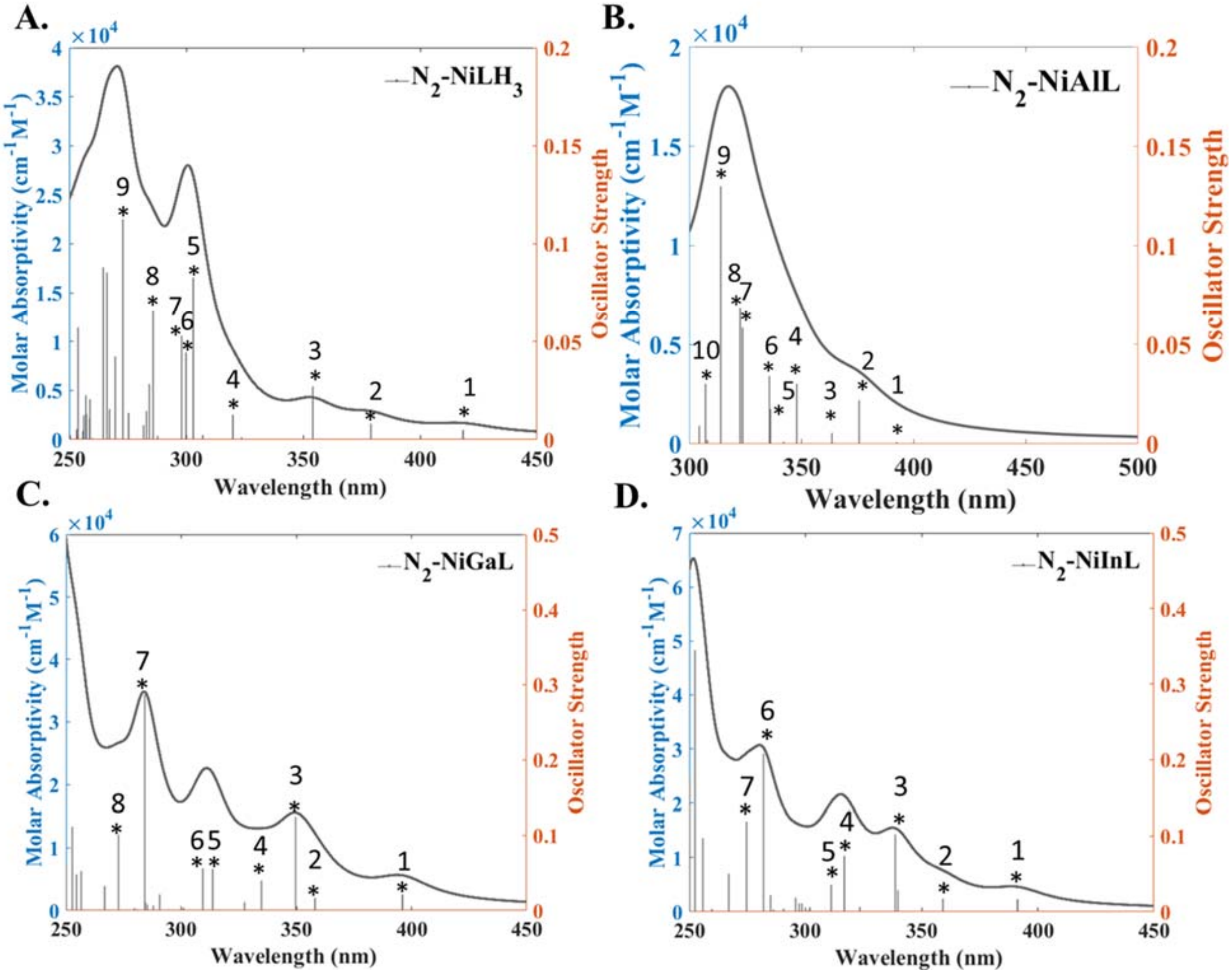

Figure S63. Simulated UV-Vis spectrum of $(N_2)NiLH_3$, $(N_2)NiAlL$, $(N_2)NiGaL$, and $(N_2)NiInL$ as calculated by TD-DFT with M06-D3/bs4 in THF (SMD).

Table S38. Transition assignments for the first six excitations of N_2 adducts based on TD-DFT calculations (M06-D3/bs4). Note: the *acceptor MOs* of $(N_2)NiLH_3$ is LUMO+8, of $(N_2)NiAlL$ is LUMO+4, and of $(N_2)NiGaL$ and $(N_2)NiInL$ is LUMO+2.

$(N_2)NiLH_3$	nm	Description	
1	418	d_{z^2} → N-N pi*	HOMO → LUMO+3,4
2	379	$d_{xy}/d_{x^2-y^2}$ + Ligands P → N-N pi*	HOMO-1,-2 → LUMO+3,4
3	354	$d_{xy}/d_{x^2-y^2}$ + Ligands P → N-N pi*	HOMO-1,-2 → LUMO+3,4
4	320	d_{z^2} → Ligands C, benzene	HOMO → LUMO, LUMO+1
5	303	Ligands N,C → Ligands C, benzene	HOMO-3 → LUMO,LUMO+1
6	300	Ligands N,C → Ligands C, benzene	HOMO-3 → LUMO,LUMO+1
$(N_2)NiAlL$	nm	Description	
1	392	d_{xy} + Ligands P → N-N pi*	HOMO-1 → LUMO+1
2	376	d_{xy} + Ligands P → *acceptor MO*	HOMO-1 → LUMO+4
3	364	d_{xy} + Ligands → N-N pi*	HOMO-1 → LUMO
4	348	$d_{x^2-y^2}$ + Ligands P,N,C → *acceptor MO*	HOMO-2,-4 → LUMO+4
5	336	d_{z^2},Ligands N, C→ N-N pi*	HOMO → LUMO+1
6	336	$d_{x^2-y^2}$ + Ligands P,N,C→ N-N pi*	HOMO-2 → LUMO+1
$(N_2)NiGaL$	nm	Description	
1	396	$d_{xy}/d_{x^2-y^2}$ + Ligand P → *acceptor MO*	HOMO-3,-4 → LUMO+2
2	358	$d_{xy}/d_{x^2-y^2}$ + Ligand P → N-N pi*	HOMO-3,-4 → LUMO,LUMO+1
3	350	Ligand N,C → *acceptor MO*	HOMO → LUMO+2
4	335	$d_{xy}/d_{x^2-y^2}$ + Ligand P → N-N pi*	HOMO-3,-4 → LUMO,LUMO+1
5	314	Ligand N,C → Ligands C, benzene	HOMO → LUMO+3,4
6	309	Ligand N,C → *acceptor MO*	HOMO-1,-2 → LUMO+2
$(N_2)NiInL$	nm	Description	
1	391	$d_{x^2-y^2}/d_{xy}$ + Ligands P → *acceptor MO*	HOMO-3 → LUMO+2
2	359	$d_{xy}/d_{x^2-y^2}$ + Ligands P → N-N pi*	HOMO-3,-4 → LUMO,LUMO+1
3	339	Ligands N,C → *acceptor MO*	HOMO → LUMO+2
4	317	Ligands N,C → Ligands C, benzene	HOMO → LUMO+3,+4
5	311	Ligands N,C → *acceptor MO*	HOMO-1,-2 → LUMO+2
6	282	d_{z^2} → *acceptor MO*	HOMO-5 → LUMO+2

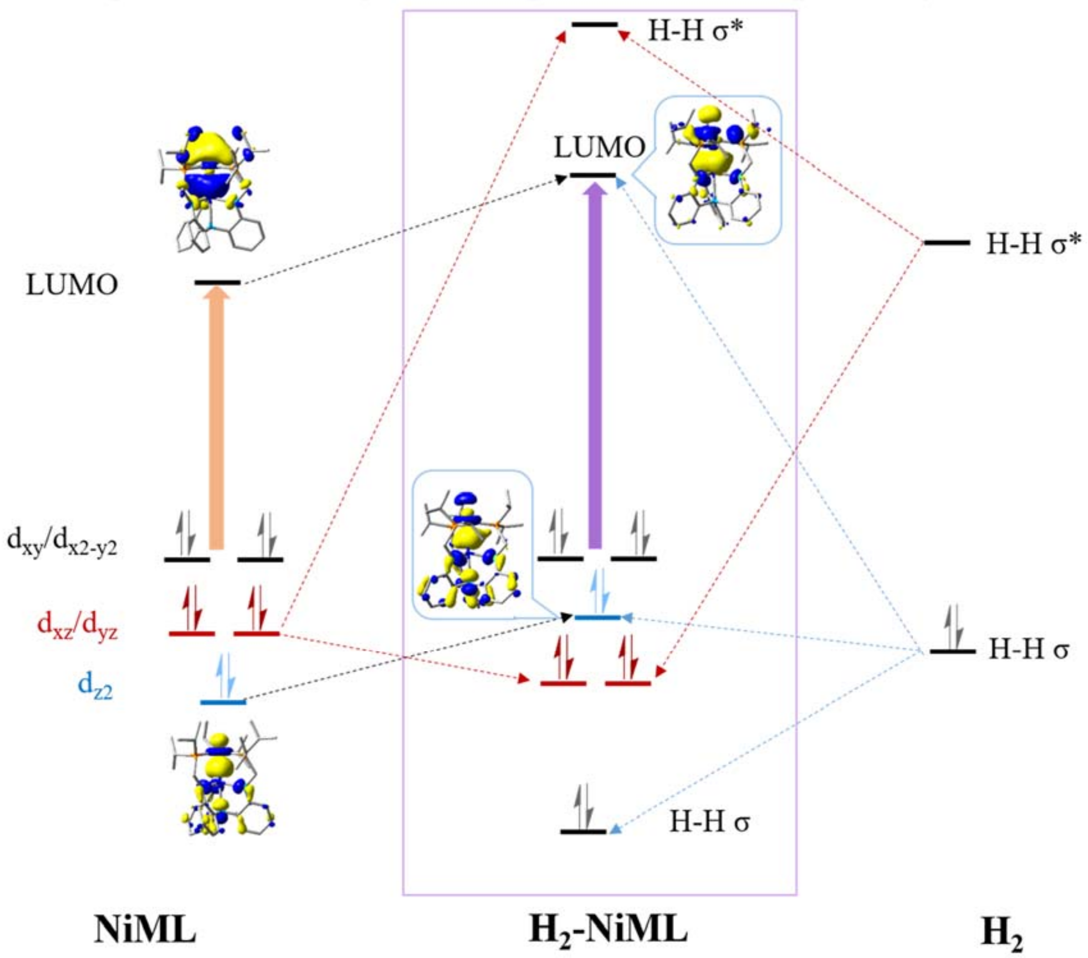

Figure S64. A simplified molecular orbital diagram of (η^2-H_2)NiML. The MO diagram emphasizes the mixing of the H−H σ MO with the LUMO of NiML to generate a new acceptor MO (labeled as LUMO in the center). The Ni→H_2 π-backdonation interaction is also shown, which stabilizes the Ni $3d_{xz}/3d_{yz}$ orbitals. Note that the energy axis is qualitative and not drawn to scale.

VI. Linear Free Energy Relationships

Correlations Between H_2 and N_2 Binding Parameters and Other Variables

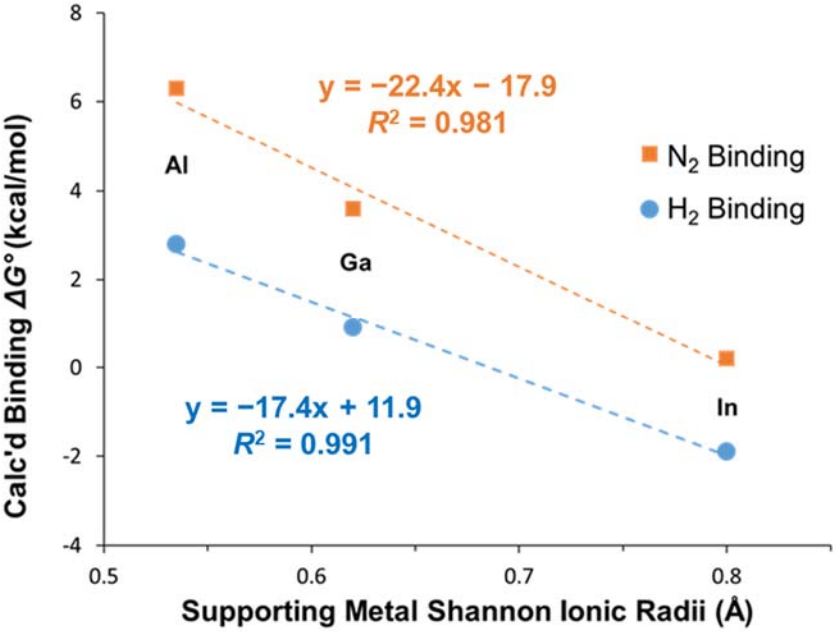

Figure S65. Plot of DFT calculated (M06-L/bs1; see Tables S16-S17) free energies of H_2 and N_2 binding ($\Delta G°$) to NiML vs. Shannon ionic radii (6-coordinate) of the supporting metal (M).[50,51] This plot shows the same trends as the analogous experimental $\Delta G°$ plot shown in Figure 7.

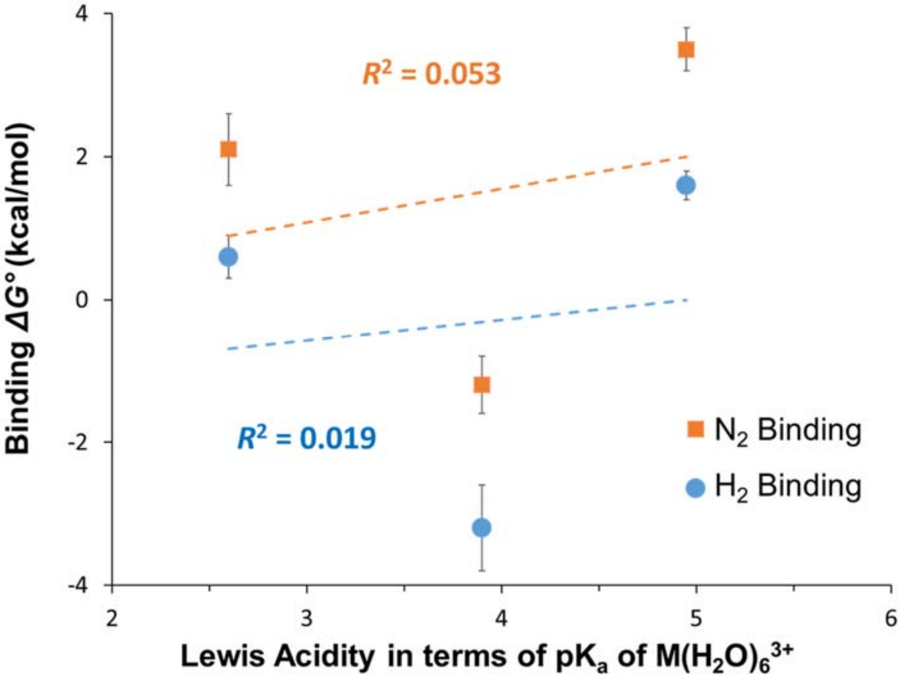

Figure S66. Plot of free energy of H_2 and N_2 binding ($\Delta G°$) to NiML vs. pK_a of $M(H_2O)_6^{3+}$ of the supporting metal.[50,52] Clearly, no correlation exists with this common parameter for Lewis acidity.[53,54]

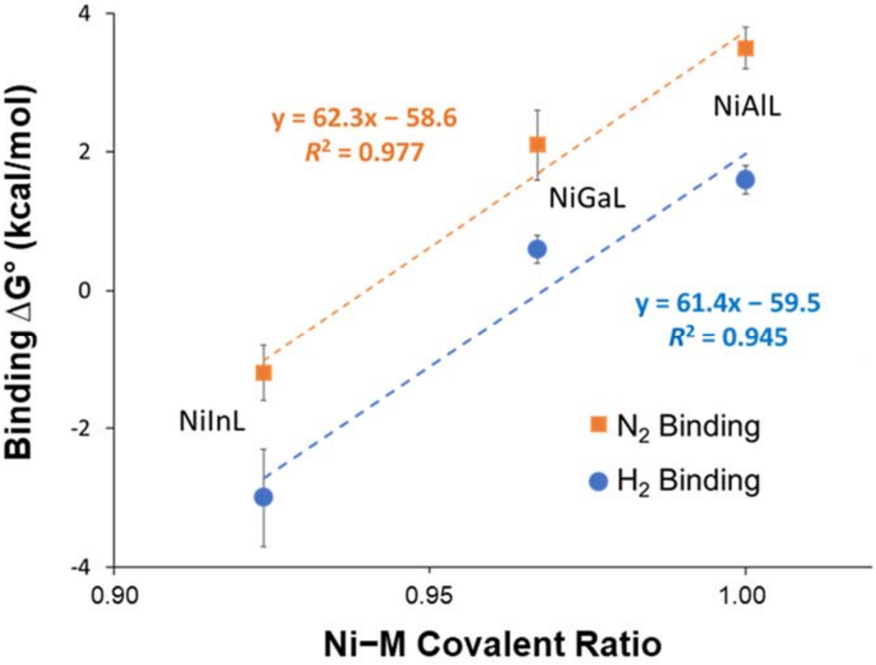

Figure S67. Plot of free energy of H_2 and N_2 binding ($\Delta G°$) to NiML vs. Ni−M covalent ratio, where covalent ratio is the ratio between the Ni−M solid-state bond distance and the sum of the Alvarez covalent radii of Ni and M.[31] Shorter normalized Ni−M bonds result in more favorable binding of both H_2 and N_2.

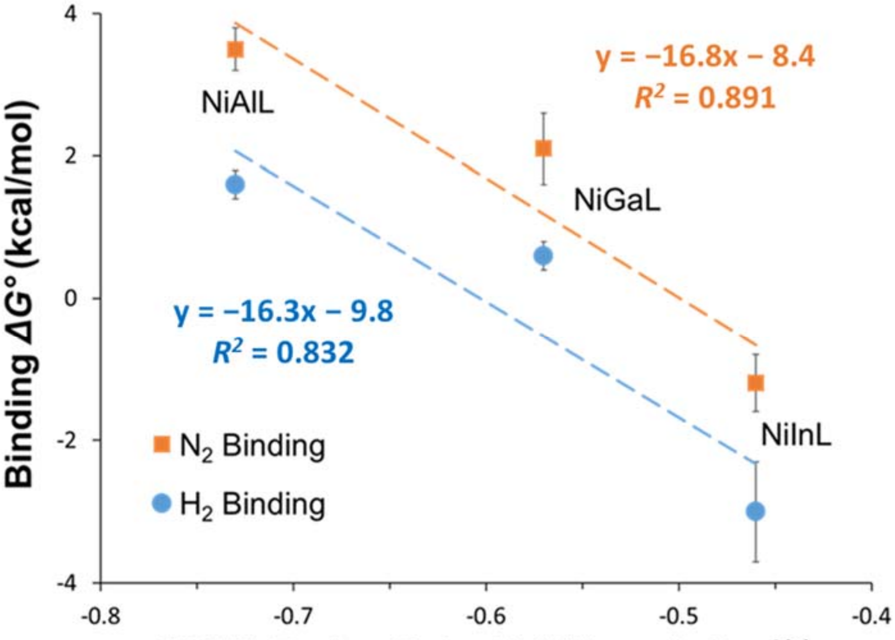

Figure S68. Plot of $\Delta G°$ for H_2 (blue circles) and N_2 binding (orange squares) vs. Ni(I/0) redox potential of NiML in CH_3CN (with $E°_{1/2}$ found to be identical to that in THF for complexes **1** and **2**;[32] see Figure S69 and Table S39). Note that although binding studies were only conducted in toluene for **1** and **3**, binding parameters are likely highly similar in toluene and THF based on DFT calculations (Table S16), our experimental results for **2** (Figures S27-S29), and previous reports.[34,35]

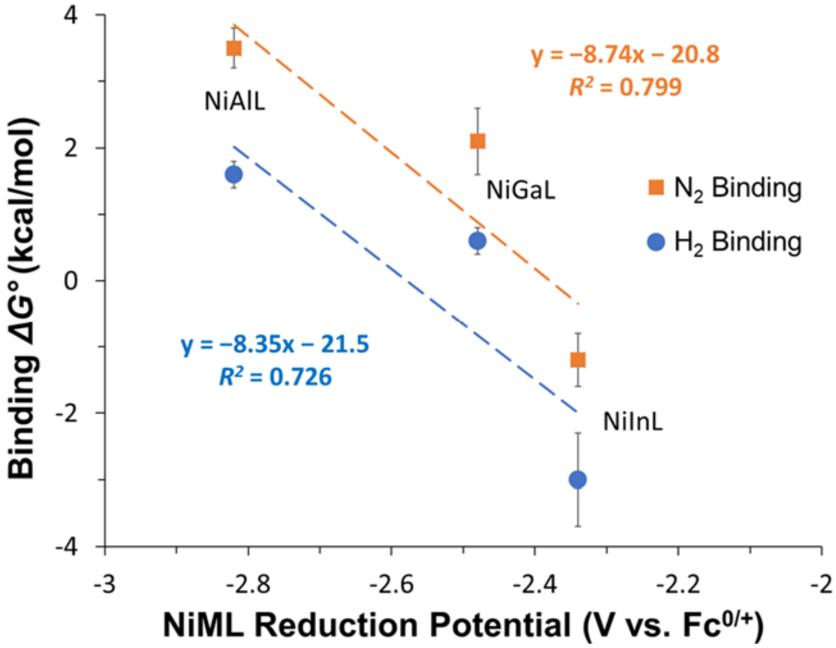

Figure S69. Plot of $\Delta G°$ for H_2 (blue circles) and N_2 binding (orange squares) vs. NiML reduction potential in THF. Note that this reduction has been previously assigned as a unique example of a "Ni(0/−I)" redox couple where the low-lying LUMO of NiML becomes singly-occupied ($R^2 = 0.98$ for correlation of Ni(I/0) and Ni(0/−I) potentials).[55] One might think that the favorability of adding a single electron to the LUMO of NiML complexes would correlate with the favorability of σ-donation from a small molecule into the LUMO, but the sub-par correlation shown is likely the result of the fact that the redox potentials do not capture the significant structural reorganization that occurs upon binding.

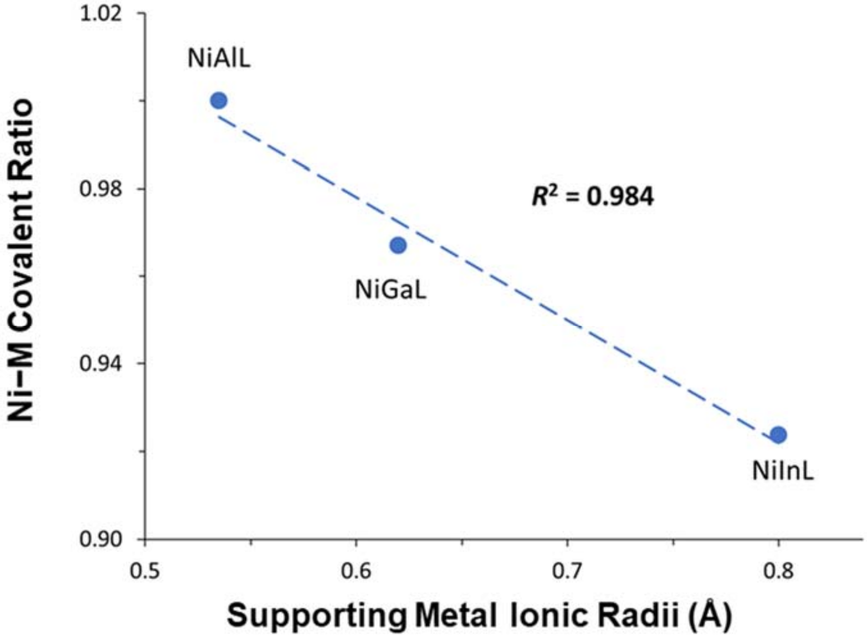

Figure S70. Plot of Ni−M covalent ratio vs. Shannon ionic radii (6-coordinate) of the supporting metal,[50,51] where covalent ratio is the ratio between the Ni−M solid-state bond distance and the sum of the Alvarez covalent radii of Ni and M.[31]

Electronic and Spatial Effects of Supporting Metal in NiML and $NiLH_3$ Complexes

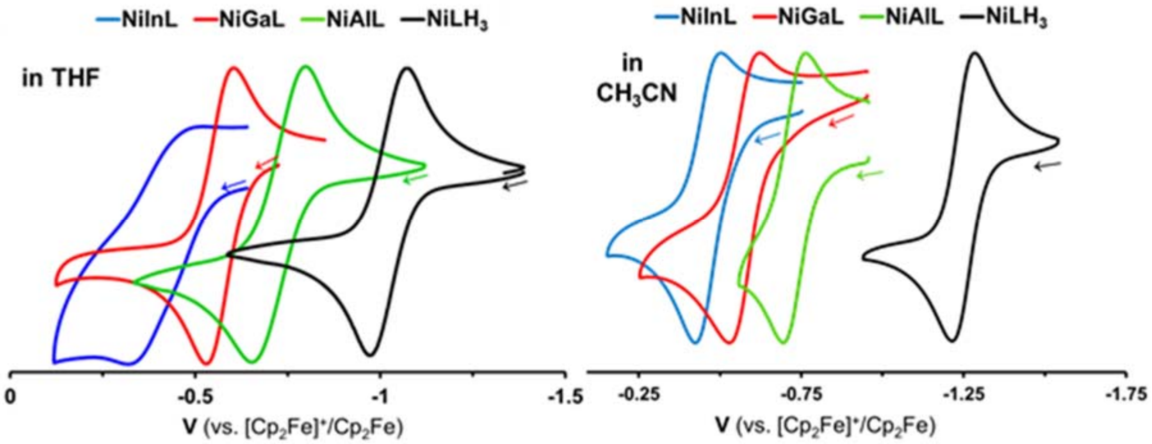

Figure S71. Cyclic voltammograms (CVs) of NiAlL (**1**), NiGaL (**2**), NiInL (**3**), and $NiLH_3$ (**4**) showing the Ni(I/0) redox couples in THF[32,33,56] (left) and in CH_3CN (right). All CVs were collected under 1 atm N_2 with [TBA][PF_6] as the electrolyte (0.1 M or 0.4 M in THF, 0.4 M in CH_3CN). All CVs in CH_3CN were collected with a scan rate of 50 mV/s, whereas CVs in THF were obtained at either 25 or 50 mV/s. All redox potentials are given relative to the $FeCp_2^{+/0}$ redox couple.

Table S39. Comparison of Ni(I/0) redox couple for NiML complexes and **4** in CH_3CN and THF.

	Ni(I/0) couple in CH_3CN					Ni(I/0) couple in THF[a]				
Complex	E_{pa}	E_{pc}	$\mathbf{E°_{1/2}}$	ΔE_p	i_{pa}/i_{pc}	E_{pa}	E_{pc}	$\mathbf{E°_{1/2}}$	ΔE_p	i_{pa}/i_{pc}
4	−1.22	−1.28	**−1.25**	69	1.00	−0.97	−1.07	**−1.02**	100	1.09
1	−0.70	−0.77	**−0.73**	71	1.11	−0.68	−0.79	**−0.74**	108	1.04
2	−0.53	−0.62	**−0.57**	89	1.17	−0.53	−0.61	**−0.57**	73	1.01
3	−0.42	−0.50	**−0.46**	83	1.46	−0.39	–	–	–	–

Note: E_{pa}, E_{pc}, and $E°_{1/2}$ are given in V, and ΔE_p is given in mV. ΔE_p = 57 mV and i_{pa}/i_{pc} = 1.00 for a perfectly reversible redox event. All CVs were collected at a scan rate of 50 mV/s unless otherwise noted. All redox potentials are given relative to the $FeCp_2^{+/0}$ redox couple. [a] CVs of **2** and **3** in THF were collected at a scan rate of 25 mV/s.[32]

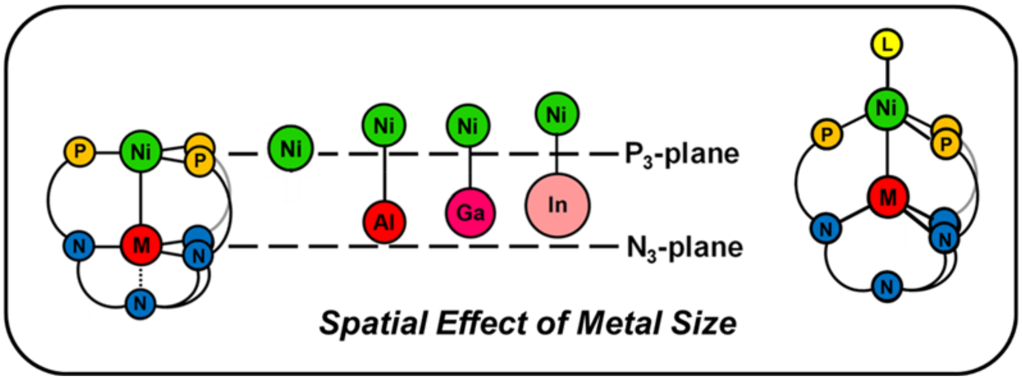

Figure S72. Effect of M(III) size on spatial positioning of Ni and M relative to the planes of their respective binding pockets. The pseudo-tetrahedral geometry of (L')NiML is also shown (*right*).

Correlations of Electronic Structure with Binding Free Energies and Ni−M Bonding

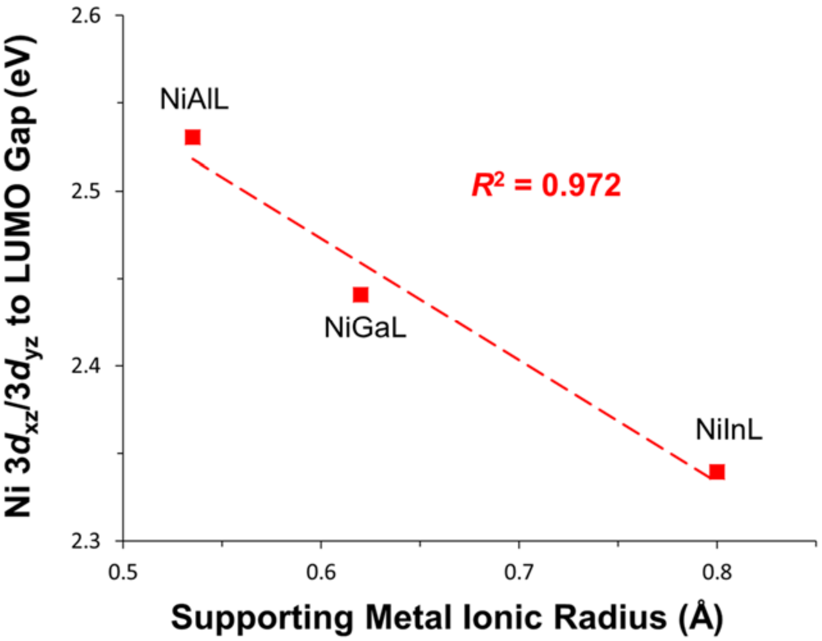

Figure S73. Plot of Ni $3d_{xz}/3d_{yz}$ to LUMO energy gaps (in eV) for NiML complexes vs. supporting metal ionic radii (Shannon 6-coordinate values).[50,51] Ni $3d_{xz}/3d_{yz}$ to LUMO energy gaps were measured via experimental UV-Vis studies (based on transition assignments by TD-DFT calculations).

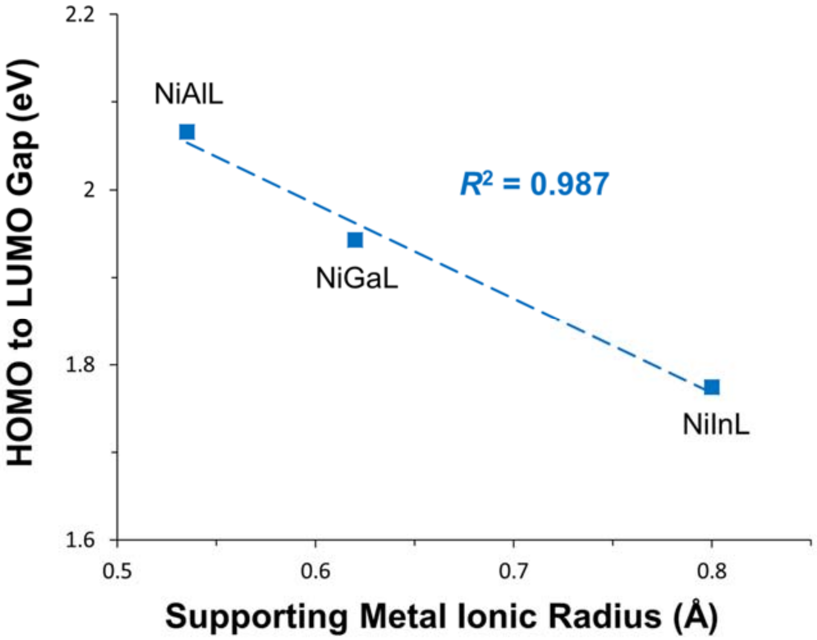

Figure S74. Plot of HOMO to LUMO energy gaps (in eV) for NiML complexes vs. supporting metal ionic radii (Shannon 6-coordinate values).[50,51] HOMO to LUMO energy gaps were measured via experimental UV-Vis studies (based on transition assignments by TD-DFT calculations).

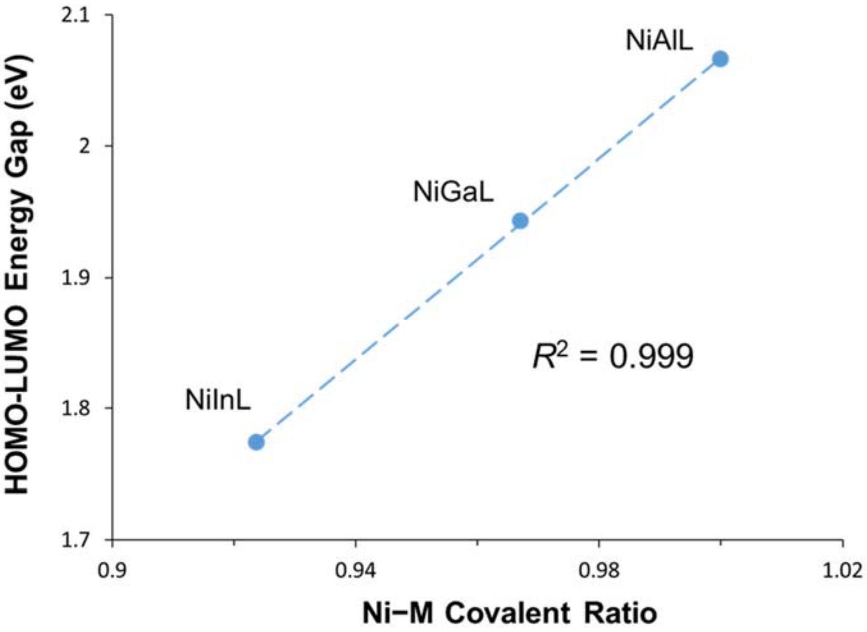

Figure S75. Plot of HOMO-LUMO energy gaps (in eV) vs. Ni−M covalent ratio. HOMO-LUMO energy gaps were measured via experimental UV-Vis studies (with the lowest energy transition assigned as Ni $3d_{xy}/3d_{x^2-y^2}$ to LUMO by TD-DFT calculations), and the Ni−M covalent ratios allow for normalized bond distances that reflect bond strength by comparing the solid-state bond distances to the sums of the Alvarez covalent radii of Ni and M.[31]

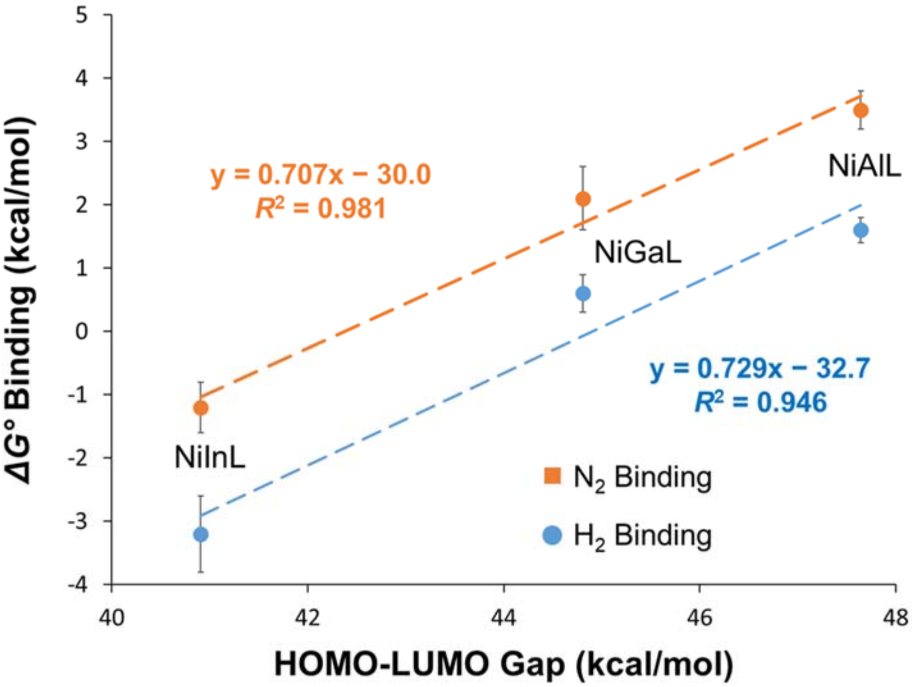

Figure S76. Plot of free energy (Δ*G*°) of H_2 (top, orange) and N_2 binding (bottom, blue) to NiML vs. HOMO-LUMO energy gap for NiML complexes, as measured via experimental UV-Vis studies (lowest energy transition was assigned as Ni $3d_{xy}/3d_{x^2-y^2}$ to LUMO by TD-DFT calculations). The slopes and intercepts are nearly identical for both H_2 and N_2 binding.

VII. References

(1) Williamson, M. P. *Prog. Nucl. Magn. Reson. Spectrosc.* **2013**, *73*, 1-16.
(2) Feeney, J.; Batchelor, J. G.; Albrand, J. P.; Roberts, G. C. K. *J. Magn. Reson.* **1979**, *33*, 519-529.
(3) Just, G. *Zeitschrift Fur Physikalische Chemie--Stochiometrie Und Verwandtschaftslehre* **1901**, *37*, 342-367.
(4) Field, L. R.; Wilhelm, E.; Battino, R. *Journal of Chemical Thermodynamics* **1974**, *6*, 237-243.
(5) Battino, R., Nitrogen and Air. In *International Union of Pure and Applied Chemistry: Analytical Chemistry Division Commission on Solubility Data* [Online] Permagon Press Inc.: Elmsford, NY, USA, 1982; p. 162. https://srdata.nist.gov/solubility/IUPAC/SDS-10/SDS-10.pdf.
(6) Brunner, E. *Journal of Chemical and Engineering Data* **1985**, *30*, 269-273.
(7) Jabloniec, A.; Horstmann, S.; Gmehling, J. *Industrial & Engineering Chemistry Research* **2007**, *46*, 4654-4659.
(8) Yonker, C. R.; Linehan, J. C. *J. Organomet. Chem.* **2002**, *650*, 249-257.
(9) Suess, D. L. M.; Tsay, C.; Peters, J. C. *J. Am. Chem. Soc.* **2012**, *134*, 14158-14164.
(10) Grills, D. C.; van Eldik, R.; Muckerman, J. T.; Fujita, E. *J. Am. Chem. Soc.* **2006**, *128*, 15728-15741.
(11) Sandstrom, J. R., *Dynamic Nuclear Resonance Spectroscopy*. 1st ed.; Academic Press, Inc: San Diego, CA, 1983.
(12) Bryant, R. G. *J. Chem. Ed.* **1983**, *60*, 933-935.
(13) Binsch, G. *J. Am. Chem. Soc.* **1969**, *91*, 1304-1309.
(14) Hulley, E. B.; Helm, M. L.; Bullock, R. M. *Chem. Sci.* **2014**, *5*, 4729-4741.
(15) Sudmeier, J. L.; Evelhoch, J. L.; Jonsson, N. B. H. *J. Magn. Reson.* **1980**, *40*, 377-390.
(16) Jaeschke, A.; Muensch, H.; Schmid, H. G.; Friebolin, H.; Mannschreck, A. *Journal of Molecular Spectroscopy* **1969**, *31*, 14-+.
(17) Halpern, J. *Bulletin of the Chemical Society of Japan* **1988**, *61*, 13-15.
(18) Budzelaar, P. H. M. *gNMR User Manual*, 5.0; IvorySoft: 2006.
(19) Stephenson, D. S.; Binsch, G. *J. Magn. Reson.* **1978**, *32*, 145-152.
(20) Vollmer, M. V.; Cammarota, R. C.; Lu, C. C. *Eur. J. Inorg. Chem.* **2019**, *2019*, 2140-2145.
(21) Frisch, M. J.; Trucks, G. W.; Schlegel, H. B.; Scuseria, G. E.; Robb, M. A.; Cheeseman, J. R.; Scalmani, G.; Barone, V.; Mennucci, B.; Petersson, G. A. *Gaussian 09, Revision E. 01, Gaussian, Inc., Wallingford CT*, 2009.
(22) Zhao, Y.; Truhlar, D. G. *J. Chem. Phys.* **2006**, *125*, 194101.
(23) Adamo, C.; Barone, V. *J. Chem. Phys.* **1999**, *110*, 6158-6170.
(24) Van Lenthe, E.; Baerends, E. J. *J. Comput. Chem.* **2003**, *24*, 1142-1156.
(25) von Hopffgarten, M.; Frenking, G. *Wiley Interdisciplinary Reviews-Computational Molecular Science* **2012**, *2*, 43-62.
(26) Hopffgarten, M. v.; Frenking, G. *Wiley Interdisciplinary Reviews: Computational Molecular Science* **2012**, *2*, 43-62.
(27) te Velde, G.; Bickelhaupt, F. M.; Baerends, E. J.; Fonseca Guerra, C.; van Gisbergen, S. J. A.; Snijders, J. G.; Ziegler, T. *J. Comput. Chem.* **2001**, *22*, 931-967.
(28) *ADF2016, SCM, Theoretical Chemistry, Vrije Universiteit, Amsterdam, The Netherlands, http://www.scm.com*.
(29) Mitoraj, M. P.; Michalak, A.; Ziegler, T. *J. Chem. Theory Comput.* **2009**, *5*, 962-975.
(30) Van Lenthe, E.; Snijders, J. G.; Baerends, E. J. *J. Chem. Phys.* **1996**, *105*, 6505-6516.
(31) Cordero, B.; Gómez, V.; Platero-Prats, A. E.; Revés, M.; Echeverría, J.; Cremades, E.; Barragán, F.; Alvarez, S. *Dalton Trans.* **2008**, 2832-2838.
(32) Cammarota, R. C.; Lu, C. C. *J. Am. Chem. Soc.* **2015**, *137*, 12486-12489.
(33) Clouston, L. J.; Siedschlag, R. B.; Rudd, P. A.; Planas, N.; Hu, S.; Miller, A. D.; Gagliardi, L.; Lu, C. C. *J. Am. Chem. Soc.* **2013**, *135*, 13142-13148.
(34) Gonzalez, A. A.; Hoff, C. D. *Inorg. Chem.* **1989**, *28*, 4295-4297.

(35) Gonzalez, A. A.; Zhang, K.; Nolan, S. P.; Lopez de la Vega, R.; Mukerjee, S. L.; Hoff, C. D.; Kubas, G. J. *Organometallics* **1988**, *7*, 2429-2435.
(36) Prokopchuk, D. E.; Chambers, G. M.; Walter, E. D.; Mock, M. T.; Bullock, R. M. *J. Am. Chem. Soc.* **2019**, *141*, 1871-1876.
(37) Hauger, B. E.; Gusev, D.; Caulton, K. G. *J. Am. Chem. Soc.* **1994**, *116*, 208-214.
(38) Gusev, D. G.; Vymenits, A. B.; Bakhmutov, V. I. *Inorg. Chem.* **1992**, *31*, 1-2.
(39) Mediati, M.; Tachibana, G. N.; Jensen, C. M. *Inorg. Chem.* **1990**, *29*, 3-5.
(40) Gusev, D. G.; Bakhmutov, V. I.; Grushin, V. V.; Vol'pin, M. E. *Inorg. Chim. Acta* **1990**, *175*, 19-21.
(41) Gusev, D. G.; Bakhmutov, V. I.; Grushin, V. V.; Vol'pin, M. E. *Inorg. Chim. Acta* **1990**, *177*, 115-120.
(42) Heinekey, D. M.; Voges, M. H.; Barnhart, D. M. *J. Am. Chem. Soc.* **1996**, *118*, 10792-10802.
(43) Prokopchuk, D. E.; Wiedner, E. S.; Walter, E. D.; Popescu, C. V.; Piro, N. A.; Kassel, W. S.; Bullock, R. M.; Mock, M. T. *J. Am. Chem. Soc.* **2017**, *139*, 9291-9301.
(44) Rittle, J.; McCrory, C. C. L.; Peters, J. C. *J. Am. Chem. Soc.* **2014**, *136*, 13853-13862.
(45) Luther, T. A.; Heinekey, D. M. *Inorg. Chem.* **1998**, *37*, 127-132.
(46) Li, Y.; Hou, C.; Jiang, J.; Zhang, Z.; Zhao, C.; Page, A. J.; Ke, Z. *ACS Catal.* **2016**, *6*, 1655-1662.
(47) Harman, W. H.; Lin, T. P.; Peters, J. C. *Angew. Chem. Int. Ed.* **2014**, *53*, 1081-1086.
(48) Harman, W. H.; Peters, J. C. *J. Am. Chem. Soc.* **2012**, *134*, 5080-5082.
(49) Cammarota, R. C.; Clouston, L. J.; Lu, C. C. *Coord. Chem. Rev.* **2017**, *334*, 100-111.
(50) Downs, A. J., *Chemistry of Aluminum, Gallium, Indium, and Thallium*. Chapman & Hall: London, 1993.
(51) Shannon, R. D. *Acta Crystallogr. Sect. A* **1976**, *32*, 751-767.
(52) Perrin, D. D., *Ionisation Constants of Inorganic Acids and Bases in Aqueous Solution*. 2nd Edition ed.; Pergamon Press: Elmsford, NY, 1982.
(53) Tsui, E. Y.; Tran, R.; Yano, J.; Agapie, T. *Nat. Chem.* **2013**, *5*, 293-299.
(54) Herbert, D. E.; Lionetti, D.; Rittle, J.; Agapie, T. *J. Am. Chem. Soc.* **2013**, *135*, 19075-19078.
(55) Vollmer, M. V.; Xie, J.; Cammarota, R. C.; Young, V. G.; Bill, E.; Gagliardi, L.; Lu, C. C. *Angew. Chem. Int. Ed.* **2018**, *57*, 7815-7819.
(56) Rudd, P. A.; Liu, S.; Gagliardi, L.; Young, V. G.; Lu, C. C. *J. Am. Chem. Soc.* **2011**, *133*, 20724-20727.